THE UNIVERSITY OF CHICAGO

A PRECISION MEASUREMENT OF THE CHARGE ASYMMETRY OF SEMI-LEPTONIC KAON DECAYS BEHIND A REGENERATOR AT KTEV

A DISSERTATION SUBMITTED TO
THE FACULTY OF THE DIVISION OF THE PHYSICAL SCIENCES
IN CANDIDACY FOR THE DEGREE OF
DOCTOR OF PHILOSOPHY

DEPARTMENT OF PHYSICS

BY
G. COLIN BOWN

CHICAGO, ILLINOIS
JUNE 2004

For Jennifer, Logan and Anna

Ars longa, vita brevis

TABLE OF CONTENTS

LIST OF FIGURES

LIST OF TABLES

ABSTRACT

This thesis describes the measurement of three parameters of the neutral kaon system by the KTeV collaboration at Fermi National Accelerator Laboratory. Using 125 million semi-leptonic kaons decays, we measure the asymmetry between $K \to \pi^- e^+ \bar{\nu}_e$ and $K \to \pi^+ e^- \nu_e$ decays downstream of a regenerator. We combine a sophisticated model of the charge asymmetry with these data to determine precisely $\phi_{f-\bar{f}}$, δ_L, and $\Re(x)$. The regeneration phase of carbon, $\phi_{f-\bar{f}}$, previously unmeasured in the KTeV momentum range, is found to be consistent with the optical model prediction:

$$\phi_{f-\bar{f}} - \phi_{analyticity} = -0.70^\circ \pm 0.88^\circ \text{ (stat)} \pm 0.91^\circ \text{ (syst)} .$$

A measure of the **CP** violating K_L asymmetry yields:

$$\delta_L = (3480 \pm 89 \text{ (stat)} \pm 53 \text{ (syst)}) \times 10^{-6} .$$

This result is more precise than any outside of the KTeV collaboration. We also measure the real part of the semi-leptonic $\Delta S \neq \Delta Q$ amplitude, x, more precisely than in any other experiment. It is consistent with zero:

$$\Re(x) = (12 \pm 33 \text{ (stat)} \pm 39 \text{ (syst)}) \times 10^{-4} .$$

ACKNOWLEDGMENTS

My grandmother, Andrea Flynn, always thought I should more carefully study history lest I be doomed to repeat it. Shortly after moving back to Austin, *All But Dissertation*, in 2001, my other grandmother, Evelyn Bown, gave me a lesson. I knew that her husband, Oliver Bown, had studied psychology at the University of Chicago under Carl Rogers. I didn't know that he had moved his young family to Austin, *All But Dissertation*, started his career at the University of Texas, and only then finished his degree. In my mind these towering figures in my life laugh at me, both saying "We could have told you it wouldn't be easy." It hasn't been easy. But I feel more blessed than doomed.

I have had a number of mentors these last twelve years. To my long time advisor, Bruce Winstein, I marvel at your ability to look at a problem and cut straight to the heart of the most critical matter. I've learned from you that complex systems need not be intimidating landscapes. You simply make your own signposts on the back of an envelope. Thank you. To my advisor, Ed Blucher, I could not have completed this thesis without your friendship and support. How many walking conversations, hands full of hot coffee and croissant, have revealed the right question, made a missing connection, or just inspired an uplifting laugh? I couldn't count. I am enormously grateful. I would also like to recognize Elliot Cheu, Harold Sanders and Hans Kobrak, each of whom in their own way took me under their wing and guided me toward the goal line but reminded me to enjoy the journey.

This project would clearly not be possible without the combined efforts of the KTeV collaboration as a whole. We built one heck of a detector, fast. I would like to single out, for their outstanding insights and assistance, my University of Chicago commrads in precision measurements: Roy Briere, Bernhard Schwingenheuer, Peter Shawhan, Jim Graham and Val Prasad.

In the metaphor of graduate school as a crucible, there are many people with whom I am eternally alloyed. John Wahl, Breese Quinn, Elizabeth Grossman, Peko Hesoi, Daniel Holz, Rob Deegan, Rob Wickham: our chalk talks taught me the majority of the physics that I now use on a daily basis. Who knew?

Mike Revesz and Min-Fon Chang, I am very lucky to have such good friends as colleagues. Charles Loeffler, I wasn't sure if I should thank you with the 'mentors', or with the 'good friends from work'. On the one hand you gave me my first science job just out of high school, gave me a summer job out of college, advised me through out, then hired me for real and taught me, and continue to teach me the finer points of signal processing, communications theory, sonar systems, office politics, funding agency politics, and child rearing. On the other hand you have been known to exchange airzooka fire, laugh at my jokes, make fun of my driving and exchange the occasional story that goes in the category of "too much information". Your black-belt kid tipped the balance, so it is here that I thank you for the slack you cut me to finish this degree, and for your treasured friendship.

I am extremely grateful to my immediate family, blood and other: Kevin, Erin, Heidi, Kathie, Pat, Andy, Sarah, Emil, Jennifer, Brian, Elizabeth. You always believed in me and it meant the world to me. Thank you too to my in-laws Dave and Nancy.

This has been a harder path than I anticipated. Even in the toughest places, my core team has never left my side. Mom, I don't understand how you can have so

much energy and optimism when you give so much of it to everyone you touch. Pop, you may not know it but your guidance and your poetry have shaped the deepest pillars of my faith. The power of ideas can make the world a better place. One poem, one experiment, one person at a time. My dear wife, Jennifer. Where are the superlatives? I know that without your help I would have faltered and failed. I also know that together we will get to laugh when our grandkids draw "A Precision Measurement ... KTeV" from the charades hat. Will you marry me?

Logan and Anna, at the finish line I thought of your futures as I wrote this paper. Learn your history well. I hope each of your paths cross as many wonderful lives and experience as much joy as mine has.

CHAPTER 1

INTRODUCTION

Experiments that measure the behavior of the neutral kaon, such as the one described in this thesis, are complex undertakings requiring millions of dollars in equipment and hundreds of person-years dedicated to construction, maintenance, monitoring, and analysis. Although the investment required is large, these experiments have produced a handsome return in the form of insight into the symmetries that underpin the Standard Model. The investigation that follows derives its results from a precise study of semi-leptonic decays of the neutral kaon. These decays are of particular interest for two reasons: first, they shed light on deeper questions of **CPT** conservation and causality, and second they provide an experimental probe that is sensitive to unexpected decay mechanisms and exchange resonances.

Prior to 1957, all observed interactions of matter conserved the symmetries of charge conjugation (**C**), parity (**P**) and time reversal (**T**). Lee and Yang [1] motivated the observation by several experiments of parity violation in nuclear decay [2, 3, 4], the product **CP** elegantly replaced the individual symmetries of **C** and **P**. In 1964, Christenson, Cronin, Fitch and Turlay [5] observed indirect **CP** violation in the neutral kaon system. Subsequent interest in the mechanisms of **CP** violation resulted in a huge experimental effort focused on the kaon system. The brass ring has been the observation of direct **CP** violation. The high kaon flux and high detector precision required for this search, together with a strong interest

in the rare decays of kaons, motivated the development of KTeV, an exceptionally sensitive detector at Fermilab. This thesis will exploit the mechanism which makes the kaon system ideal for probing **CP** violation in order to test **CPT** symmetry, causality and our understanding of the fundamental components of the Standard Model.

Other precision KTeV measurements focus on the oscillation seen in the decay rate of $K \to \pi^+\pi^-$ ($K_{\pi 2}$) behind a thick regenerator. It is relatively easy to determine the decay distribution of $K_{\pi 2}$ events because one fully reconstructs the event. Our analysis will focus on $K^0 \to \pi e \nu_e$ decays (K_{e3}). These semi-leptonic decays provide unique information. The strength of K_{e3} asymmetry at small values of proper time is sensitive to violations in the $\Delta S = \Delta Q$ rule. At large values of proper time, the asymmetry is a direct measurement of the real part of the kaon mixing parameter ϵ_K. Through intermediate values of proper time, the charge asymmetry is sensitive to the regeneration phase but not to any final state interactions. Phase measurements at low energies give clues to behavior at higher, even inaccessible, energies. Combining the phase measurement from this thesis with the regeneration amplitude measurement made with $K_{\pi 2}$ events probes the scattering behavior of kaons beyond the current observable energy range. Experimentally, the asymmetry can be measured without the simulation-dependent normalization which is required for $K_{\pi 2}$ measurements. But, analysis challenges remain due to the missing neutrino. Simulation will still be required for understanding kaon momentum distribution as well as the considerable background from scattering in the regenerator.

This chapter introduces the kaon system (Section 1.1) with a focus on its interaction with matter (Section 1.2), then describes the key role that kaon decays to 2π ($K_{\pi 2}$) have in probing **CP** violation (Sections 1.3 and 1.4). These studies motivate the introduction of the theoretical underpinnings of analyticity (Section 1.5), and

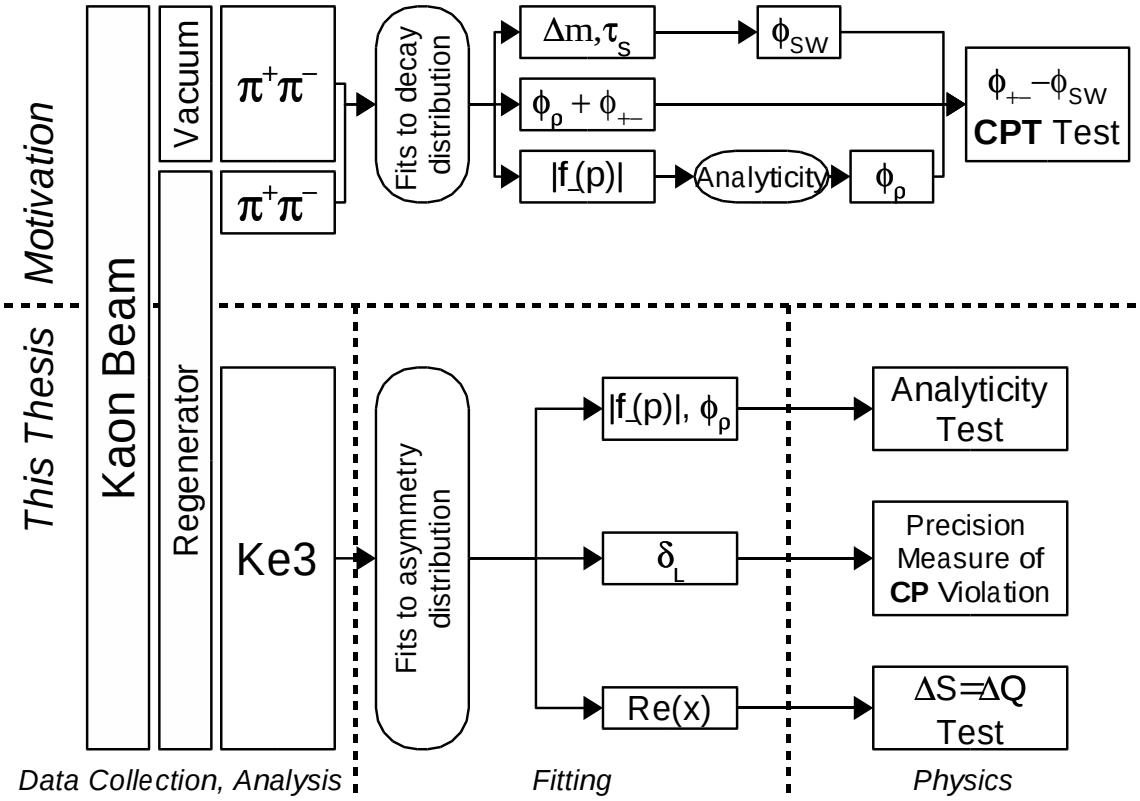

Figure 1.1: Overview of the Motives and Goals of this Thesis

the use of the asymmetry of semi-leptonic kaon decays downstream of a regenerator to measure the phase and magitude of an analytic scattering amplitude over a range of momenta (Section 1.6). In addition, the assumption that semi-leptonic decay is principally a $\Delta S = \Delta Q$ process is relaxed and a test for surprising violations of this rule is described. Figure 1.1 provides an overview of the motivation and goals of this thesis.

1.1 Kaon Phenomenology

The kaon system is a two state system with mass eigenstates determined by the strangeness (**S**) conserving strong force and decay eigenstates determined by the weak force:

$$\begin{aligned} K^0 &= \overline{s}d \longleftarrow Strangeness = +1 \\ \overline{K^0} &= s\overline{d} \longleftarrow Strangeness = -1 \ . \end{aligned} \tag{1.1}$$

K^0 and $\overline{K^0}$ are **CP** conjugates of one another. In the notation where **CP** is seen as a Hilbert space operator:

$$\begin{aligned} \mathbf{CP}|K^0\rangle &= e^{i\pi\phi}|\overline{K^0}\rangle \\ \mathbf{CP}|\overline{K^0}\rangle &= e^{i\pi\phi}|K^0\rangle \ . \end{aligned} \tag{1.2}$$

The **CP** violation in decay is very small and so the decay eigenstates are most easily written as a perturbation of the **CP** eigenstates (ironically K_1 is *even* and K_2 is *odd*).

$$\begin{aligned} |K_1\rangle &= \frac{1}{\sqrt{2}}(|K^0\rangle + |\overline{K^0}\rangle) \\ |K_2\rangle &= \frac{1}{\sqrt{2}}(|K^0\rangle - |\overline{K^0}\rangle) \ . \end{aligned} \tag{1.3}$$

Prior to 1964, these states were thought to be equivalent to the observed short- and long-lived kaon states. K_1 decayed to the **CP**-even 2π final state rapidly due the large phase space available. K_2, being **CP**-odd, was precluded from decay to the 2π state, so decayed more slowly to the available 3 particle final states (3π, K_{e3}). The

observation by Christianson, Cronin, Fitch and Turlay [5] that K_2 can decay to a 2π final state, necessitated a new model. This led to the introduction of an effective Hamiltonian, $\mathcal{H}$, that would dynamically mix the **CP** eigenstates. In the K^0, $\overline{K^0}$ basis the most general form is

$$\mathcal{H} = \begin{pmatrix} M_{11} & M_{12} \\ M_{12}^* & M_{22} \end{pmatrix} - \frac{i}{2} \begin{pmatrix} \Gamma_{11} & \Gamma_{12} \\ \Gamma_{12}^* & \Gamma_{22} \end{pmatrix} . \tag{1.4}$$

Here the diagonal elements are real and the off diagonals are complex. The result is a leading hermitian term, determined by coupling within the kaon system, and a second anti-hermitian term, determined by coupling outside the kaon system. In the absence of any constraints from **C**,**P**,**T** or combinations, this hamiltonian still has the 8-degrees of freedom of a completely general complex matrix. The eigenvectors of this system will be the observed states, K_S and K_L. Constraints from physical symmetries reduce the original 8-degrees of freedom. The assumption of **CPT** conservation results in a pair of constraints:

$$\begin{aligned} M_{11} &= M_{22} \\ \Gamma_{11} &= \Gamma_{22} \end{aligned} \tag{1.5}$$

The assumption of **CP** conservation results in a pair of constraints:

$$\begin{aligned} Im(M_{12}) &= 0 \\ Im(\Gamma_{11}) &= 0 \end{aligned} \tag{1.6}$$

If all of these constraints are applied, the resulting eigenvectors are K_1 and K_2. Releasing the **CP** constraint and solving gives new eigenvectors, most easily written

in terms of K_1 and K_2:

$$\begin{aligned} |K_S\rangle &= \frac{1}{\sqrt{1+|\epsilon_K|^2}}\left(|K_1\rangle + \epsilon_K|K_2\rangle\right) \text{ , and} \\ |K_L\rangle &= \frac{1}{\sqrt{1+|\epsilon_K|^2}}\left(\epsilon_K|K_1\rangle + |K_2\rangle\right) \text{ ,} \end{aligned} \tag{1.7}$$

where:

$$\begin{aligned} \epsilon_K &= \frac{Im(M_{12}) - \frac{i}{2}Im(\Gamma_{12})}{i\Delta m - \frac{1}{2}\Delta\Gamma} \text{ ,} \\ \Delta m &= m_L - m_S = 2\cdot\Re(M_{12}) \text{ , and} \\ \Delta\Gamma &= \Gamma_S - \Gamma_L = -2\cdot\Re(\Gamma_{12}) \text{ .} \end{aligned} \tag{1.8}$$

These expressions are accurate to first order in ϵ_K. This form emphasizes that **CP** violation in either the mass term (M_{12}) or the decay term (Γ_{12}) acts as a perturbation to a base system that is dominantly **CP** conserving. Measurements of the kaon system show that the **CP** violation proceeds dominantly through the mass matrix, typified by diagrams like Figure 1.2, even to the point of inspiring so called super-weak theory [6], which postulates a unique **CP** violating mechanism in the mass matrix and no **CP** violation through the decay channel, i.e. $Im(\Gamma_{12}) = 0$. This results in the so called *super-weak* phase,

$$\phi_{SW} = \text{Arctan}\left(\frac{2\Delta m}{\Delta\Gamma}\right) \text{ .} \tag{1.9}$$

This is very close to being the exact phase of ϵ_K, and consequently this angle is used as the reference against which other **CP** violating phases are compared. For current best values of Δm and $\Delta\Gamma$, ϕ_{SW} is 43.4°. Releasing the constraints on $\mathcal{H}$ from **CPT** symmetry, but assuming the departure to be small, results in an additional

perturbative term, again arising from violation in either the mass term or the decay term:

$$\begin{aligned} |K_S\rangle &= \frac{1}{\sqrt{1+|\epsilon_K+\delta_K|^2}}(|K_1\rangle + (\epsilon_K+\delta_K)|K_2\rangle)\ , \\ |K_L\rangle &= \frac{1}{\sqrt{1+|\epsilon_K-\delta_K|^2}}((\epsilon_K-\delta_K)|K_1\rangle + |K_2\rangle)\ , \text{ and} \\ \delta_K &= \frac{\frac{i}{2}(M_{22}-M_{11})+\frac{1}{4}(\Gamma_{22}-\Gamma_{11})}{i\Delta m - \frac{1}{2}\Delta\Gamma}\ . \end{aligned} \tag{1.10}$$

This describes *indirect* **CPT** violation. Other possible mechanisms for **CPT** violation are plentiful and could manifest themselves in many different ways.

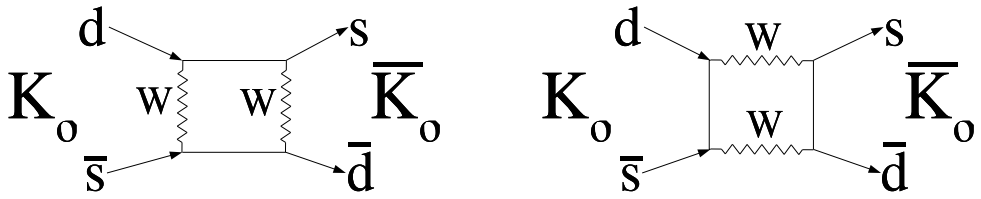

Figure 1.2: Second Order Box Diagram for K^0- $\overline{K^0}$ Mixing

1.2 Regeneration

In order to understand how precision **CP** tests are performed in the KTeV apparatus, it is first necessary to understand the phenomenon of regeneration. Due to the asymmetry of the interaction of K^0 and $\overline{K^0}$ with matter ($\overline{K^0}$ is more strongly absorbed), a pure K_L beam traversing a matter field is attenuated but also develops a K_S component. To see how this happens, let f and $\bar{f}$ be the forward scattering

amplitudes of a single atom for K^0 and $\overline{K^0}$, respectively. This adds a scattering term to the effective Hamiltonian of the system:

$$\mathcal{H}_{scat} = -2\,N\,\pi\,\beta\,\gamma \begin{pmatrix} \frac{f}{k} & 0 \\ 0 & \frac{\bar{f}}{k} \end{pmatrix} . \tag{1.11}$$

Here N is the number density of the scatterers, k is the kaon momentum, and β and γ are the usual relativistic parameters ($\beta = v/c; \gamma = 1/\sqrt{(1-\beta^2)}$). The result is new eigenstates for the forward scattering kaons. After solving the new eigensystem, the resulting time evolution matrix in the K_S, K_L basis is (assuming **CPT**):

$$e^{-\left(\frac{\bar{\Gamma}}{2}+Im(g_+)\right)\tau} \begin{pmatrix} \cosh(i\delta\tau) - \frac{h}{\delta}\sinh(i\delta\tau) & \frac{g_-}{\delta}\sinh(i\delta\tau) \\ \frac{g_-}{\delta}\sinh(i\delta\tau) & \cosh(i\delta\tau) + \frac{h}{\delta}\sinh(i\delta\tau) \end{pmatrix} , \tag{1.12}$$

where:

$$\begin{aligned} h &= -\frac{\Delta m}{2} - \frac{i\Delta\Gamma}{4} , \\ \bar{\Gamma} &= \frac{\Gamma_S + \Gamma_L}{2} , \\ g_\pm &= \pi N \frac{(f \pm \bar{f})}{k} , \text{ and} \\ \delta &= \sqrt{h^2 + g_-^2} . \end{aligned} \tag{1.13}$$

There is a whole lot of physics in this solution. For an incident K_L beam, the resulting output beam has a mixed amplitude, which can be written as $\sim|K_L\rangle + \rho|K_S\rangle$. This is the definition of the regeneration amplitude, ρ. Although this full matrix description will be used in all subsequent analysis, the thick regenerator formula is a very good approximation and demonstrates the relevant mechanisms

we will exploit in our analysis:

$$\begin{aligned} \rho &= i\pi NL\frac{f-\bar{f}}{k}g(L)\ , \\ g(L) &= \frac{1-e^{-i(\lambda_S-\lambda_L)\frac{L}{\beta\gamma}}}{i(\lambda_S-\lambda_L)\frac{L}{\beta\gamma}}\ , \text{ and} \\ \lambda_{S,L} &= m_{S,L}-\frac{i}{2}\Gamma_{S,L}\ . \end{aligned} \tag{1.14}$$

The function $g(L)$ depends on geometry alone. Equation 1.14 shows the essential dependence that the phase of ρ has on the phase of $f-\bar{f}$. This dependence is necessary to proceed with measurements of the **CP** violating phases

$$\phi_\rho = \frac{\pi}{2}+\phi_{f-\bar{f}}+\phi_g\ . \tag{1.15}$$

1.3 The CP Violating Phases

To quantify **CP** violation, KTeV observed the decay rates of the kaon system. Specifically, the ratio of the decay amplitudes of K_S and K_L to various final states (FS) plays a huge role and is given the name η,

$$\eta_{FS} = \frac{\langle FS|\mathcal{H}|K_L\rangle}{\langle FS|\mathcal{H}|K_S\rangle}. \tag{1.16}$$

We will show that η_{+-} and η_{00} (short hand for $\eta_{\pi^+\pi^-}$ and $\eta_{\pi^0\pi^0}$) are measures of **CP** violation, and their phase, if **CPT** is conserved, is prescribed to be 'very near' the super-weak phase, as constrained by the magnitude of direct **CP** violation. To do so, we first introduce direct **CP** violation. Assuming **CPT** symmetry,

$$\eta_{+-} = \frac{\epsilon_K\langle\pi^+\pi^-|\mathcal{H}|K_1\rangle+\langle\pi^+\pi^-|\mathcal{H}|K_2\rangle}{\langle\pi^+\pi^-|\mathcal{H}|K_1\rangle+\epsilon_K\langle\pi^+\pi^-|\mathcal{H}|K_2\rangle} \text{ and}$$

$$\eta_{00} = \frac{\epsilon_K \langle \pi^0\pi^0|\mathcal{H}|K_1\rangle + \langle \pi^0\pi^0|\mathcal{H}|K_2\rangle}{\langle \pi^0\pi^0|\mathcal{H}|K_1\rangle + \epsilon_K \langle \pi^0\pi^0|\mathcal{H}|K_2\rangle} \; . \tag{1.17}$$

Now the decay amplitudes are decomposed into isospin states,

$$\begin{aligned} |\pi^+\pi^-\rangle &= \sqrt{\frac{2}{3}}|I=0\rangle + \sqrt{\frac{1}{3}}|I=2\rangle \; , \text{ and} \\ |\pi^0\pi^0\rangle &= -\sqrt{\frac{1}{3}}|I=0\rangle + \sqrt{\frac{2}{3}}|I=2\rangle \; . \end{aligned} \tag{1.18}$$

Let δ_I represent the phase shift due to final state interactions via the strong force and A_I be the isospin dependent part of the decay amplitude. Then,

$$\begin{aligned} \langle I=0|\mathcal{H}|K^0\rangle &= A_0 e^{i\delta_0} \; , \text{ and} \\ \langle I=2|\mathcal{H}|K^0\rangle &= A_2 e^{i\delta_2} \; , \end{aligned} \tag{1.19}$$

and under **CPT**,

$$\begin{aligned} \langle I=0|\mathcal{H}|\overline{K^0}\rangle &= A_0^* e^{i\delta_0} \; , \text{ and} \\ \langle I=2|\mathcal{H}|\overline{K^0}\rangle &= A_2^* e^{i\delta_2} \; . \end{aligned} \tag{1.20}$$

After some simplification (see [7] for details), the result is,

$$\begin{aligned} \eta_{+-} &= \epsilon_K + \frac{\epsilon'}{1+\omega/2} \; , \\ \eta_{00} &= \epsilon_K - 2\frac{\epsilon'}{1-\omega/2} \; , \\ \epsilon' &= \frac{iIm(A_2)}{\sqrt{2}A_0} e^{i(\delta_2-\delta_0)} \; , \text{ and} \\ \omega &= \frac{Re(A_2)}{A_0} e^{i(\delta_2-\delta_0)} \; . \end{aligned} \tag{1.21}$$

During this simplification the K^0, $\overline{K^0}$ relative phase (ϕ from Equation 1.2) has been set such that A_0 is real. Note that measurements of the final state interactions show $\delta_2 - \delta_0 = -42^\circ \pm 4^\circ$ [8], resulting in ϵ'/ϵ having a very small imaginary component (because it is largely parallel to ϕ_{SW}).

If we now relax the **CPT** constraint any number of problems might arise. For example, imagine that **CPT** violation were, like **CP** violation, larger in the mixing matrix than in the decay amplitudes. Then:

$$\begin{aligned} \eta_{+-} &= \epsilon_K - \delta_K + \frac{\epsilon'}{1+\omega/2} \text{ , and} \\ \eta_{00} &= \epsilon_K - \delta_K - 2\frac{\epsilon'}{1-\omega/2}. \end{aligned} \tag{1.22}$$

Noting that according to Equation 1.10, δ_K will be orthogonal to ϵ_K, any observation of non-zero $\phi_{+-} - \phi_{SW}$ is a signature of **CPT** violation. This test motivates the study of this phase with the best precision available.

1.4 Measuring CP Sensitive Phases

The strategy that the KTeV collaboration employs for measuring the **CP** sensitive phases hinges on the change in decay rate as a function of time downstream of the regenerator. For kaons emerging from a regenerator with flux Ψ, the decay rate is:

$$\begin{aligned} R &= |\langle FS|\Psi(\tau)\rangle|^2 \\ &= \Psi \left| e^{-\tau(\frac{\Gamma_L}{2}+im_L)} \langle FS|K_L\rangle + e^{-\tau(\frac{\Gamma_S}{2}+im_S)}\rho \langle FS|K_S\rangle \right|^2 \\ &= \Psi |\langle FS|K_S\rangle|^2 \left(e^{-\Gamma_L\tau} + |\frac{\rho}{\eta}|^2 e^{-\Gamma_S\tau} + |\frac{\rho}{\eta}| e^{-(\Gamma_S+\Gamma_L)\tau/2} \cos(\Delta m\tau + \phi_\rho - \phi_\eta) \right). \end{aligned} \tag{1.23}$$

The result is that a careful measurement of the evolution of the decay rate of $K \to \pi^+\pi^-$ allows the extraction of the phase term, $\phi_\rho - \phi_{+-}$. In order to perform our sensitive test of **CPT**, by comparing ϕ_{+-} with the superweak phase, the regeneration phase must be determined precisely.

1.5 Analyticity

The technique KTeV employs to extract ϕ_ρ is to measure the magnitude of ρ as a function of momentum and to infer the phase using the analyticity of the scattering amplitudes and our understanding of the entire spectrum of kaon-nucleon interactions [7, 9]. How is this phase determined? At the heart of the scattering theory is the expansion of the scattered field into a series of outgoing waves. Starting from the fundamental assumptions of weak causality and **CPT** conservation, field theory predicts that the phase of the forward amplitude is related to its magnitude [10]. The mathematics behind this relationship begins with the Titchmarch theorem [11], which applies to ordinary functions, and extends its results to generalized functions [12]. Our analytic functions are the scattering amplitudes f and $\bar{f}$ from Equation 1.11 above. These are each analytic functions of the center of mass energy, $\sqrt{s}$. The alert reader will note that E, p, and $\sqrt{s}$ are not the same quantity; however, at our energies they are very close. The following sketch will play somewhat fast and loose with these terms. See Block and Cohn [13] on this topic for a more rigorous treatment.

Since the **C**, **P** and **T** conserving strong force completely dominates the kaon-nucleon scattering process, the scattering amplitudes are related (in similar fashion

to the $K^0 - \overline{K^0}$ system) by:

$$f(E) = -\bar{f}(-E) \ . \tag{1.24}$$

For the purpose of studying regeneration, it is easiest to symmetrize the system and work with:

$$f_{\pm}(E) = \frac{f(E) \pm \bar{f}(E)}{2} \ . \tag{1.25}$$

These terms have already been seen to be the relevant players in an analysis of regeneration. Their symmetry, namely,

$$f_{\pm}(E) = \pm f_{\pm}(-E) \ , \tag{1.26}$$

can be shown to simplify the relations of analyticity. The relationship between real and imaginary parts mandated by the Cauchy-Riemann relations can be made explicit:

$$Ref_+(E) = ERef_+(0) + P\frac{2E^2}{\pi}\int_0^\infty \frac{Imf_+(x)}{x(x^2-E^2)}\,dx \ , \text{ and} \tag{1.27}$$

$$Ref_-(E) = E\frac{d}{dx}Ref_-(x)|_{x=0} + P\frac{2E^3}{\pi}\int_0^\infty \frac{Imf_+(x)}{x^2(x^2-E^2)}\,dx \ . \tag{1.28}$$

This form reveals a key feature of the scattering amplitude. Contributions to the total cross-section at all energies (proportional to the imaginary part of the amplitude) contribute to the phase at a given energy. The weight with which they contribute diminishes rapidly both as the energy grows and as the energy difference grows, but the magnitude of such effects can have an impact on the application of these relations. The objection, raised by Kleinknecht and Luitz [14], is that the

integral of Equation 1.28 has no upper limit and that consequently an exotic resonance above our energy could feed down into our momentum range and foul our measurement. Careful analysis of this notion has severely limited the magnitude of any such contribution (see Briere and Winstein [15]).

We measure $|f_-|$ quite well in our momentum range and it is seen to be very close to obeying a pure power law ($\sim p^\alpha$). In this case it is useful to recast the Equations 1.27 and 1.28 into the so called Derivative Analyticity Relations [16, 17, 18],

$$\begin{aligned} Re\left(\frac{f_+}{p^\alpha}\right) &= \tan\left(\frac{\pi}{2}\left(\alpha - 1 + \frac{\partial}{\partial \ln(p)}\right)\right) Im\left(\frac{f_-}{p^\alpha}\right) \text{ , and} \qquad (1.29) \\ Re\left(\frac{f_-}{p^\alpha}\right) &= \tan\left(\frac{\pi}{2}\left(\alpha + \frac{\partial}{\partial \ln(p)}\right)\right) Im\left(\frac{f_-}{p^\alpha}\right) . \qquad (1.30) \end{aligned}$$

The notation involving the tangent of an operator is shorthand for the appropriate power series expansion. It is worth noting that this operator is linear in an unusual double sense. Either the sum or the product of any two functions satisfying Equation 1.30 is itself a solution. Substituting our power law into this equation, namely,

$$\begin{aligned} \Re(f_-) &= C \cdot p^\alpha \cdot \sin(\phi_{f_-}) \text{ , and} \\ \Im(f_-) &= C \cdot p^\alpha \cdot \cos(\phi_{f_-}) \qquad (1.31) \end{aligned}$$

gives the relation between the power and the phase that to first order describes f_-:

$$\phi_{f_-} = -\frac{\pi}{2}(1+\alpha) . \qquad (1.32)$$

The measured power law behavior is very close to what is expected based on extrapolating Regge-pole exchange theory from lower energies up to our energy

range. Regge-pole theory explains the scattering amplitude as an expansion in terms of the first order T-channel exchange of a number of hadronic resonances. The ω, ρ, A_2 and f, correspond to observed resonances. The exceptional Reggeon is the Pomeron, P, which is structurally more complicated, but motivated by the observed rise of hadronic cross-sections at high energy. Each of these intermidiaries carries certain quantum numbers which bear on their behavior under symmetry operations. For our regenerator, which is very nearly isoscalar (Dominantly ^{12}C), the contribution to regeneration of all poles but the ω are removed. Three effects leave some residual non-power-law behavior. First, our regenerator is not a perfect isoscalar. The presence of hydrogen in addition to carbon allows a small contribution from ρ-exchange to contribute as well. Second, the minute difference in energy dependence of the cross-sections of K-n and K-p causes nuclear screening to induce a slight modification of the momentum dependence of f_-. The principal uncertainty that remains is the contribution from *inelastic* screening. Within a nucleus, a scatter can proceed through an intermediate state that is not a kaon. Model dependence in the treatment of this term dominates the uncertainty in the shape of f_-.

1.6 Phase in K_{e3} Asymmetry

To measure the regeneration phase independently of obsevations of the $K_{\pi 2}$ final state, we look to the charge asymmetry of K_{e3} decays. The relative decay rates for $K \to \pi^- e^+ \bar{\nu_e}$ and $K \to \pi^\pm e^\mp \nu_e$ can be computed. First order diagrams of the decay are shown in Figure 1.3. The next two sections develop treatments of the K_{e3} asymmetry, first assuming that these two diagrams are the only relevant processes, and then imagining what the first order effect of the higher-order diagrams would be. The first case will provide a mechanism for extracting the regeneration phase,

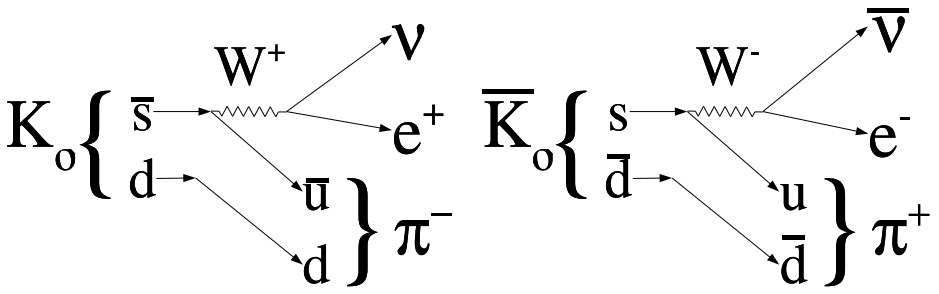

Figure 1.3: First Order Diagrams for $K \to \pi^- e^+ \bar{\nu}_e$ and $K \to \pi^+ e^- \nu_e$.

ϕ_ρ, and the K_L asymmetry, δ_L. The second case will introduce the parameter x as a measure of the contribution of the higher-order diagrams and reveal our sensitivity to this complex parameter.

1.6.1 When $\Delta S = \Delta Q$

The lepton charge effectively tags the strangeness of the parent kaon. In the context of the decay rate of Equation 1.23, we have,

$$\begin{aligned} \eta_{\pi^- e^+ \nu} &= 1, \\ \eta_{\pi^+ e^- \bar{\nu}} &= -1, \\ \left\langle \pi^- e^+ \nu | K_S \right\rangle &= 1 + \epsilon_K \ , \text{ and} \\ \left\langle \pi^+ e^- \bar{\nu} | K_S \right\rangle &= 1 - \epsilon_K \ . \end{aligned} \tag{1.33}$$

The charge asymmetry is defined by Equation 1.34,

$$\delta(\tau) = \frac{R(\pi^- e^+ \nu) - R(\pi^+ e^- \overline{\nu})}{R(\pi^- e^+ \nu) + R(\pi^+ e^- \overline{\nu})} \ , \tag{1.34}$$

which after a good deal of simplification becomes:

$$\delta(\tau) \simeq 2\,|\rho|\,e^{-\frac{\Gamma_S-\Gamma_L}{2}\tau}\cos(\Delta m\tau+\phi_\rho)+2\cdot\Re(\epsilon_K)\;. \tag{1.35}$$

Here we can see that the phase of the oscillating term is now precisely a measure of the regeneration phase. The advantage of having only a single pion in the decay products is that no final state interactions alter this phase. Note that, as expected, the prediction for the asymptotic asymmetry, δ_L, is $2\cdot\Re(\epsilon_K)$. By fitting the evolution of this asymmetry precisely, we can extract both the phase and δ_L.

Carithers [19] measures $\phi_{f-\bar{f}}$ for carbon by fitting the observed asymmetry using this functional form. At the lower energy (4.5-11.2 GeV) of that experiment, the value extracted was $-40.9^\circ \pm 2.6^\circ$. With improved statistics we can make a similar measurement in our higher momentum range and reduce the error by a factor of 2.

In addition, the asymmetry at large proper time can be measured precisely enough to eclipse all prior measurements. Although it is not as statistically powerful as the measurement made by analyzing KTeV's data without the presence of the regenerator, our value will contribute significantly to the overall world average.

1.6.2 When $\Delta S \neq \Delta Q$

What happens when we release the $\Delta S = \Delta Q$ rule? The typical approach to allowing such a violation is to introduce x and its **CPT** conjugate, $x^\star$, defined (in the context of **CPT** conservation) as follows,

$$\begin{aligned} x &= \frac{\left\langle K^+_{e3}|M|\overline{K^0}\right\rangle}{\left\langle K^+_{e3}|M|K^0\right\rangle}\;, \text{ and} \\ x^\star &= \frac{\left\langle K^-_{e3}|M|K^0\right\rangle}{\left\langle K^-_{e3}|M|\overline{K^0}\right\rangle}\;. \end{aligned} \tag{1.36}$$

Allowing x to be non-zero and propagating through our equations for the asymmetry (to first order in x and $|\rho|$), the new expression for the proper time evolution of the asymmetry is:

$$\delta(\tau) \;=\; (1+2\cdot\Re(x))\left(2\,|\rho|\,e^{-\frac{\Gamma_S-\Gamma_L}{2}\tau}\cos(\Delta m\tau+\phi_\rho)+2\cdot\Re(\epsilon)\right)\;. \quad (1.37)$$

Note that no first order $Im(x)$ terms remain.

The CPLEAR experiment's measurement, $\Re(x) = (-18 \pm 41 \pm 45) \times 10^{-4}$[20], is the best current limit on this parameter. The Standard Model predicts a tiny value, $\sim 10^{-8}$, hence any observable deviation from zero at the current level of precision would uncover a dramatic input from new physics.

1.7 Summary

We now have three tools in hand to take precise measurements of the asymmetry evolution behind the KTeV regenerator and place them into the context of the Standard Model. Each tool addresses very different physics. Precise measurement of δ_L pushes the state of the art in understanding the CKM unitarity triangle. Seeking limits on $\Re(x)$, in essence, searches for exotic interactions that would break our current understanding of semi-leptonic kaon decay. Checking $\Delta\phi_\rho$ probes **CPT** and causality through the analyticity relations, although any observed violation might also be attributable to the impact of an exotic resonance on kaon-nucleon scattering.

Figure 1.4 shows a flow diagram for the way forward. Chapter 2 will introduce the KTeV detector and show that it is well suited to observe the decays needed, and that although the neutrino escapes, the observed part of the decay will have enough kinematic information to allow us to measure the time evolution of the asymmetry.

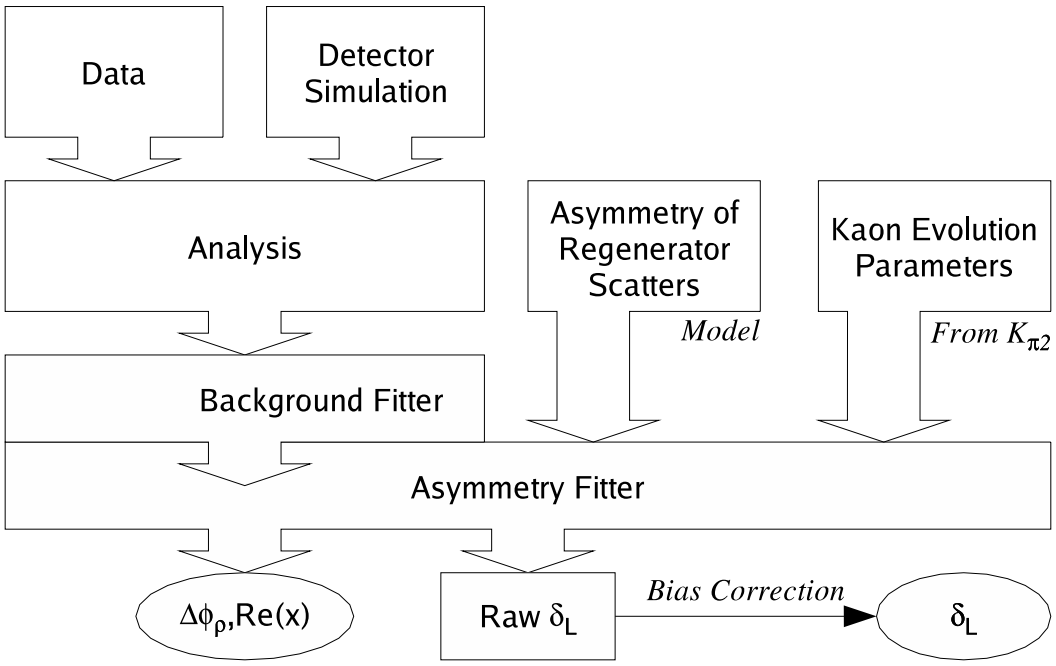

Figure 1.4: Flow Chart of the Analysis

Chapter 3 will descibe the 1997 run and the methods used to record the decays in the detector. Chapter 4 will give the details of the analysis cuts used to select a clean, well understood sample of K_{e3} events. The detailed detector simulation is critical in understanding the background and in quantifying the correlation of observable quantities in the event sample with the proper time. Chapter 5 will describe the simulation, illustrate its accuracy both for the signal and for the scattered backgrounds, and discuss the impact of the non-K_{e3} backgrounds observed. Chapter 6 will discuss the fitter and detail the careful allowances made for uncertainties in the background. Chapter 7 will catalog the broad range of systematic concerns and quantify their impact on the final fit results. Finally, Chapter 8 will summarize and put our results in the context of past measurements.

CHAPTER 2

EXPERIMENTAL TECHNIQUE

The KTeV detector has two configurations. When set up for E799, the focus is on rare decays of the K_L and Λ. When set up for E832, the focus is on effects related to the regenerator. The E832 data is of interest in this analysis. In order to obtain the best possible statistics for the $\Re(\epsilon'/\epsilon)$ measurement, the E832 configuration is a streamlined $K \to 2\pi$ event collection machine. The large fluxes and precise measurements required for this effort also provide an ideal source of regenerator K_{e3} decays.

The regenerator K_{e3} analysis faces two major hurdles due to the undetectable neutrino and resulting incomplete reconstruction of the parent kaon's momentum. First, a probabilistic approach to the proper time of the decay must be employed since the total momentum of the parent is ambiguous. Second, non-coherent scatters in the regenerator, which can be removed to a large degree in the 2π analysis by limiting the transverse momentum of the parent, remain as a very large background since this kinematic handle is unavailable.

This chapter will give a brief overview of the KTeV apparatus. Then the strategy for addressing the twin problems of incomplete reconstruction will be introduced. A description of the technique used to cancel geometric acceptance differences between oppositely charged decays will follow. Finally, a brief discussion of residual charge asymmetries is included.

2.1 The KTeV Apparatus

The KTeV apparatus is spread over two large experimental halls on the Fermilab site. The upstream hall is dedicated to turning the high energy, high flux proton beam provided by the TeVatron into, clean, high flux kaon beams. The downstream hall houses the active portion of the KTeV detectors. Sections 2.1.1 describes the target hall, and Section 2.1.2 describes the active detector elements.

2.1.1 Beamline

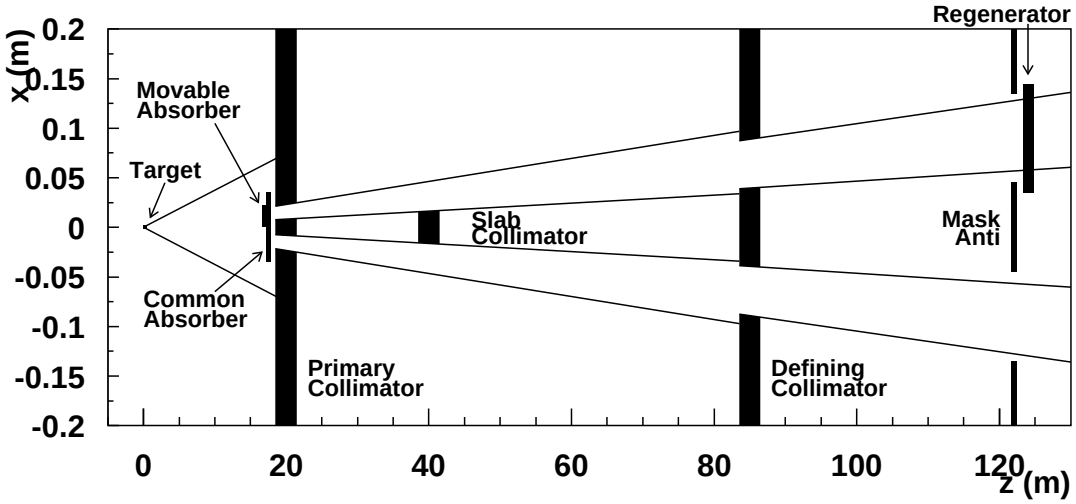

Figure 2.1: Geometry of the KTeV secondary beamline. The movable absorber and regenerator articulate between the east ($x < 0$) and west ($x > 0$) beams at the conclusion of each spill. Note the disparity in scales between the x and z axis.

The KTeV beamline, pictured in Figure 2.1, is optimized to produce two clean, high flux K_L beams. For 20 seconds out of every minute the TeVatron provides a 900 GeV proton beam focused on the KTeV target. Each minute long cycle is referred to as a spill. Within the spill, protons arrive in 1-2 ns "buckets" at 19 ns intervals. Typical proton fluxes as measured upstream of the target were on

the order of $1 - 5 \times 10^{12}$ per spill or $1000 - 5000$ per bucket. These protons hit a $3 \times 3 \times 300$ mm beryllium oxide target, producing copious secondaries of all varieties. The target serves as the origin of the KTeV coordinate system, with Z-axis oriented in the secondary beam direction, Y-axis pointing up, and the X-axis increasing toward detector "west". Large magnets immediately downstream of the target and between the primary and slab collimators (not shown in the figure) sweep away all charged particles. A common absorber removes the photon component as the beams enter the collimation system. Twenty-eight meters downstream of the target the entire beamline and decay region is evacuated. The collimators form 2 beams, which by 120 meters downstream of the target are dominantly K_L and neutrons with some residual neutral hyperons.

The $\Re(\epsilon'/\epsilon)$ measurement is statistically best served by equal numbers of regenerator and vacuum decays. Given the same K_L flux, the regenerator beam has a much higher rate of 2π decays; therefore, a movable absorber shadows the regenerator, which alternates between the east and west beams on a spill by spill basis. The regenerator kaons, which this analysis focuses on, traverse 18 inches of beryllium in the movable absorber plus 20 inches of beryllium and 3 inches of lead in the common absorber. After $\sim$100 meters of additional flight to allow the K_S component to decay away, the resulting K_L beam has a spectrum with a peak flux near 50 GeV, falling to half the peak below 30 GeV and above 85 GeV.

2.1.2 Detector

Figure 2.2 shows the layout of the detector. Its active elements include: the regenerator, which is effectively part of the beamline, in addition to being a detector element; the charged spectrometer, responsible for the measurement of all components of the charged particle momenta; the calorimeter, optimized for the measurement of pho-

ton positions and energies but highly effective as a tool for differentiating between pions and electrons; and the extensive veto systems, responsible for rejecting events with products not fully contained within the sensitive portions of the detector. This section will address each of these four systems in turn.

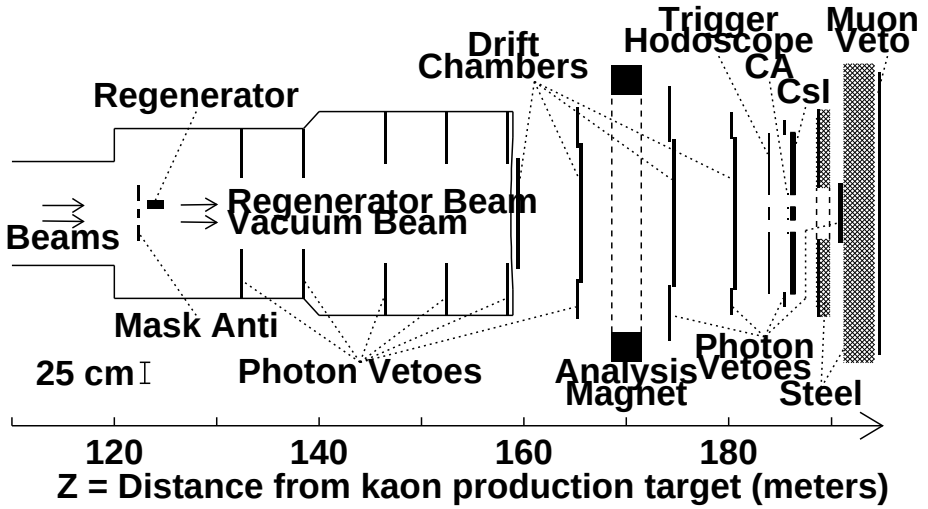

Figure 2.2: Plan View of the KTeV Detector

The Regenerator

The primary role of the regenerator is to convert incident K_L particles into a well understood K_L and K_S mixture. The regenerator is composed of a stack of 84 $10 \times 10 \times 2$ cm blocks of scintillator (density 1.032 g/cm^3, composition: carbon:hydrogen::1:1.1 by weight) each viewed by two phototubes. At the end is a final $10 \times 10 \times 2$ cm block composed of alternating 5.6 mm layers of lead (density 11.35 g/cm^3) and 4 mm layers of scintillator, also viewed by a pair of phototubes.

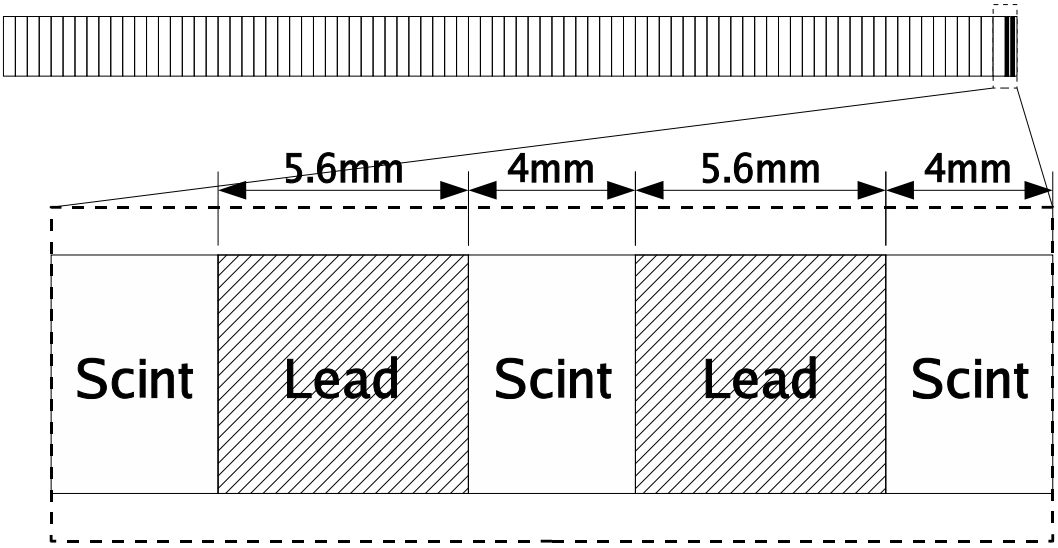

Figure 2.3: The full 168 cm KTeV regenerator is depicted on top. The final module is expanded below.

Figure 2.3 shows the geometry. The resulting combination is a total of 1.83 interaction lengths.

Kaons emerging from the regenerator can be categorized by their scattering as either coherently, diffractively or inelastically regenerated (although these will be subdivided later in this thesis). Inelastically regenerated kaons scatter off individual nuclei, often resulting in a small hadronic shower. Inelastic events are by far the most numerous. By instrumenting the regenerator, the hadronic showers can be detected and most of the inelastic scatters vetoed (along with internal and upstream decays). Coherently regenerated kaons are the purely forward scattered source that this analysis is interested in. Their production is $\sim$100 times smaller than the inelastic events. Diffractively regenerated kaons have scattered off of one or more atomic nuclei without causing their disintegration. They are outnumbered by the coherently regenerated kaons by $\sim$5:1 but do not trigger the regenerator veto.

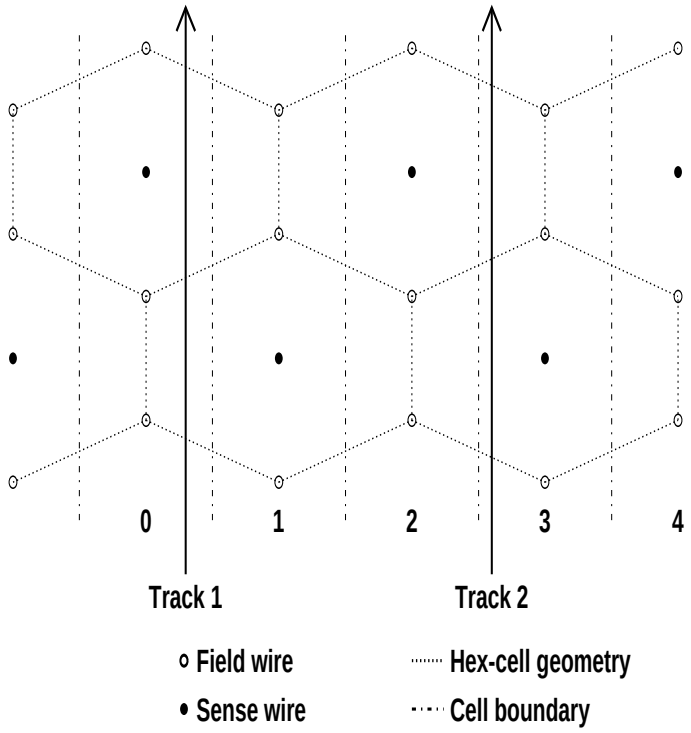

Figure 2.4: Drift Chamber Cell Geometry

The observable decay products from a K_{e3} decay are the pion and the electron. These must be reconstructed as precisely as possible. The drift chambers depicted in Figure 2.2 are responsible for this task. Each of the four chambers has two layers of sense wires, spaced by 12.7 mm, offset by 6.35 mm, aligned with the x-axis and two similar layers of sense wires aligned with the y-axis. Each sense wire sits in the center of a hexagonal cell of field wires (see Figure 2.4) which are held at high voltage ($\sim$2450 V). As a relativistic charged particle traverses the chamber, it ionizes the argon-ethane gas and the resulting electrons drift toward the sense wire at roughly 50 microns/ns. Very near the sense wire, the drifting electrons begin ionizing the gas creating an avalanche that results in a detectable pulse on the sense wire. This pulse

is then used to start a time delay counter (TDC) with 1/2 ns precision. The result of arduous calibration efforts (described in Graham [7]) is that a hit pair localizes a charged particle with ∼90 micron precision. The analysis magnet provides a uniform momentum kick of $\sim 412\,\mathrm{MeV}/c$ to the passing particles. By matching upstream and downstream spectrometer tracks at the bend plane of the magnet, a full trajectory is mapped out allowing the sign of the charge and magnitude of the momentum to be reconstructed.

The Calorimeter

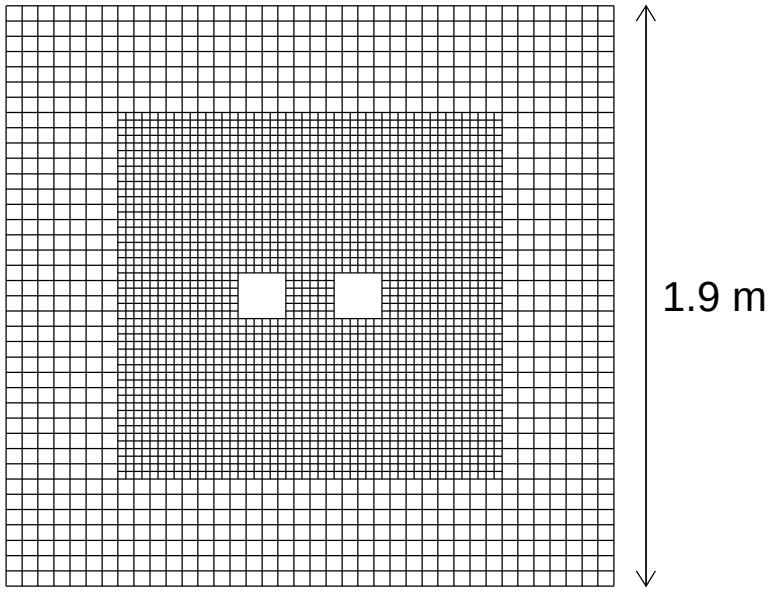

Figure 2.5: CsI Calorimeter Geometry

The calorimeter, as shown in Figure 2.5, is a stack of 3100 pure cesium iodide crystals, 50 cm (27 radiation lengths) in depth, composing a 1.9 m square with two 15 cm square beam holes. The principal role of this detector is to precisely reconstruct photons from neutral mode decays ($K \rightarrow n\pi^0$). As a result, extreme measures

have been taken to ensure that the crystal energy response is highly linear and that the position of clusters formed by electromagnetic showers can be determined with great precision. To accomplish this high level of performance, a number of experimental tricks are used. Unfiltered, the scintillation light from pure undoped CsI consists of about 80% photons from a fast ($\sim$36 ns) decaying source, with the remaining photons from a longer lived ($\sim$1 μs) excited state of the material. By applying a UV filter to selectively remove the long component (480 nm wavelength) while retaining the short component (315 nm), the ratio is improved to 90%. This reduces the pile-up effects, analogous to the screen streaks that high end LCD screen makers warn you against. The light output is $\sim$20 photons per MeV of energy. Each crystal is viewed by a photomultiplier tube. The trigger system uses the individual dynode outputs as a fast identifier of events of interest. The anode outputs are digitized by a custom digitizer with 16 bits of dynamic range positioned inches from the phototube. Six samples are collected at 53 MHz capturing $\sim$96% of the fast scintillation component. For calibration purposes a Nd:YAG laser, through a system of optical fibers, could feed controlled light pulses to every crystal. The thesis of V. Prasad [21] is the definitive source on the full calibration of both the electronics and the response of the crystals themselves. The result is an array with a resolution of $\sigma_E/E \simeq 2\%/\sqrt{E} \oplus 0.4\%$ for E measured in GeV.

For the purpose of the K_{e3} measurement, the calorimeter is used to distinguish pions from electrons by comparing the energy of the cluster that matches the downstream particle track to the measured momentum. Because the electron electromagnetically showers in the calorimeter, it will deposit all of its energy. In contrast, the pion will either leave only ionization energy or will begin a hadronic shower which is not fully contained by the CsI crystals. Note that in rare cases the pion can charge exchange and the resulting chain $\pi^{\pm} \to \pi^0 \to 2\gamma \to$ EM shower will result in deposit

of all of the pion energy in the calorimeter. This leads to an event loss that will be addressed later.

The Veto Systems

This analysis relies on the veto systems to fulfill three roles. First, they sharply define the geometric apertures that govern the acceptance of the detector. Second, they reduce the overall trigger rate to a manageable level. Third, they help to eliminate backgrounds associated with events where particles escape the combined fiducial volume of the CsI and chamber systems.

The system includes 9 detectors, Ring Counters (RC6-9), Spectrometer Antis (SA1-4) and the CsI Anti, which surround the outer aperture of the detector spaced from Z of 132 m through 184 m. Each is a sandwich of alternating lead and scintillator layers of 16 radiation lengths. Photons convert and shower in the lead depositing energy in the scintillator, where phototubes measure the light output. Thresholds on the light output are set such that even minimum ionizing pions and muons escaping the fiducial volume cause an event to be rejected. The Mask Anti (MA) is a similar detector upstream of the regenerator. Behind the CsI is the Back Anti (BA), another 10 radiation length veto counter that removes events in which particles are lost down the beam hole. A large hodoscope behind an additional 4 m of steel (Z = 192 m) is used to veto muons. To provide a sharp edge for the inner aperture in neutral mode, the Collar Anti (CA) surrounds each beam hole immediately in front of the calorimeter, eclipsing the inner 1.5 cm of the crystals. Although it functions similarly to the other veto systems, its construction uses tungsten in place of the lead to allow more precise machining of this critical aperture, as well as to fit its 8.7 radiation lengths in as small a space as possible.

2.2 Incomplete Reconstruction

While the detector described above is excellent at resolving all of the relevant kinematics of both the electron and the pion, the neutrino is lost. As a result two key parameters in the $K_{\pi 2}$ analysis, kaon momentum (P_K) and kaon transverse momentum (P_T), are not available in this analysis. The "most probable momentum" ($\hat{P}_K$) replaces P_K in determining the proper time of an event in this analysis. The large role that P_T usually plays in removing decays of scattered kaons must be divided among a number of kinematic variables sensitive to scattering in the regenerator.

2.2.1 Momentum Ambiguity

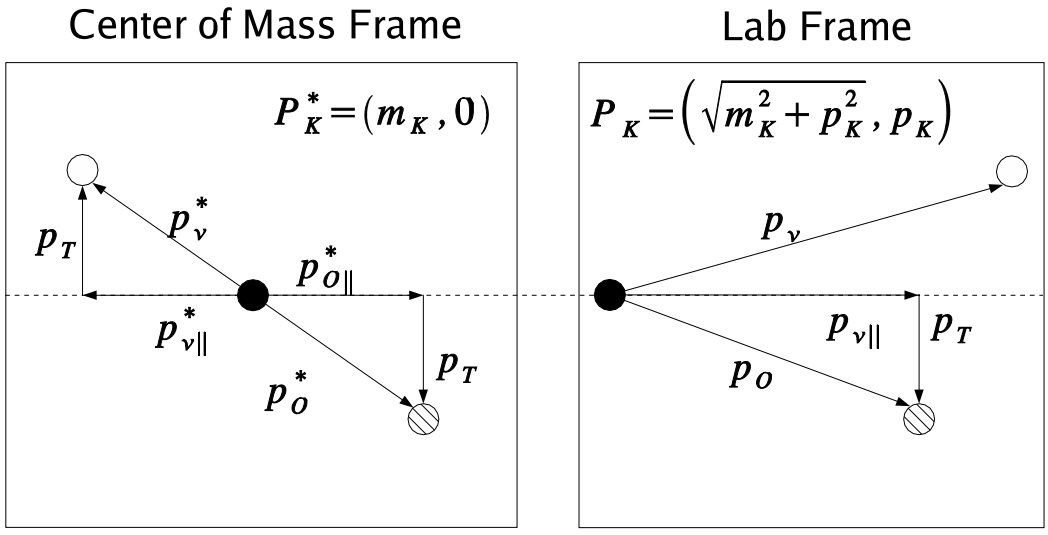

Figure 2.6: Kinematics of Impartial Reconstruction

What reconstruction can be done when there is missing momentum? Figure 2.6 shows a two body decay where one body is lost both in the lab frame and in the rest frame. Star superscripts label the rest frame kinematic quantities.

Begin with four-momentum conservation,

$$P_K = P_{OBS} + P_\nu \ . \tag{2.1}$$

Take the dot product with P_{OBS} and evaluate the left hand side in the center of mass frame:

$$m_K \cdot E^*_{OBS} = m^2_{OBS} + P_\nu \cdot P_{OBS} \ . \tag{2.2}$$

Evaluating the last term by squaring Equation 2.1 yields

$$m^2_K = m^2_{OBS} + m^2_\nu + 2P_\nu \cdot P_{OBS} \ . \tag{2.3}$$

Rearranging terms results in an expression for E^*_{OBS}:

$$E^*_{OBS} = \frac{m^2_K - m^2_\nu + m^2_{OBS}}{2m_k} \ . \tag{2.4}$$

Now observe that ${p^*_{OBS\|}}^2$ can be found using the Pythagorean theorem:

$${p^*_{OBS\|}}^2 + p^2_T = {E^*_{OBS}}^2 - m^2_{OBS} \ , \text{ whence} \tag{2.5}$$

$$\text{ARGUMENT} \equiv {p^*_{OBS\|}}^2 = \frac{(m^2_K - m^2_{OBS} - m^2_\nu)^2 - 4m^2_{OBS}m^2_\nu}{4m^2_k} - p^2_T \ . \tag{2.6}$$

This expression is often referred to as the ARGUMENT since it appears inside a square-root in many kinematic expressions. If all quantities are measured correctly, the ARGUMENT is constrained to be positive definite.

To find the momentum of the parent kaon we begin with the standard Lorentz

boost equations:

$$E^*_{OBS} = \gamma E_{OBS} - \beta\gamma P_{OBS\|} \quad (2.7)$$

$$P^*_{OBS\|} = \gamma P_{OBS\|} - \beta\gamma E_{OBS} \; . \quad (2.8)$$

Multiplying Equation 2.7 by $P_{OBS\|}/E_{OBS}$ and subtracting Equation 2.8 results in an expression for the boost factor:

$$\beta\gamma = \frac{E^*_{OBS}P_{OBS\|} - P^*_{OBS\|}E_{OBS}}{E^2_{OBS} - P^2_{OBS\|}} \; . \quad (2.9)$$

Using the relation $E^2_{OBS} - P^2_{OBS\|} = m^2_{OBS} + p^2_T$, and explicitly emphasizing that only the magnitude of $P^*_{OBS\|}$ is known, the result for the kaon momentum is:

$$p_K = \beta\gamma \cdot m_K = m_K \left(\frac{E^*_{OBS}P_{OBS\|} \pm P^*_{OBS\|}E_{OBS}}{m^2_{OBS} + p^2_T} \right) . \quad (2.10)$$

Interestingly, the relative probabilities of these two solutions are independent of any detector acceptances or efficiencies. In the limit of perfect detector resolution, they depend only on the relative magnitude of the parent momentum spectrum at the two solutions and the relative magnitude of the matrix element squared for the two solutions. Figure 2.7 shows these distributions and the reconstructed quantities from a typical event. The ratio is easily computed, given our best understanding of each of these functions:

$$R_P = \frac{\Phi(P_{HI}) \cdot \mathbf{M}(P_{HI})^2}{\Phi(P_{LO}) \cdot \mathbf{M}(P_{LO})^2} \; . \quad (2.11)$$

$\hat{P}_K$ is set equal to the low momentum solution when $R_P < 1$ and the high solution when $R_P > 1$. Cases where our guess is incorrect will dilute the sample and affect

the measured asymmetry. The exact method for accounting for this dilution will be described in Chapter 6. The basic idea is to use a detailed simulation of the detector acceptance to predict the distribution of true P_K that occupy each $(\hat{P}_K, Z)$ bin. The average asymmetry weighted by the flux in each bin is then compared to the measured asymmetry in that bin.

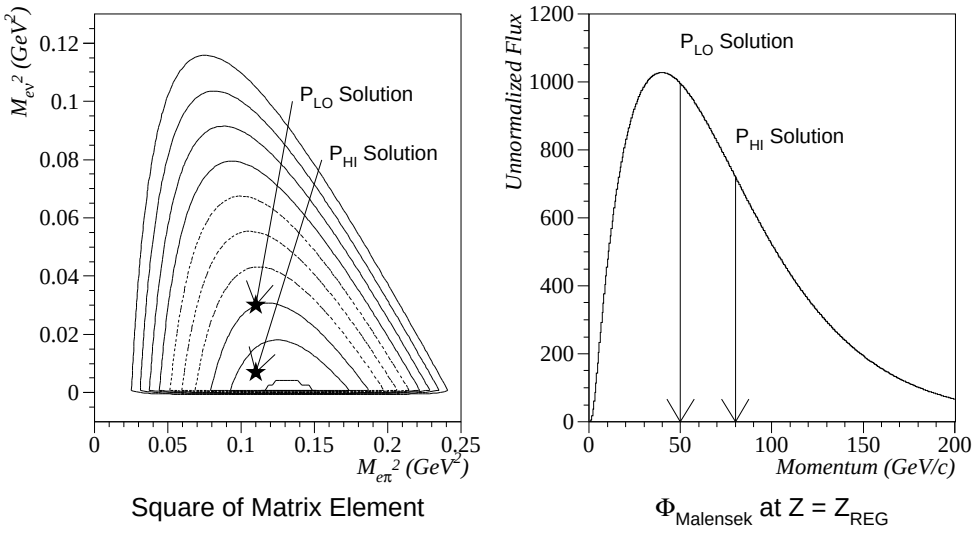

Figure 2.7: a) The figure on the left shows the contours of the K_{e3} matrix element. Reconstruction of the visible decay products reduces the phase space to a small allowable region around two points, one for the high momentum solution, one for the low momentum solution. b) The figure on the right shows the predicted momentum flux at the downstream edge of the regenerator. A typical pair of solutions are shown.

2.2.2 Incoherent Background

The computations in the preceding section provide a way to mitigate the impact of incomplete momentum reconstruction on computing the proper lifetime relevant to the physics at hand. However, the incomplete kinematic reconstruction also hinders

the removal of scattered events based on their large p_T^2. In this section we identify 5 kinematic variables that are sensitive to scattering, which we will use to reduce, study and model scattered events. The mechanism by which the distribution of these variables are factored into a final result will be described in Chapter 6.

The Variables p_{Te}^2, $p_{T\pi}^2$ and p_T^2

For a kaon at rest, simple kinematics limit the values of p_T^2 that any of the final state particles could have. Suppose that particle 1 is a decay product with angle θ to the direction of flight in the rest frame. We compute the transverse momentum as follows:

$$p_{T1}^2 = \sin^2(\theta)\left(\frac{m_K^2 + m_1^2 - m_2^2}{2m_K}\right)^2 - m_1^2 \,, \tag{2.12}$$

where m_2 is the mass of the remaining decay products. This quantity will be maximized when $\theta = \pi/2$ and m_2 assumes its minimum. This minimum occurs when the two particles in the recoil system are relatively at rest, resulting in a mass which is their simple sum. Therefore, the absolute maximum is:

$$(p_{1T}^{max})^2 = \left(\frac{m_K^2 + m_1^2 - (m_a + m_b)^2}{2m_K}\right)^2 - m_1^2 \,. \tag{2.13}$$

where a and b are used to label the particles in the recoil system. Table 2.1 shows the resulting maxima. These values are quite large compared to the typical p_T^2 distributions of the scattered kaons which tend to fall off as $e^{-C \cdot p_T^2}$ where C is of order 1000000 $(c/\mathrm{MeV})^2$ or larger. Each of these is measurable in the KTeV detector. Although the neutrino is not seen, we can equate its transverse momentum to that of the electron pion system.

Decay Product	$(p_T^{max})^2$
e	52562 $(\mathrm{MeV}/c)^2$
π	52562 $(\mathrm{MeV}/c)^2$
ν	52497 $(\mathrm{MeV}/c)^2$

Table 2.1: Maximum Obtainable p_T^2 Values

The RINGNUMBER Variable

Scatters can also be identified in cases where the decay vertex is displaced from the boundary of the kaon beam. In the analysis of $K \to \pi^0\pi^0$ decays, the center of energy of the event is formed at the calorimeter and compared to the extent of the beam. We borrow the terminology RINGNUMBER from this analysis [21]. In the K_{e3} case, a line is drawn from the target through the decay vertex to a point on the face of the CsI. The area (in cm^2) of the smallest square co-centered with the regenerator beam and containing this point is given the name RINGNUMBER. Since our beams are nearly perfect squares and the halo is quite well controlled, there is a steep decline in the distribution above a RINGNUMBER of $\sim$100. This variable is most effective at identifying scatters with low values of momentum and high values of Z-vertex.

The ARGUMENT Variable

The ARGUMENT defined in Equation 2.6 is the final variable sensitive to incoherent scattering we consider. This is a useful variable since mismeasurements can lead to small negative values while large negative values occur exclusively when kaon scattering falsifies the assumption that the line from the target to the vertex defines the direction of the parent.

Fitting Strategy

Measurements of these five different variables kick only a small fraction of decays of scattered kaons into the unphysical region. Neverthless, these variables play a very important role since the precise understanding of their behavior will be used to correctly account for the remaining incoherent background. The fitting strategy is twofold. First, float the parameters that relate to the normalization of the scattered background in order to best fit the sidebands in these sensitive distibutions. Second, trust the simulation to provide the correction for the inelastic background in the final fit to the asymmetry. This will require an extra layer of complexity in the fitting process; however, since the background is so large this added complexity is the only route to confidence.

2.3 Acceptance Cancelation

The geometric acceptance of the KTeV detector for a single magnet polarity is dramatically different for K^+_{e3} and K^-_{e3}. Models of the geometry are good but the analysis relies on an additional trick to minimize its dependence on the Monte Carlo simulation. Consider the '4-fold way' in which event counts are proportional to flux, acceptance, and a term from the underlying physics asymmetry. This can be expressed as follows:

$$\begin{aligned} N_{\downarrow\pm} &\sim \Phi_{\downarrow} A_{\downarrow\pm} \frac{1 \pm \delta}{2} \text{ , and} \\ N_{\uparrow\pm} &\sim \Phi_{\uparrow} A_{\uparrow\pm} \frac{1 \pm \delta}{2} \text{ .} \end{aligned} \tag{2.14}$$

where N is the number of events observed, Φ is the kaon flux, A is the detector acceptance, δ is the charge asymmetry of the underlying physics, and the subscripts indicate the magnet polarity for the sample ($\uparrow\downarrow$) and the lepton charge ($\pm$).

The central conjecture in the 4-fold way is that the acceptance in an ideal experiment depends only on geometry. That is to say the events with left bending electrons and the events with left bending positrons have identical acceptance:

$$\begin{aligned} A_{\uparrow +} &= A_{\downarrow -} \ , \\ A_{\uparrow -} &= A_{\downarrow +} \ . \end{aligned} \tag{2.15}$$

In that ideal case, a carefully chosen ratio,

$$R^2 \ = \ \frac{N_{\downarrow +} \cdot N_{\uparrow +}}{N_{\downarrow -} \cdot N_{\uparrow -}} = \left(\frac{1+\delta}{1-\delta} \right)^2 \ , \tag{2.16}$$

allows the complete cancellation of detector acceptance.

In the real experiment four effects corrupt this cancellation:

1. The magnetic field is not reversed perfectly. This will result in an imperfect cancellation of geometric effects due to the slightly different field for positive and negative polarity of the magnet.

2. The positive and negative polarity data cannot be taken simultaneously. Drifts in the calibration, beam, veto performance and detector resolution may impact the two polarities differently.

3. The detector is not charge symmetric. Like all detectors, the KTeV detector has a large preponderance of electrons over positrons. At the electron energies

in question, the e^+/e^- difference between the cross-section with the detector materials will slightly alter the efficiency of one charge relative to the other.

4. The detector is not isoscalar. Most critically, the CsI calorimeter is made of more neutrons than protons. Therefore there will be a difference in the efficiency of positive pions and negative pions.

All of these effects will be shown to be acceptably small.

2.4 Residual Charge Asymmetry

A number of effects unrelated to geometry will have an impact on the charge asymmetry measured in the detector. The vacuum beam $K_L \to \pi e \nu$ decays have none of the complications associated with the regenerator and are an ideal sample for characterizing these effects. KTeV has published 'A Measurement of the K_L Charge Asymmetry'[22] based on exactly this sample which breaks down the residual detector asymmetry. The corrections included are in Table 2.2. These contribute to a final measurement using vacuum beam events of $\delta_L = 3322 \pm 74$ ppm.

Source of Bias	Bias(ppm)
$\pi^\pm$ difference in CsI	-156 $\pm$ 10
$\pi^\pm$ interaction in trigger scintillator	54 $\pm$ 10
π decay and punchthrough	34 $\pm$ 40
$e^\pm$ difference in CsI	-19 $\pm$ 18
target/absorber $K_S - K_L$ interference	-12 $\pm$ 1
e^+ annihilation in spectrometer	11 $\pm$ 1
δ-ray production	-8.5 $\pm$ 4.3
π absorption in spectrometer	5.0 $\pm$ 3.2
inexact magnet polarity reversal	-3.1 $\pm$ 1.6
final collimator and regenerator scatters	-1.2 $\pm$ 2.3
$K_{\pi 3}, K_{\mu 3}, \Lambda_{p\pi}$ and Λ_β backgrounds	0.5 $\pm$ 0.7
Total Correction	-95.3 $\pm$ 46.5

Table 2.2: Asymmetry Biases in Vacuum Beam Analysis (K_L)

The biases in our regenerator measurement of δ_L are very similar to those in the vacuum beam. The chief differences come from two sources. First, the Z distribution of decays is different since the vacuum analysis uses events upstream of the regenerator edge. Second, slight changes to event selection criteria designed to squeeze the momentum ambiguity and eliminate scattered events alter the pion momentum spectrum. This stands out as the largest bias and since its bias is momentum dependent, it will be critical to carefully recompute the bias in the regenerator sample.

CHAPTER 3

DATA COLLECTION

The KTeV data acquisition system is capable of writing ∼5 Mb/sec of data. With a raw event averaging 8 Kb, the triggering system was designed to select events at the rate of ∼2 kHz to write to tape. The structure of the primary beam results in a 'bucket' of protons every 19 ns during the 20 seconds of active spill every minute. Three levels of trigger logic are used to accomplish this herculean sorting task. The first level trigger runs at 53 MHz and uses the prompt signals from the veto systems and drift chambers, the CsI total energy, and the trigger hodoscopes. After the level 1 selection, the trigger is interrupted while the second level processes operate. These include the Hardware Cluster Counter (HCC) [23], which counts the individual clusters of energy in the calorimeter, the y-track finder and 'hit counting'. A front-end dead time of ∼2 μs allows this hardware to complete its processing and for the trigger logic to reach a decision. Events satisfying the level 2 requirement incur an additional 10 μs dead time as the front-end crates move the information about the detectors state into a centralized data buffer. The third level trigger pulls events from this buffer and performs a full event reconstruction.

During typical running, the global trigger rate is approximately 40 kHz out of level 1, 10 kHz out of level 2, and 2 kHz out of level 3 and onto tape. An overall dead time of 33% is typical.

3.1 Trigger Logic

3.1.1 Level 1 Trigger

For the regenerator K_{e3} sample, the nominal charged mode trigger is required for all events. This trigger combines inputs from the trigger hodoscope, the drift chambers, and the veto systems.

At $Z = 184$ m the trigger hodoscope consists of two planes (V_0 and V_1) of 5 mm thick scintillator paddles, as depicted in Figure 3.1. Each plane has 14 cm square holes in the beam region to allow the neutral beams to pass. The planes are split vertically and the counters are offset horizontally, such that none of the long vertical cracks align. The trigger logic counts hit paddles in each plane, requiring hits to be consistent with two tracks but still allowing a single point inefficiency ($2V_0 \cdot V_1 + V_0 \cdot 2V_1$). Additionally, triggered counters must have representatives from both top and bottom, as well as east (-x) and west (+x). A central overlap region is allowed to count as either east or west for this East-West-Up-Down logic ($EWUD$).

To further reduce the trigger rate, both views of the upstream chambers are instrumented with logic that provides a fast signal for events which have hits. These are referred to as the drift chamber "ORs" (DC-OR). Requiring that 3 of 4 upstream views have DC-OR hits reduces the trigger rate by removing events with decay vertices downstream of chamber 1.

In addition to the hodoscopes and DC-ORs, which signal the presence of good events, requirements are made to eliminate triggers on events that are unacceptable. Requiring the regenerator veto output level to be low eliminates events with hard scatters, showers or decays in the regenerator. This includes the elimination of a majority of the inelastic regeneration background. Activity in the photon veto counters also causes the level 1 trigger to reject an event. Events with final state

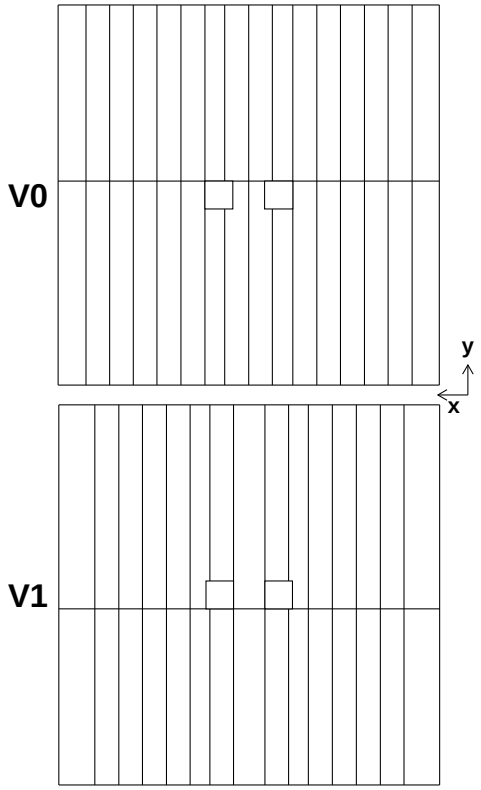

Figure 3.1: Trigger Counter Geometry

particles that escape detection by the drift chambers and calorimeter or that are accompanied by large coincident accidental activity are removed by this requirement. High energy muons, either directly from kaon decay or from subsequent pion decay, will, with high probability, penetrate the steel filters downstream of the CsI and cause the muon hodoscopes to register a hit. The level 1 logic removes events which trigger this counter, eliminating most $K \to \pi\mu\nu$ ($K_{\mu 3}$) events.

3.1.2 Level 2 Trigger

The charged mode level 2 trigger relies on two hardware processors to make more precise decisions about the geometry of hits in the drift chamber. The 'hit counting'

processor reads out the drift chambers and quickly assesses the number of in-time hits. This number must be consistent (allowing for single wire inefficiency) with the presence of at least two tracks in the spectrometer. These in-time hits are passed on to the "Y-track finder" which applies a track shape filter to reject two-track events inconsistent with a common upstream vertex.

3.1.3 Level 3 Trigger

In the Level 3 trigger, a full event reconstruction is done. Reconstructed events are required to have two or more tracks, with at least one matched to a cluster, and a reasonable vertex candidate on the regenerator side of the detector. In the vacuum beam, events with a track with $E/P > 0.9$ are tagged as likely K_{e3} decays and prescaled by a factor of 7. In the regenerator beam, these events have been spared the prescale in order to maximize the data sample for this analysis.

3.2 The 1997 Run

Data from KTeV's 1997 run is used for this analysis. Between April 3 and July 13, 323 high quality data runs were collected (runs 9063 - 10259). The magnet polarity was periodically flipped ($\sim$ twice daily) to help cancel the geometric acceptance bias in our detector. The distribution of events collected to tape by run and the magnetic field polarity for each can be seen in Figure 3.2.

During the 1997 running period, 2.3×10^{17} protons were delivered to target. There were 24×10^9 Level 1 triggers, 12×10^9 Level 2 triggers, and 5×10^8 regenerator tags written to tape. On the order of 4 terabytes of regenerator K_{e3} decays were written to tape.

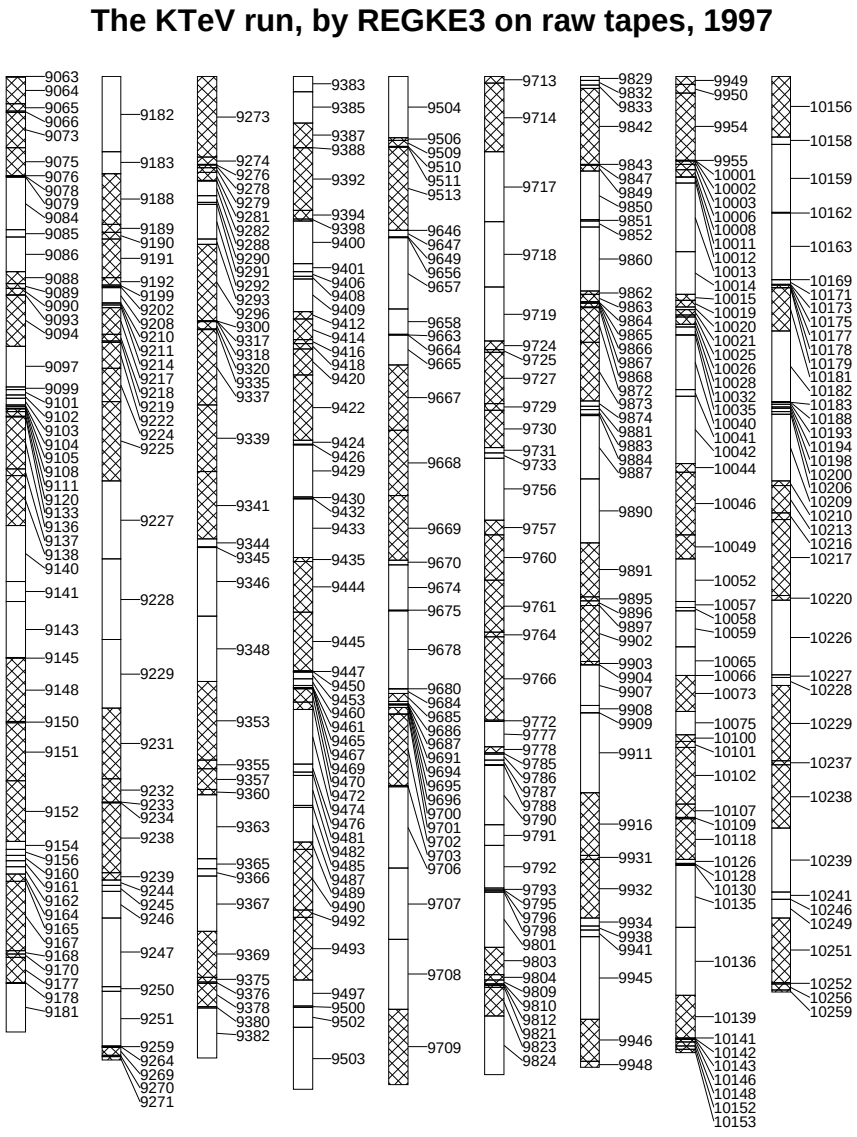

Figure 3.2: Runs used in this analysis. The area of each rectangle is proportional to the number of regenerator K_{e3} events accepted in the final analysis. Shading indicates the magnet polarity.

CHAPTER 4

DATA ANALYSIS

The aim of the final event selection process is to eliminate poorly reconstructed events, eliminate events from non-K_{e3} decays, and minimize events from decays of scattered kaons. Additionally, the analysis addresses the momentum ambiguity due to the missing neutrino. The level of care required for the treatment of scatters and the momentum ambiguity is unique to this analysis. The irreducible background from kaons that scatter in the regenerator is very large and must be known well. Although regenerator scatters are treated carefully in the $K_{\pi 2}$ analysis, in that case the parent p_T^2 is fully reconstructed, resulting in an order of magnitude reduction in the background. The momentum ambiguity has been addressed with varying degrees of sophistication in KTeV measurements of the K_{e3} form factor, the $K_{e3\gamma}$ branching ratio and form factor [24] and the K_L asymmetry, δ_L [22]. However, these efforts, conducted in the vacuum beam, did not simultaneously address a large background issue. One final comment comparing this effort to others within KTeV - the number of regenerator K_{e3} decays written to tape, 500 million, was the second largest event sample in KTeV by only a factor of 2. The larger vacuum K_{e3} set is one of the largest fully reconstructed signal samples in the history of high energy particle physics. This analysis must address three frontiers: regenerator scattering, statistical power, and momentum ambiguity resolution.

This chapter describes the selection criteria and the generation of arrays for use by the fitter.

4.1 Analysis Cuts

Many cuts are applied to the recorded sample in order to leave a population of events that have a high signal to background ratio and are easily modeled.

4.1.1 Event Quality Cuts

The tracking analysis matches upstream track segments to downstream track segments at the bend plane of the magnet. A χ^2 parameter quantifies the quality of the track matching. Similarly, the decay vertex is defined by the closest approach of the upstream segments. A similar χ^2 parameter quantifies the quality of the vertex fit. Loose cuts on these reconstruction parameters guarantee well measured 2 track events. Additionally, we require that the vertex be on the same side (east/west) of the detector as the regenerator. Cuts on activity in the regenerator scintillator eliminate neutron interactions, kaon decays within the regenerator, and the majority of inelastic kaon scatters. These cuts require that:

- Vertex $\chi^2 < 100$
- Offmag $\chi^2 < 500$
- X_{VTX} has the same sign as X_{REG}
- Regenerator Activity < 2 MIPs
- Regenerator Lead Module Activity < 0.7 MIPs

4.1.2 Particle ID Cuts

The standard KTeV analysis matches tracks in X with those in Y by pairing projected tracks with clusters in the calorimeter. Requiring tracks to be separated at

the CsI guarantees that very few mis-matches remain in the final sample. Because the electron shower is contained within the calorimeter, the ratio of its measured energy and momentum is expected to be very near unity. Most of the time the pion showers hadronically or not at all, depositing only a small fraction of its energy in the calorimeter. Our cuts require a high value of E/P for the electron and a low value of E/P for the pion to ensure clean particle identification. The result is a set of good two track events with a high purity of K_{e3} events. These cuts require that:

- Track X Separation at CsI > 3 cm
- Track Y Separation at CsI > 3 cm
- Track R Separation at CsI > 5 cm
- E/P for $\pi < 0.85$
- E/P for electron > 0.94

4.1.3 Fiducial Cuts

To measure direct **CP** violation, the acceptance for $K_{\pi 2}$ events must be understood extremely well. The crucible of the $\Re(\epsilon'/\epsilon)$ analysis forged a set of fiducial cuts which guarantee that only events for which the detector acceptance is well modeled survive. Although modeling the acceptance is not as critical to this analysis, the same fiducial cuts are used to select well measured events with efficient particle identification. These cuts require that:

- Distance from CA edge > 2 mm
- Track is inside DC outer edge
- Distance from CsI outer edge > 2.9 cm

- Distance from VV' hole edge > 1 mm
- Wire centered cell separation > 2 cells

4.1.4 Non K_{e3} Background Cuts

The largest remaining background not due to real K_{e3} decays are the decays of coherently regenerated kaons to $\pi^+\pi^-\pi^0$. A kinematic cut on the longitudinal momentum of the π^0 (so called $P_{\pi^0 KIN}$ [9]) is very effective in removing these events. A small number of scattered kaons that decay to $\pi^+\pi^-\pi^0$ can survive this cut. Cutting on extra clusters in the event greatly reduces this background in addition to eliminating many radiative K_{e3} decays. Regenerator $K_{\pi 2}$ decays are eliminated by assuming both particles are pions and removing events with reconstructed mass near the kaon mass. $K_{\mu 3}$ decays with both particles misidentified are reduced by requiring potential μ tracks to have sufficient momentum to penetrate the μ-filter and fire the veto. These cuts require that:

- If $M_{\pi\pi} < 0.400$ GeV, then $P_{\pi^0 KIN} < 0.0$ GeV
- No extra clusters (> 20 cm from track at the CsI and $E > 1.5$ GeV to qualify)
- 0.4926 GeV $< M_{\pi\pi} < 0.5026$ GeV
- Track momentum > 8 GeV
- Track momentum < 200 GeV

4.1.5 Scattered K_{e3} Background Cuts

The scatters of kaons in the regenerator are very difficult to remove since they have identical final state particles and the rejection power of the P_T^2, so great in the fully

reconstructed modes ($\pi^+\pi^-$, $\pi^+\pi^-\pi^0$), is severely handicapped by the neutrino's unmeasured trajectory. A number of kinematic cuts serve to decrease the number of scattered events in our samples. Requiring that the vertex remains in the beam region removes scatters that escape the profile of the well collimated kaon beams. For coherent events, the kinematic maximum for the transverse momentum of each track, and for the 2 track system is $\sim$0.054 (GeV/c)^2 ($\sim\frac{M_K^2-M_\pi^2}{2M_K}$). Removing events that exceed this limit preferentially rejects scattered events. The most powerful discriminant is the ARGUMENT, ${p^*_{OBS\|}}^2$, defined in Equation 2.6. Imperfect resolution contributes a small, non-physical tail to the negative side of the ARGUMENT distribution, however for scattered events this tail is much larger. Requiring the ARGUMENT to be greater than -0.002 (GeV/c)^2 reduces the scattered background by $\sim$40%. These cuts require that:

- RINGNUMBER < 110 cm^2
- $P_T^2 < 0.054 \left(\frac{\mathrm{GeV}}{c}\right)^2$
- P_T^2 $\pi^\pm < 0.054 \left(\frac{\mathrm{GeV}}{c}\right)^2$
- P_T^2 $e^\pm < 0.054 \left(\frac{\mathrm{GeV}}{c}\right)^2$
- ARGUMENT $> -0.002 \left(\frac{\mathrm{GeV}}{c}\right)^2$

4.2 Input to the Fitter

After applying all of the cuts, 125,425,011 signal events remain. For each combination of magnet polarity, lepton sign, and regenerator position, a histogram is made of the ($\hat{P}$,Z) distibution, with 1 GeV steps from 0 to 200 GeV and 40 cm steps from 110 m to 160 m. These 8 histograms serve as the inputs to the asymmetry calculation. When analyzing the simulated data, the same histograms are made; however,

Source	Sample	Histogram Variables
Data Signal MC Background MC	Signal Sideband	$(\hat{P},Z)$
Data Signal MC Background MC	Sideband	$(P_T^2,\hat{P})$ $(\text{RINGNUMBER},\hat{P})$ $(\text{ARGUMENT},\hat{P})$ $(P_{Te}^2,\hat{P})$ $(P_{T\pi}^2,\hat{P})$
Signal MC Background MC	Signal	$(\hat{P},P,Z)$

Table 4.1: Final Arrays Generated for the Asymmetry Fitter.

an additional set of arrays are generated, recording the distibution of $(P,\hat{P},Z)$ in coarser 5 GeV by 2 m steps. For a background free sample this information would be sufficient for the fitter. However, to address the large background a sideband sample is defined. Any event which passes all of the analysis cuts not associated with the scattered background (Sections 4.1.1-4.1.4), but fails at least 1 of the scattered background cuts, is assigned to the sideband sample. For this sample, 5 additional histograms are formed, 1 for each of the background sensitive variables. Table 4.1 summarizes the analysis output histograms.

CHAPTER 5

THE MONTE CARLO SIMULATION

Section 2.2 described the need for a detailed detector simulation to fulfill two roles. First, it must predict the distribution of proper times observed so that the fitter can accurately extract the parameters of interest from the observed asymmetry. Second, it must predict the distribution of the incoherent decays sufficiently to allow their correct treatment in the fitting process.

To accomplish these tasks the standard KTeV Monte Carlo (MC) simulation has been modified to include a detailed model of incoherent scatters in the regenerator. Section 5.1 will give an overview of the KTeV simulation methodology as implemented in the MC. Section 5.2 follows with a plethora of Data/MC comparisons to demonstrate the strengths and weaknesses of our model. Section 5.3 describes this model of the regenerator and shows the critical data/MC comparisons. Finally, Section 5.4 discusses a quick method for quantifying the impact of non-K_{e3} backgrounds in our sample.

5.1 The Monte Carlo Simulation

The KTeV Monte Carlo simulation is about 100,000 lines of FORTRAN code developed by a truly collaborative effort over many years. The simulation can be broken into parts: kaon production, kaon evolution, kaon decay, decay product evolution,

individual detector response, accidental activity, and trigger response. Each of these steps plays a role in correctly predicting the overall detector acceptance.

The momentum spectrum of kaon production is tuned to agree with the spectrum observed in the $K \to \pi^+\pi^-$data. The parameterization of the ratio of K^0 and $\overline{K^0}$ is based on the production model of Malensek [25]. Simulation of the kaon evolution properly computes the amplitude of evolution as the kaon traverses the absorbers and regenerator. Upstream collimators are treated as perfectly absorbing. Kaon scattering is modeled in the downstream collimators, absorbers and regenerator. The kinematics of the K_{e3} decays generated for this analysis include the full radiative treatment, including $K_{e3\gamma}$ decays.

The decay products are traced through the detector. Multiple scattering, electron Bremsstrahlung, photon pair production, and pion decay are all modeled: any secondary particles are traced through the detector as well. The appropriate momentum kick is applied at the bend plane of the magnet.

The simulation of the drift chambers must convert the position of the passing particle into hit-times on the relevant wires. J. Graham's thesis [7] describes this in detail. The simulation takes place at a low enough level to address four effects that result in inefficiencies or degradation in resolution of the detector.

1. In a small fraction of cases ($\sim$ 1%), the pulse from the wire never crosses above threshold and the Time Delay Counter (TDC) doesn't register a hit. This "wire inefficiency" is addressed by including a detailed wire by wire map of the measured inefficiency. This is coupled with an overall cell position dependence to model the effect.

2. In a fraction of cases, the sum of distances (SOD) from adjacent wires is observed to be more than 1 mm greater than the cell size, resulting in poorer

resolution. This effect is more prominent in the central chamber region exposed to the neutral beams. The simulation addresses this problem by modeling the arrival time of individual drift electrons and computing a simulated pulse shape. The localized wire damage that causes the "high-SOD" problem is then modeled by adjusting the gain of the final cascade to the wire. Thus the effective threshold for triggering the TDCs is adjusted to be consistent with the observed high-SOD rates.

3. Accidentals can result in both "low-SOD" hit pairs when they trigger the TDC before the actual particle passes, and hit losses when they trigger the TDC just prior to the event start time, causing the true pulse be missed due to the discriminator dead-time. Two causes of the discriminator dead-time are modeled: 42 ns after an early accidental is the minimum re-triggering time and hits that should be in this window are missed. Long accidental pulses can cause the re-triggering time to be extended. The distribution of these pulse lengths are tuned in the MC to match the data.

4. Delta rays from the interaction of the charged particle with the chamber window or gas can generate low-SOD events as well. These are included in the MC and then tuned to match the 0.5% level observed in the data.

The simulation of the amount of energy deposited in the calorimeter is described in detail in the thesis of V. Prasad [21]. The simulation is driven by a core library of showers (for both electrons and pions) generated by GEANT. For electrons and photons, the showers cover a 13×13 small block region (extended via a parametrization to 27×27) and are generated in 6 logarithmic energy bins. For pions the coverage must be more extensive, covering a 50×50 array, due to the less uniform nature of hadronic showers. Care is taken to match the observed impact of location de-

pendence within the crystals, leakage across the beam-holes, photo-statistics and calibration of the ADC response.

The simulation also includes the trigger hodoscopes. Details of their geometry have been very carefully mapped out and the resulting 0.3% inefficiency is very well understood. The full Level 1, Level 2, and Level 3 triggers are simulated and the final output of the MC is saved in a format that is completely compatible with the standard KTeV data.

5.2 Monte Carlo Comparisons to Data

For the purposes of generating the migration matrix, 1,127,811 coherent regenerator K_{e3} decays were generated that pass all of the analysis cuts. An additional 142,587 incoherent events were generated separately and also pass all analysis cuts. These represent only $\sim$1% of the data sample but provide an adequate statistical sample for the purposes of this analysis. These coherent and incoherent samples are combined in a weighted fashion based on the parameters in the background fit discussed in Chapter 6, to allow the comparisons with the data which follow.

5.2.1 Quality Variables

Figure 5.1 shows the data/MC overlays for the track quality variables. Note the logarithmic scale and the quite loose cuts in these variables. The regenerator veto cut is the most restrictive, removing 6.5% of otherwise acceptable events. The MC predicts only a 5.8% loss, suggesting an incomplete accounting of K_{e3} events which accompany energy deposit in the regenerator. The systematic effect of this mismatch is investigated further in Section 7.3.1.

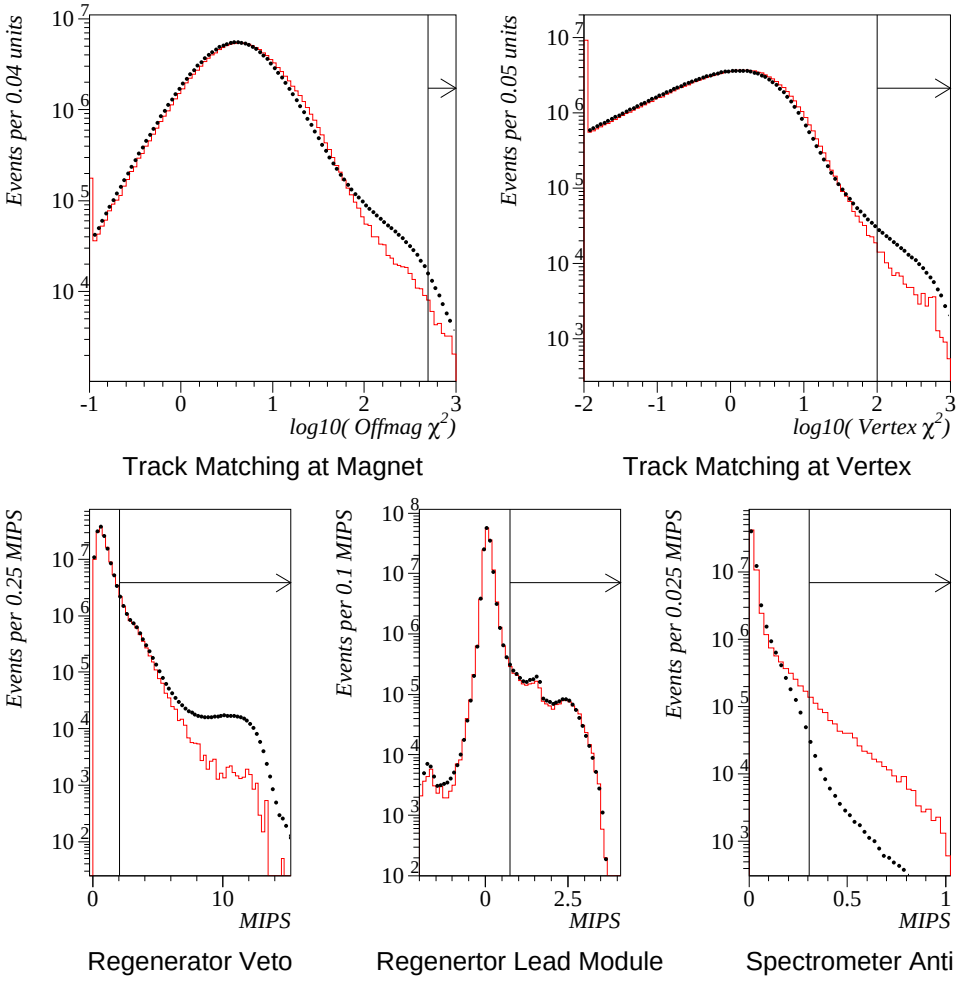

Figure 5.1: Overlay of Data on Monte Carlo of the Quality Variables. Although the agreement on the tails of the χ^2 distributions is poor, this represents very few events. Arrows indicate the events removed by the standard analysis cuts.

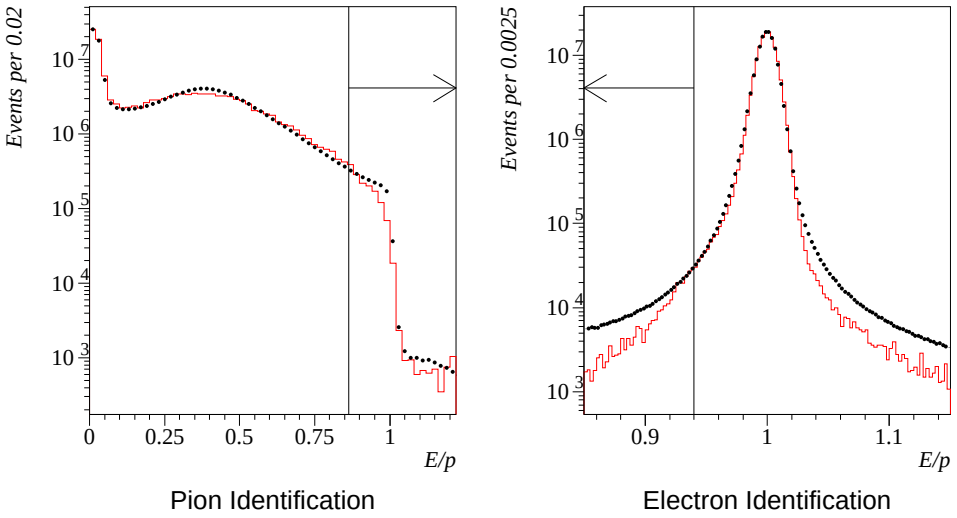

Figure 5.2: Overlay of Data on Monte Carlo for E/P. Arrows indicate the events removed by the standard analysis cuts.

5.2.2 PID Variables

Simulation of the CsI response for the pions and electrons is quite difficult but not extremely critical to this analysis. Figure 5.2 shows the level of success in this endeavor. A small background can be seen in the electron E/P plot. The level of this background (found by fitting a second order polynomial to the sidebands in Figure 5.2) is 3×10^{-4}. This level is consistent with K_L scatters in the regenerator which subsequently decay to charged $K_{\pi 3}$ ($K \to \pi^+\pi^-\pi^0$) and have a pion that passes the electron ID cuts. Section 5.4.1 will show that this has negligible impact on our fits.

Track separation cuts are required in order to guarantee proper track-cluster matching for the E/P measurements. The acceptance of the detector is sensitive

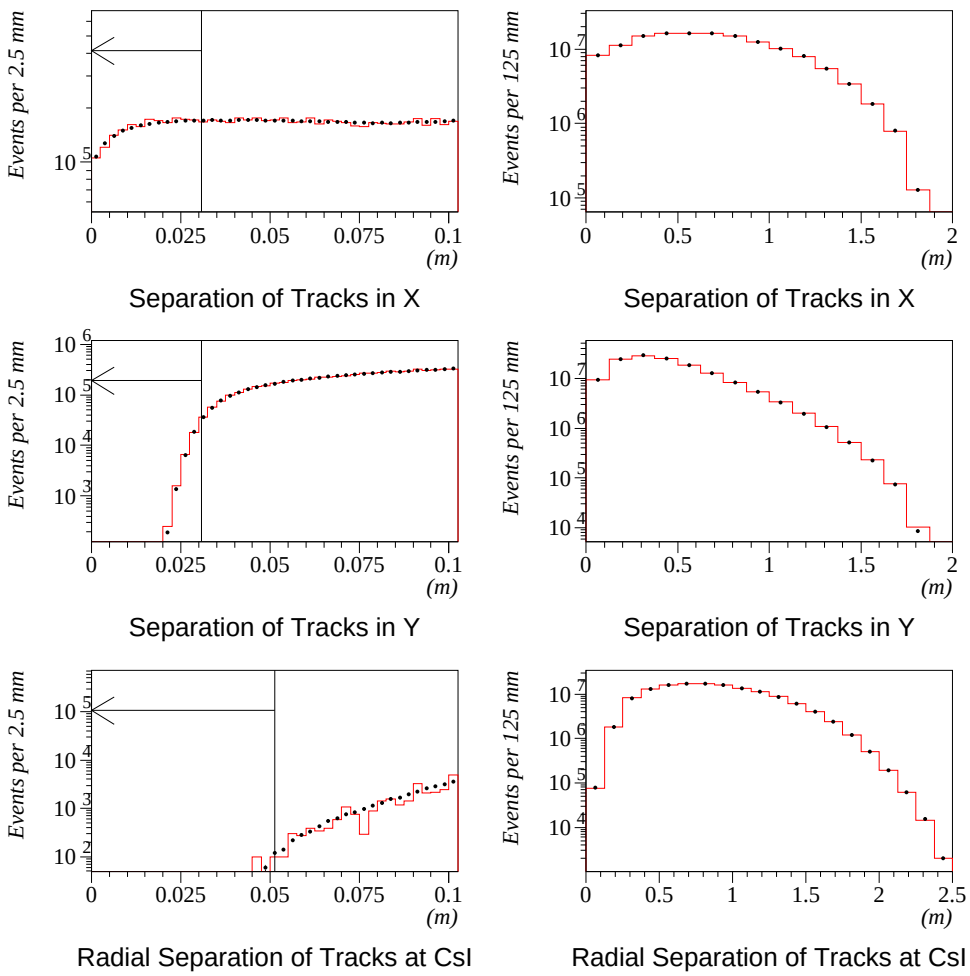

Figure 5.3: Overlay of Data on Monte Carlo for for Track Separation Variables. Plots on the left are the expanded version of the leftmost bin of the plots on the right. Arrows indicate the events removed by the standard analysis cuts.

to these cuts. Figure 5.3 shows good agreement between the data and MC for the track isolation variables.

5.2.3 Fiducial Variables

The cuts which define the geometric aperture for the decay products play a key role in defining the acceptance. Careful study of the electron illuminations near the edges of the CA and the trigger beamholes give very precise knowledge of their location. Figure 5.4 shows the agreement of the fiducial variables. The simulation matches the data very well.

Figure 5.5 shows typical chamber illumination overlays; the discrepancies between data and MC are too small to see on the linear scale. Figure 5.6 shows a typical Data/MC ratio for a pair of these illumination plots. This level of agreement is typical across the volume of the detector.

For the purposes of this analysis, the most probable solution as described in Section 2.2.1 is selected, and the corresponding momentum, $\hat{P}_K$, is used as the observable for the histograms critical to the fitter.

The prediction of the most probable solution does not perform as well for $K_{e3\gamma}$ or scattered K_{e3} decays. The Monte Carlo simulation predicts the migration of the data due to this selection so that the fitter can predict the asymmetry in the observed quantities based on the predicted value in the undistorted quantities. There is no systematic impact on the fit from this momentum picking procedure due to mis-measurement of the matrix element or the flux since they apply the same way to the data and the Monte Carlo. A sub-optimal choice of selection functions will reduce the statistical power. Bias may arise in the asymmetry prediction of the fitter in a way that would be flagged by a failure of the Monte Carlo to match the critical kinematic distributions: $M_{\pi e}$, P_T^2, ARGUMENT, and $P_{T\pi}^2$.

Figure 5.7 shows the dilution effect, as well as the ability of our simulation to predict the distribution of $\log(R_P)$. This procedure results in the correct selection

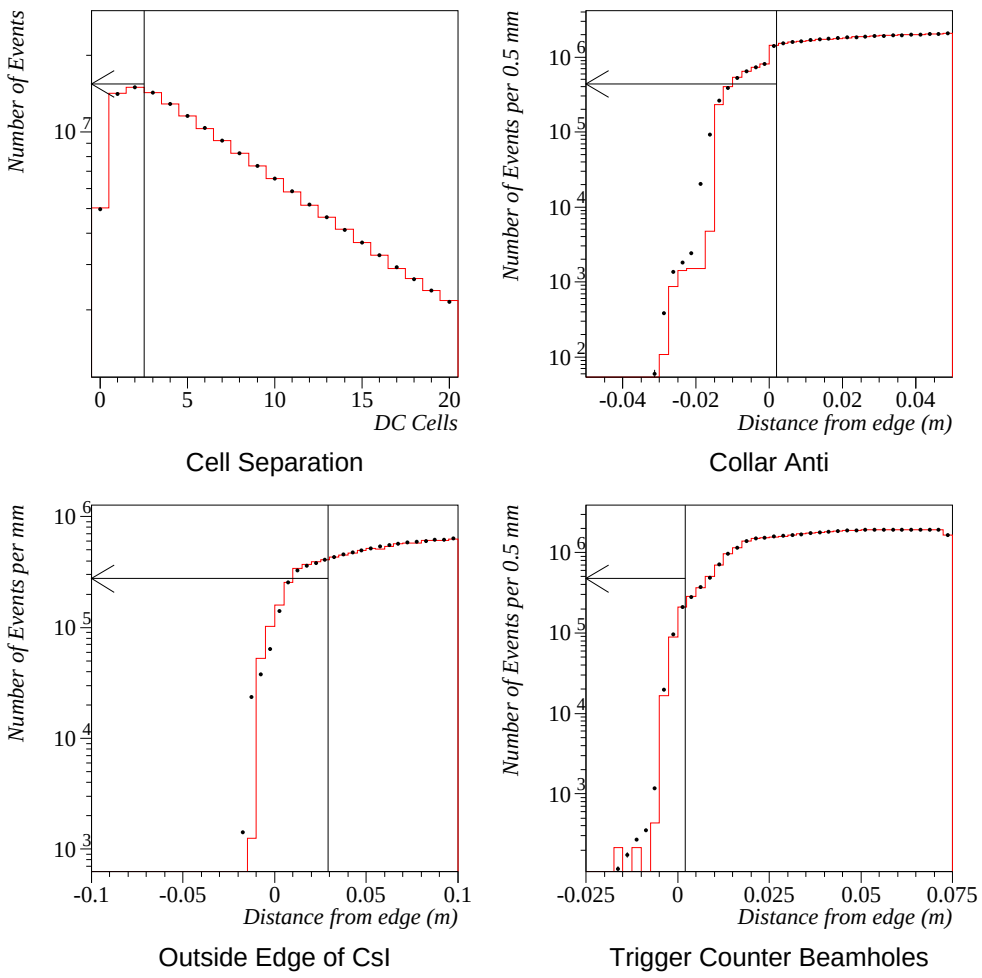

Figure 5.4: Overlay of Data on Monte Carlo for the Fiducial Variables.

65% of the time. There is a statistically significant bias observable as a step in the data/MC ratio. This has the same impact as a mismeasurement of the kaon flux on our fit. Section 7.2.6 addresses this bias.

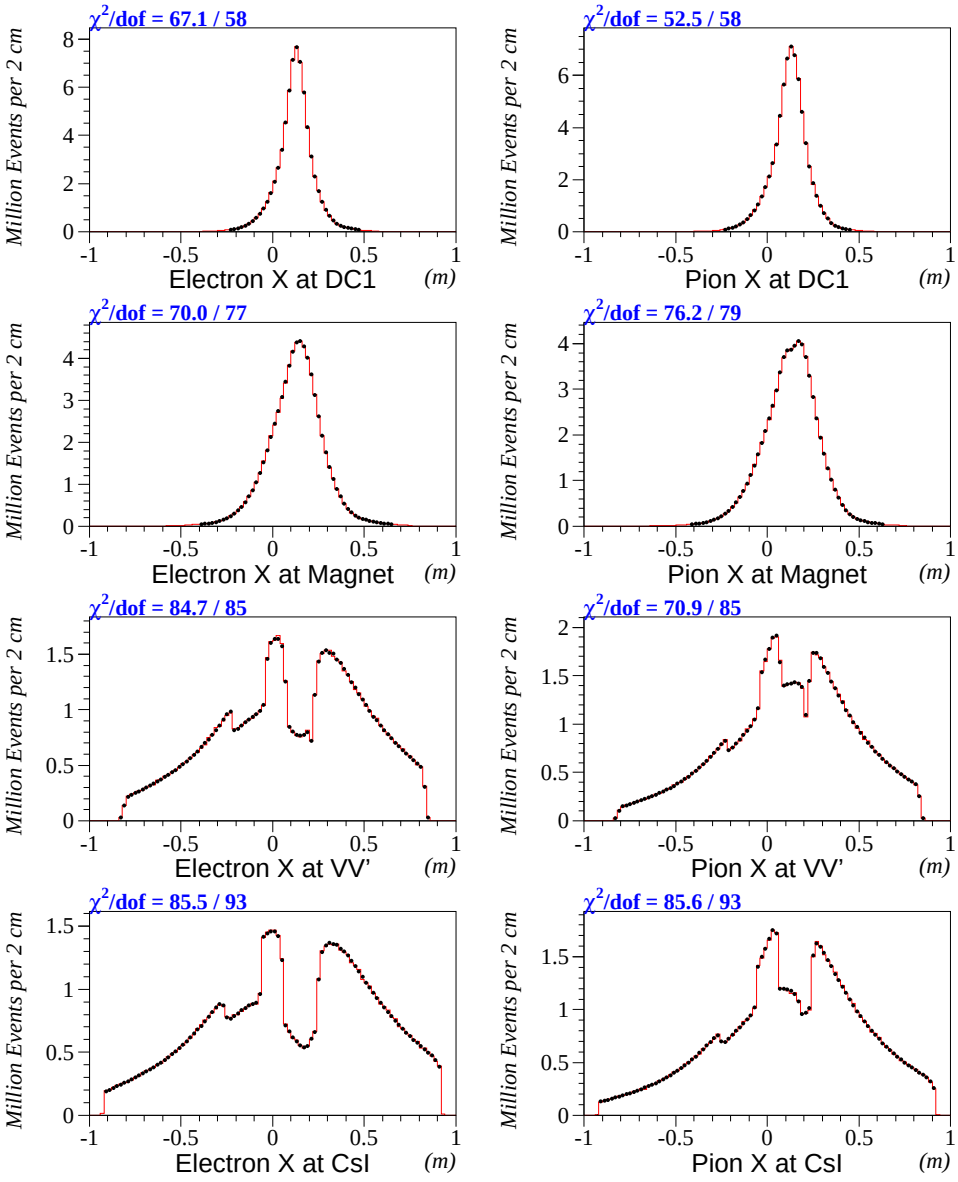

Figure 5.5: Overlay of Data on Monte Carlo for the Illumination. The west beam only is shown in these plots.

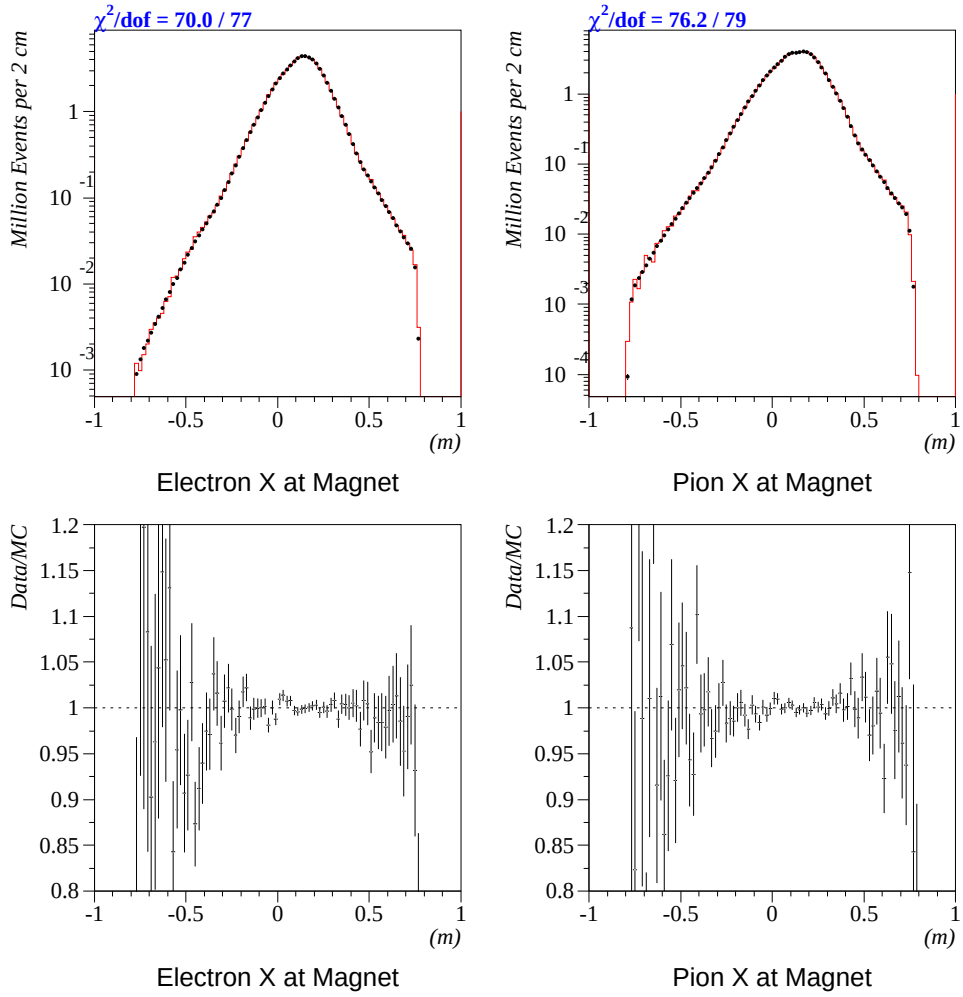

Figure 5.6: Overlay of Data on Monte Carlo for the Illumination at the Magnet Bend Plane. The west beam only is shown in these plots.

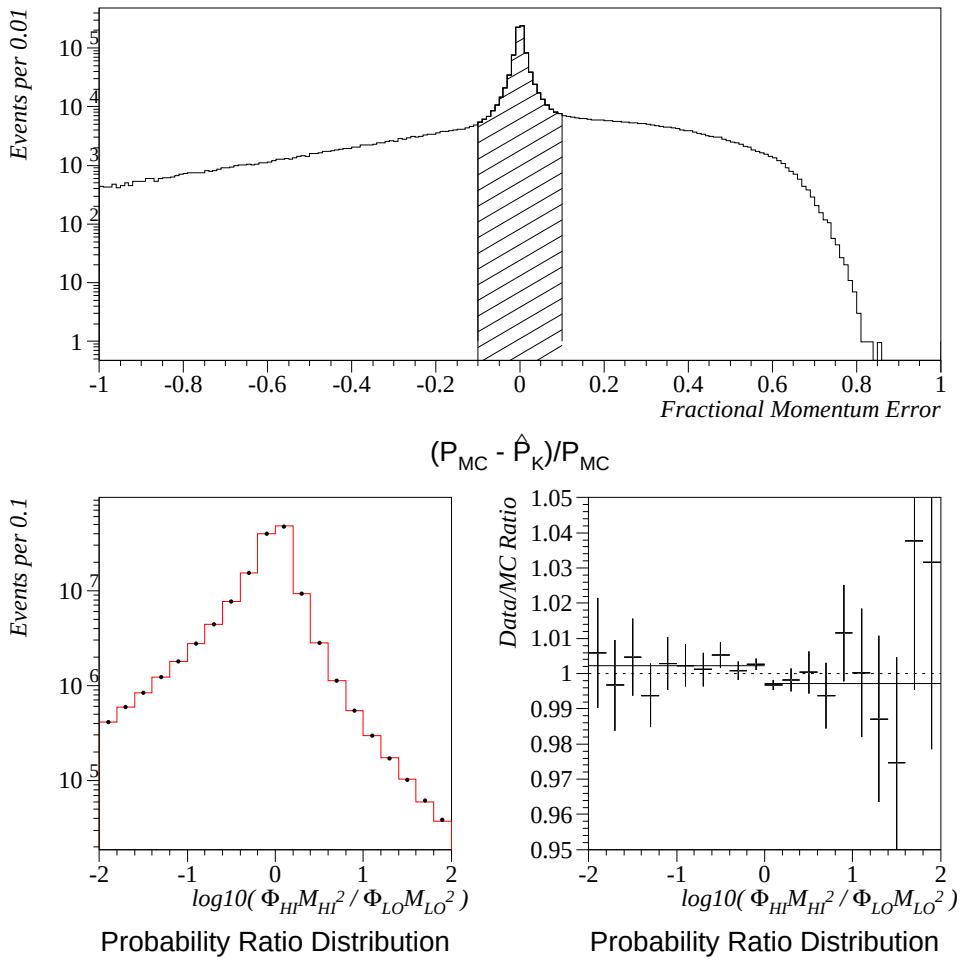

Figure 5.7: a) Error on measured momentum as measured by the Monte Carlo (MC). The width of the peak is the resolution; the 'background' is dilution effect of choosing the wrong solution. 65% of reconstructed MC events are within 10% of the correct momentum solution b,c) Data/MC overlay of the ratio of Hi to Lo momentum weights.

5.3 Simulation of Regenerator Scatters

A simplistic but effective model of diffractive scatters results in the conclusion that the regeneration amplitude for a kaon that undergoes a single elastic nuclear scatter can be written in terms of the coherent regeneration and the length of the regenerator (see Appendix F of [9]):

$$\begin{aligned} |\Psi_{diff}\rangle &\sim |K_L\rangle + \rho_{eff}\,|K_S\rangle \\ \rho_{eff} &= -\left(\frac{2-x}{x}\right)\rho_{coh}\ , \end{aligned} \tag{5.1}$$

where x is the number of interaction lengths in the regenerator.

Kaons that scatter in the regenerator are the dominant background in the neutral mode analysis of $\Re(\epsilon'/\epsilon)$. Consequently, the length of the KTeV regenerator has been optimized to minimize this contaminant. Minimizing ρ_{eff} reduces the background for K_S decays but also has an excellent side-effect for the K_{e3} asymmetry analysis. The phase of the scattered component is almost exactly opposite to that of the coherent component. In the limit that this phase reversal is exact and the coherent and scattered acceptances are the same, the magnitude of the asymmetry is reduced but the phase remains unchanged. Thus, at first order, the impact of this background on the phase measurement is *zero*.

Subtleties like the real part of the nuclear scattering amplitude, decays in the regenerator, multiple scattering, and inelastic regeneration hamper this cancellation. Also simply ignoring the background and allowing the amplitude to float would reduce the statistical power of the fit. Instead, the fitter accounts for incoherent backgrounds by introducing the effective regeneration amplitude, ρ_{eff}, for each of the scattered components. Each component's migration, momentum spectrum, and

Source	$\left\|\frac{\rho_{eff}}{\rho_{coh}}\right\|$	$\phi_{eff} - \phi_{coh}(^\circ)$
Coherent	1.0000	0.00
Single C	0.1393	165.50
Single Pb	0.2300	60.20
Double Scatter	1.2200	172.18
Multiple Scatter	2.3900	175.22
Inelastic Scatter	∞	0.00

Table 5.1: Regenerator Scattering Parameters. An effective ρ of ∞ is shorthand for pure K_S.

kinematics are derived from a modified version of the KTeV Monte Carlo. The modified MC assumes a Regge parameterization of the $K-p$ and $K-n$ amplitudes, integrating these into the carbon and lead nuclear amplitudes using a model that includes both elastic and inelastic screening, and then propagating the kaon state through the regenerator using a full multiple scattering Monte Carlo. The resulting events are tagged by class. Events are tagged as single scatters (carbon and lead considered separately), double scatters (carbon and lead together), inelastic scatters and a catch all multiple scatter (> 2) category. In addition to providing a sample of events the MC computes an effective regeneration amplitude and phase for each component. Table 5.1 shows the values of ρ_{eff}, compared to ρ_{coh}, for each of the scatter types considered. The time dependence of inelastic scatters, typically hard scatters off hydrogen or individual nucleons not vetoed by the regenerator, has been studied with $K_{\pi 2}$ decays and has been found to be very close to that of pure K_S.

Table 5.2 summarizes the background level that remains in the signal region. Using a crude approach to limiting the bias for these background levels is inadequate. Instead, these backgrounds are folded into the fitter where more exhaustive study of their impact is possible.

The most critical test for the regenerator scatter simulation is getting the back-

Source		Events (10^6)	Bkgd.
Data		138.549	.
Elastics		14.219	9.74 %
	1 C	11.358	8.20 %
	1 Pb	1.814	1.31 %
	2 Scat.	0.994	0.72 %
	>2 Scat.	0.053	0.04 %
Inelastics		1.230	0.89 %
Total		15.450	11.15 %

Table 5.2: Regenerator Scatter Statistics in the Signal Region.

ground prediction correct. After normalizing the background components in the sideband of the background variables, Figure 5.8 shows the data/MC overlay of the P_T^2 and RINGNUMBER distributions. There is a clear deficit in the simulation at a RINGNUMBER of 90 to 100 that the systematic error must address. Figure 5.9 shows similar overlays for the ARGUMENT, P_{Te}^2 and $P_{T\pi}^2$ distributions. The ARGUMENT distribution of the signal near 0 is very sensitive to resolution effects. Since the cut is at a value of $-0.002(\mathrm{GeV}/c)^2$, this can result in a large systematic error. For large values of the ARGUMENT the disagreement is due to the same scattered $K_{\pi 3}$ events that affect the electron E/P agreement.

5.4 Non-K_{e3} Backgrounds

To quantify the importance of a given background, it is useful to consider its impact on the charge asymmetry. Consider a signal with N_0 events and an asymmetry of δ_0. Equation 5.2 shows the observed asymmetry after the addition of a background with N_1 events and an asymmetry of δ_1. The error introduced by the contamination is linear in both the size of the background and the *difference* between signal and

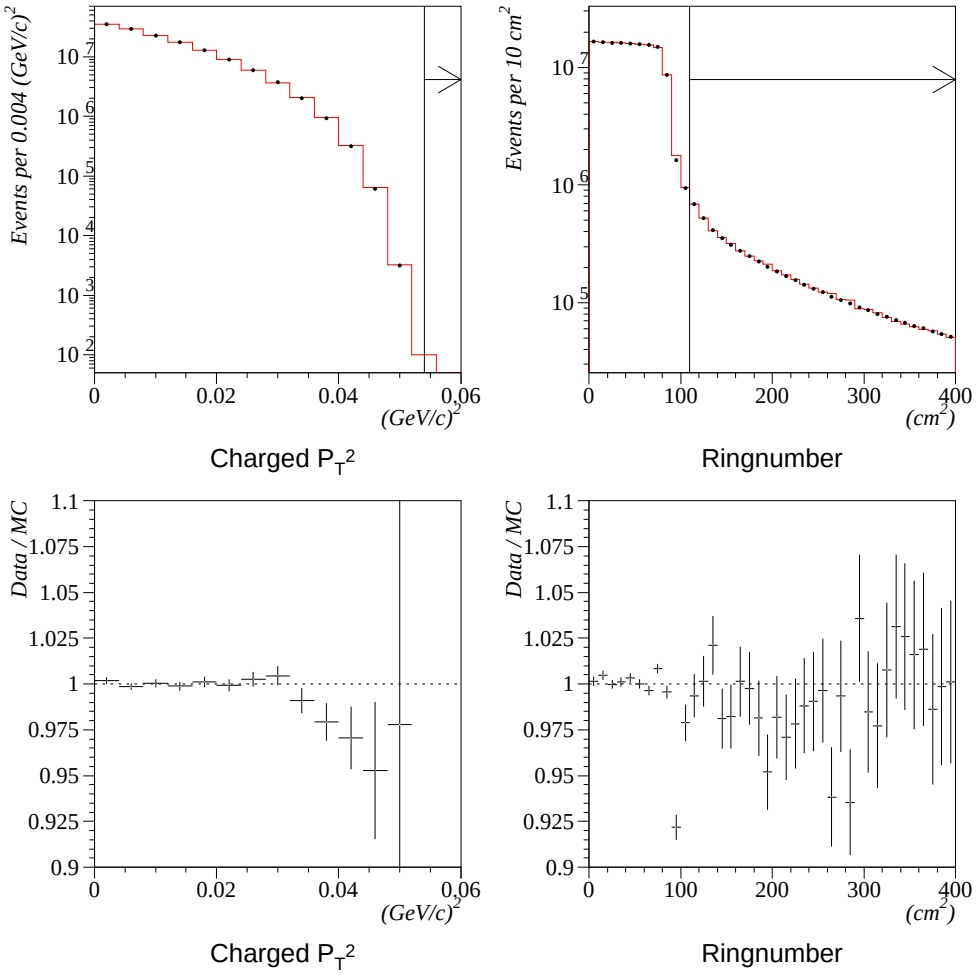

Figure 5.8: Overlay of Data on Monte Carlo for the Observed P_T^2 and RINGNUMBER Distributions.

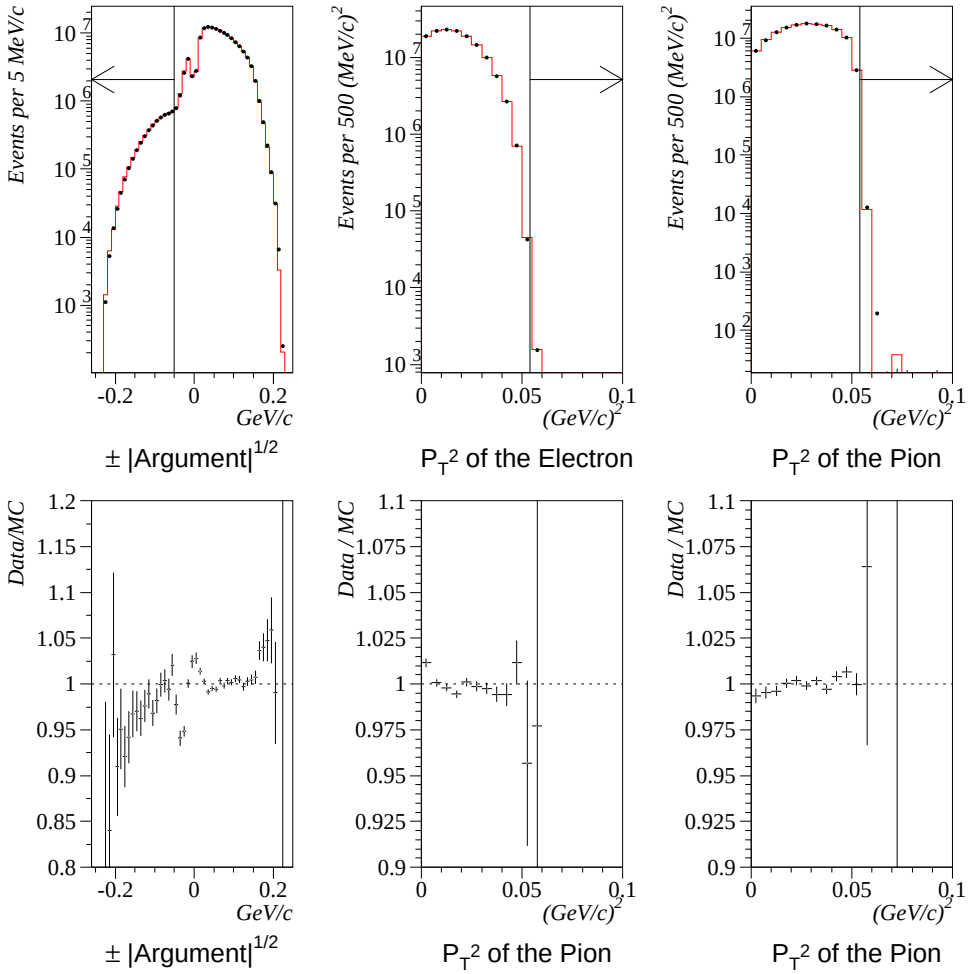

Figure 5.9: Overlay of Data on Monte Carlo for the ARGUMENT, and Track P_T^2 Distributions.

background asymmetries [26]:

$$\delta_{obs} = \delta_0 + (\delta_1 - \delta_0)\frac{N_1}{N_0} \ . \tag{5.2}$$

The relevant metric for this analysis is complicated by the fact that both the absolute level and the proper time dependence of this dilution affect the fit values. For small backgrounds, a naive fit of the data is done by plotting the asymmetry versus τ', the most probable proper time. This histogram is then fit to a function with the form of Equation 1.35. Floating Δm, Γ_S, ϕ_ρ, $|\rho|$ and δ_L results in a good qualitative fit to the data. Clearly the values found will not be accurate; the migration is not included, the momentum dependence of ρ is ignored, etc.. However, by applying the correction of Equation 5.2 and refitting with only ϕ_ρ and δ_L floating, the impact on ϕ_ρ of a background with known $\delta_1(\tau)$ and $N_1(\tau)$ can be estimated.

5.4.1 $K \rightarrow \pi^+\pi^-\pi^0$

The quality of the calorimeter provides extremely good rejection of events without a real electron in the final state. However, in rare cases a photon (or photons) from π^0 decay will deposit sufficient energy in a $\pi^\pm$ cluster to cause the track to be misidentified as an electron.

Table 5.3 shows that the low level of the 3 body decay that remains in the sample is largely removed by a simple kinematic cut (the cut against extra clusters has already been applied). This level has been estimated by normalizing a $K_{\pi 3}$ Monte Carlo with no cut on electron E/P in the region removed by the $P_{\pi^0 KIN}$ cut. Figure 5.10 shows the region removed by our background cut as well as the normalized $K_{\pi 3}$ background projected onto the $P_{\pi^0 KIN}$ axis and the background that remains. The resulting phase bias is $0.036(11)^\circ$.

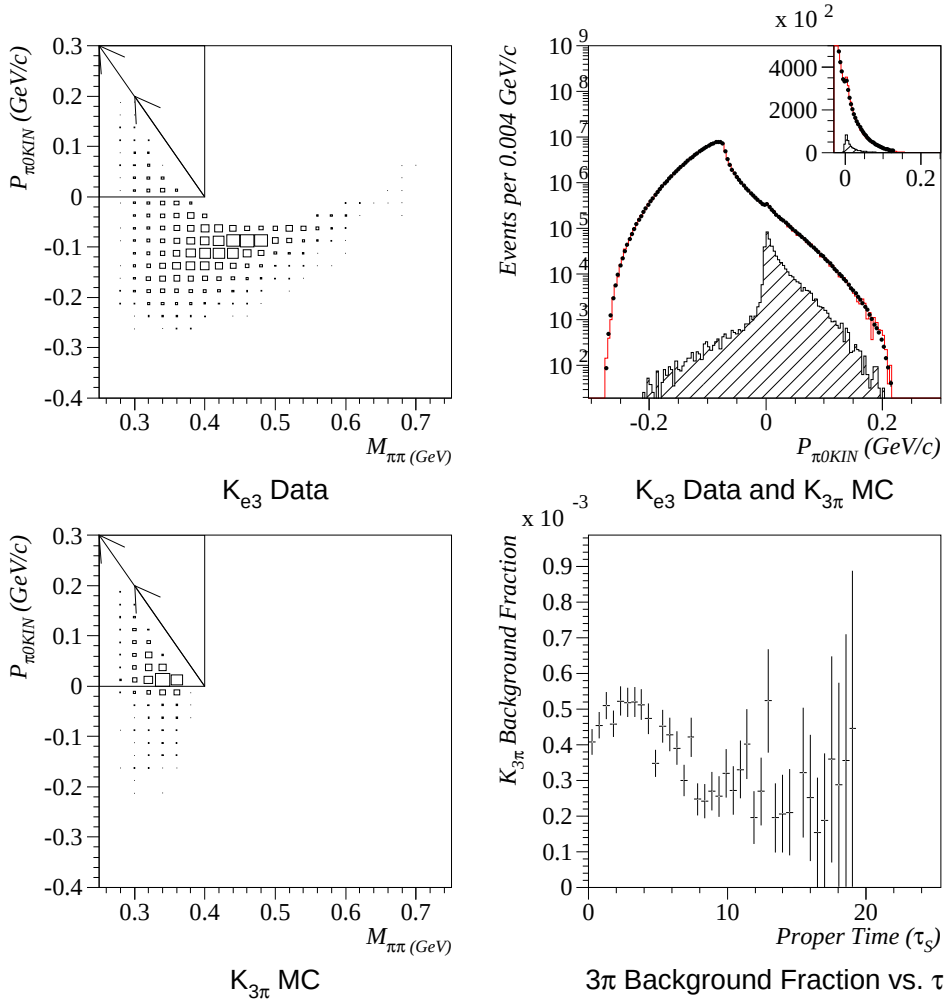

Figure 5.10: The 3π Background. The top-left figure shows the distribution of the observed data in $P_{\pi^0 KIN}$ and $M_{\pi\pi}$. The box in the upper left is removed by the background cuts. The lower-left shows the same distribution for simulated $K_{\pi 3}$ events. The upper-right plot shows the remaining contamination on a logarithmic scale, with an inset on a linear scale. The bottom-right plot shows the background level as a function of observed proper time.

Initial Background	0.30 %
Coherent K_{e3} MC Loss	1.70 %
Scattered K_{e3} MC Loss	3.38 %
Data Loss	2.17 %
Background Rejection	86.%
Remaining Background	0.05 %

Table 5.3: $K \to \pi^+\pi^-\pi^0$ Background Rejection.

5.4.2 $K \to \pi^{\pm}\mu^{\mp}\nu$

In order for a $K_{\mu 3}$ decay to pass the final cuts, one track must fake an electron and the muon must fail to fire the veto counters. This happens most frequently when a low momentum muon ranges out in the filter steel while an accidental track satisfies the electron requirements.

The KTeV Monte Carlo with accidental events overlayed predicts a $K_{\mu 3}$ background acceptance of $(2.0 \pm 1.4) \times 10^{-6}$. Comparing this to a K_{e3} acceptance of 8.36% and using

$$\frac{BR(K_{\mu 3})}{BR(K_{e3})} = 70.1\% \tag{5.3}$$

produces a prediction of the relative background level of

$$\frac{N_1}{N_0} = (17 \pm 12) \times 10^{-6} \; . \tag{5.4}$$

The time dependence of this is similar to that of K_{e3} decays. Deviations due to the misreconstructed momentum, which change the time dependence, have been considered and are small. Even allowing the worst case for the asymmetry of the background, namely 90° out of phase with the signal, only biases the phase by 0.03°.

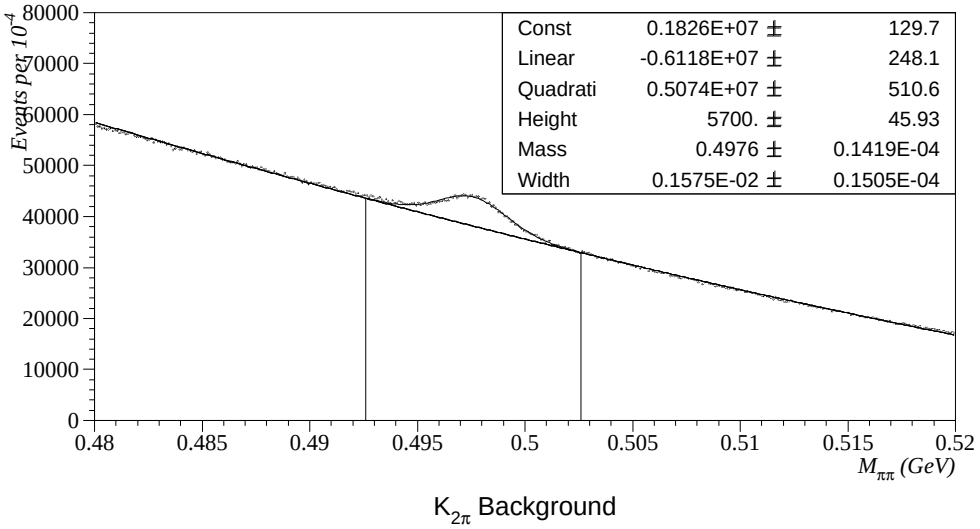

Figure 5.11: The $K_{\pi 2}$ background fit to a Gaussian. A second order polynomial approximates the K_{e3} shape. The total number of $K_{\pi 2}$ events is $225,000$.

5.4.3 $K \to \pi^+\pi^-$

Although Table 5.4 shows that the $K_{\pi 2}$ background is quite small, there is no reason not to remove a background that is so cleanly isolated. Figure 5.11 shows the clear enhancement in the 2π invariant mass distribution in the region of the kaon mass. Failure to make this cut biases the phase by $-0.09^\circ \pm 0.03^\circ$.

Initial Background	0.16 %
Coherent K_{e3} MC Loss	2.87 %
Scattered K_{e3} MC Loss	1.96 %
Data Loss	2.96 %
Background Rejection	∼100.00 %
Remaining Background	0.00 %

Table 5.4: $K \to \pi^+\pi^-$ Background Rejection.

CHAPTER 6

FITTING

This chapter provides a detailed account of the fitting strategy. A discussion of fitting gives needed perspective on the systematic impact of the various effects analyzed in Chapter 7.

6.1 Fitting

The function of the fitter is to take a set of inputs, which include the physics parameters of interest and a set of parameters that describe the background, and to generate a prediction of the asymmetry that can be quantitatively compared to the data. The presence of a large irreducible background from regenerator scatters, and the effects of the dilution of the momentum spectrum by the ambiguity due to the unmeasured neutrino, must be included in the predictions. I consider first the technique for fitting the coherent part. Modifications needed to address the scattered background will follow, along with the exact parameterization used for the background and the method for extracting the value of the background parameters from the data.

6.1.1 Fitting the Coherent Asymmetry

The Physics

The principal physics parameters included in the analyticity fit are:

$$\phi_{f-\bar{f}}\big|_{P_K=70\text{ GeV}},\ \left|\frac{f-\bar{f}}{k}\right|_{k=70\text{ GeV}},\alpha,\ \Delta m,\ \Gamma_S,\ \text{and}\ \delta_L.$$

The first three of these are combined with our best understanding of nuclear screening effects to produce $|f_-(P_K)|$ and $\phi_{f_-}(P_K)$. Together with Δm, Γ_S and measurements of the regenerative behavior of minority components of the KTeV regenerator (hydrogen and lead), these parameters are used to propagate the kaon state from the target to the downstream end of the regenerator resulting in a prediction for ρ. The rate for each lepton charge state is then determined by integrating Equation 1.23 over each Z bin for a fixed value of P. Combining the results for the two charged states yields a predicted asymmetry in each bin, $\delta(P, Z)$.

For ϕ_ρ measurements the $\Delta S = \Delta Q$ violating parameter, x, is fixed to zero. To measure $\Re(x)$ it is then floated in a separate set of fits where ϕ_ρ is fixed to the value predicted by analyticity.

The Migration

The undetected neutrino results in an imperfect reconstruction of the parent kaon momentum. To address this issue the analysis computes an observable, the "most probable momentum" or $\hat{P}_K$ as defined in Section 2.2.1 (henceforth $\hat{P}$). In order to produce a prediction of the asymmetry in a given bin of the observables, $(\hat{P}, Z)$, we compute the appropriately weighted average of the theoretical asymmetry for the mix of real momenta, P, present in each $\hat{P}$ bin as predicted by the MC.

Written in discrete form, the predicted asymmetry in a bin is:

$$\delta(\hat{P}_j; Z_k) \;=\; \frac{\sum_{i=i_{min}}^{i_{max}} M(P_i, \hat{P}_j; Z_k)\delta(P_i; Z_k)}{\sum_{i=i_{min}}^{i_{max}} M(P_i, \hat{P}_j; Z_k)}. \tag{6.1}$$

The M in Equation 6.1 is the MC generated migration matrix. This 3-dimensional array parameterizes the small effect of momentum resolution and the large smearing in the process of computing $\hat{P}$ from the observed particle's trajectories and momenta. Note that resolution effects in the momentum measurement are effectively included in this migration matrix but resolution in Z is not. Systematic effects of Z resolution will be shown to be small.

Acceptance Cancellation

Our data are the numbers of accepted events, $N_i(\hat{P}_j; Z_k)$, in each of 8 subsamples, i. These subsamples will be labeled by subscripts in the succeeding to indicate the magnet polarity, $\uparrow$ / $\downarrow$; the charge of the lepton, $+/-$; and the regenerator position, E/W, i.e., $i \in \{\uparrow +E, \uparrow -E, \downarrow +E, \downarrow -E, \uparrow +W, \uparrow -W, \downarrow +W, \downarrow -W\}$.

In order to compare $\delta(\hat{P}_j; Z_k)$ to the events measured in our data, we will lean heavily on the acceptance cancelation described in Section 2.3. The asymmetries due to the geometry effects in our detector are removed to first order by alternating the polarity of the magnetic field. In that ideal case, the ratio of Equation 2.16 allows the complete cancellation of detector acceptance.

To numerically address the non canceling parts of the acceptance I define the real world acceptance, A:

$$A_{\downarrow +} \;=\; \mathcal{G}_{\leftarrow} \cdot (1 + \Delta\mathcal{G}_{\leftarrow}) \cdot \varepsilon_{e\leftarrow} \cdot (1 + \Delta\varepsilon_{e\leftarrow}) \cdot \varepsilon_{\pi\leftarrow} \cdot (1 + \Delta\varepsilon_{\pi\leftarrow}) \;,$$

$$
\begin{aligned}
A_{\downarrow -} &= \mathcal{G}_{\rightarrow} \cdot (1 - \Delta\mathcal{G}_{\rightarrow}) \cdot \varepsilon_{e\rightarrow} \cdot (1 - \Delta\varepsilon_{e\rightarrow}) \cdot \varepsilon_{\pi\rightarrow} \cdot (1 - \Delta\varepsilon_{\pi\rightarrow}) \ , \\
A_{\uparrow +} &= \mathcal{G}_{\rightarrow} \cdot (1 + \Delta\mathcal{G}_{\rightarrow}) \cdot \varepsilon_{e\rightarrow} \cdot (1 + \Delta\varepsilon_{e\rightarrow}) \cdot \varepsilon_{\pi\rightarrow} \cdot (1 + \Delta\varepsilon_{\pi\rightarrow}) \ , \text{ and} \\
A_{\uparrow -} &= \mathcal{G}_{\leftarrow} \cdot (1 - \Delta\mathcal{G}_{\leftarrow}) \cdot \varepsilon_{e\leftarrow} \cdot (1 - \Delta\varepsilon_{e\leftarrow}) \cdot \varepsilon_{\pi\leftarrow} \cdot (1 - \Delta\varepsilon_{\pi\leftarrow}) \ . \qquad (6.2)
\end{aligned}
$$

The newly introduced variables are $\mathcal{G}$, the canceling part of the geometric and time dependent acceptance; $\Delta\mathcal{G}$, the part that does not cancel; $\varepsilon_{e/\pi}$, the canceling part of the electron/pion efficiencies and $\Delta\varepsilon_{e/\pi}$, the non-canceling part of the electron/pion efficiencies. Equation 6.3 shows the more realistic result for R^2 in the good approximation that these Δ's are significantly less than 1:

$$
\begin{aligned}
R^2 &= \left(\frac{1+\delta'}{1-\delta'}\right)^2 \qquad (6.3) \\
\delta' &= \delta + \frac{1}{2}\left(\Delta\mathcal{G}_{\rightarrow} + \Delta\mathcal{G}_{\leftarrow} + \Delta\varepsilon_{e_{\rightarrow}} + \Delta\varepsilon_{e_{\leftarrow}} + \Delta\varepsilon_{\pi\rightarrow} + \Delta\varepsilon_{\pi\leftarrow}\right) \ . \qquad (6.4)
\end{aligned}
$$

The problem of quantifying the Δ's remains and will be discussed as part of the systematic error. For now, however, I will neglect these small corrections and focus on how best to compare the predicted asymmetry to that observed in the data.

The Likelihood

In order to compare the predicted asymmetry to the data collected in each bin, a likelihood is computed for the agreement of the data with the model represented by:

$$
\begin{aligned}
N_{\downarrow -} &= N \cdot F \cdot R \cdot D \ , \\
N_{\uparrow -} &= N \cdot A \cdot R \cdot D \ , \\
N_{\downarrow +} &= N \cdot F \cdot A \cdot D \ , \text{ and} \\
N_{\uparrow +} &= N \cdot D \ . \qquad (6.5)
\end{aligned}
$$

A comparison to Equation 2.14 shows that the new parameters have the following definitions:

$$\begin{aligned} R &= \frac{1-\delta}{1+\delta}\ , \\ D &= \frac{1+\delta}{4}\ , \\ F &= \frac{\Phi_{\downarrow}}{\Phi_{\uparrow}}\ , \text{ and} \\ A &= \frac{A_{\rightarrow}}{A_{\leftarrow}}\ . \end{aligned} \tag{6.6}$$

For each beam and $(\hat{P}, Z)$ bin there are four data points, ($N_{\uparrow+}$,$N_{\downarrow+}$,$N_{\uparrow-}$ and $N_{\downarrow-}$) and only three free variables (N, F and A). The negative log(Likelihood) can be written down and minimized,

$$\begin{aligned} -\log(\mathcal{L}) &= N_{\Sigma}\log(ND) + N_{\downarrow}\log(F) + \\ &\quad N_{\rightarrow}\log(A) + N_{-}\log(R) - N\ . \end{aligned} \tag{6.7}$$

Equation 6.7 introduces new variables to represent various data combinations:

$$\begin{aligned} N_{\Sigma} &= N_{\downarrow-} + N_{\uparrow-} + N_{\downarrow+} + N_{\uparrow+} \\ N_{\downarrow} &= N_{\downarrow-} + N_{\downarrow+}\ , \\ N_{\rightarrow} &= N_{\uparrow-} + N_{\downarrow+}\ , \\ N_{\leftarrow} &= N_{\uparrow+} + N_{\downarrow-}\ , \text{ and} \\ N_{-} &= N_{\downarrow-} + N_{\uparrow-}\ . \end{aligned} \tag{6.8}$$

The strategy used by the fitter is to maximize the likelihood by allowing F, N and A to float in each bin, and δ (thus the derived R and D) to be predicted by the

physical model. This is quite straight forward. The maximum possible $\log \mathcal{L}$ occurs for the values in Equations 6.9:

$$\begin{aligned} N_0 &= N_\Sigma \, , \\ D_0 &= \frac{N_{\uparrow +}}{N_\Sigma} \, , \\ F_0 &= \sqrt{\frac{N_{\downarrow -} \cdot N_{\downarrow +}}{N_{\uparrow -} \cdot N_{\uparrow +}}} \, , \\ A_0 &= \sqrt{\frac{N_{\downarrow +} \cdot N_{\uparrow -}}{N_{\downarrow -} \cdot N_{\uparrow +}}} \, , \text{ and} \\ R_0 &= \sqrt{\frac{N_{\downarrow -} \cdot N_{\uparrow -}}{N_{\downarrow +} \cdot N_{\uparrow +}}} \, . \end{aligned} \tag{6.9}$$

When compared to the actual $\log \mathcal{L}$ for the fit, with R and D derived from the prediction, this can be converted to a χ^2 in the conventional way,

$$\chi^2 = 2 \cdot (\log \mathcal{L}_{MAX} - \log \mathcal{L}_{PRE}) \, . \tag{6.10}$$

The total χ^2 is the sum of this statistic over each bin in Z and $\hat{P}$. The parameters of the fit are varied in order to minimize this value. The likelihood method *does not* give different results from a simple χ^2 calculation. However, systematic checks in which the flux ratio, F, is fixed within each beam are robustly defined by a simple extension of this procedure. Although it is not relevant for this analysis, this method is also insensitive to potential biases which result from low statistics bins.

6.1.2 Including the Background

Unfortunately there is a large irreducible background of kaons that scatter in the regenerator. Subtracting background from the data before the arrays are passed to the fitter would necessitate the generation of large MC samples and place at a premium

the simulation's modeling of the detector asymmetry. Instead the background is included in the fitting procedure. MC for each background source produces migration arrays analogous to the coherent arrays. An expression similar to Equation 6.1 is formed for each source, and the average of these, weighted by the number of events from each source is used for the prediction.

$$\delta(\hat{P}_j; Z_k) = \frac{\sum_{m=1}^{N_S} \delta_m(\hat{P}_j; Z_k) N_m(\hat{P}_j; Z_k)}{\sum_{m=1}^{N_S} N_m(\hat{P}_j; Z_k)}, \tag{6.11}$$

$$\delta_m(\hat{P}_j; Z_k) = \frac{\sum_{i=i_{min}}^{i_{max}} M_m(P_i, \hat{P}_j; Z_k) \delta_m(P_i; Z_k)}{\sum_{i=i_{min}}^{i_{max}} M_m(P_i, \hat{P}_j; Z_k)}. \tag{6.12}$$

The scattered background has been separated into five sources: single scatters off of carbon, single scatters off of lead, double scatters, multiple (> 2) scatters, and inelastic scatters. These are all added together with the coherent piece to generate the final prediction.

Each $\delta_m(P_i; Z_k)$ is computed using effective values for ρ_m and α_m taken from a detailed model of scattering in the regenerator (Section 5.3). The N_m arrays are taken from a MC which is scaled to correctly predict the sidebands in the P_T^2, ARGUMENT and RINGNUMBER distributions as described in Section 6.1.3.

6.1.3 Fitting the Background

In order to normalize the scattered background to the regenerator K_{e3} data, five distributions are considered: Signal $(\hat{P}, Z)$, Sideband $\hat{P}$, Sideband P_T^2, Sideband

ARGUMENT, and Sideband RINGNUMBER. Detailed descriptions of these variables are provided in the description of the analysis (Section 2.2.2).

The fitter allows a scale and a slope in observed momentum to modify the scattered background predicted by the MC. To make a prediction of the overall background, the fitter scales the scattered MC as defined in Equations 6.13 and 6.14. The new parameters added include an overall normalization to the total flux in each beam, $N_{E/W}$; a separate normalization for elastic and inelastic scatters, $N_{ela/ine}$; a momentum slope for the coherent MC, m_{coh}; and a momentum slope for the scattered background, m_{scat}. Note that the $\hat{P}$ slopes are introduced in such a way that they transform not only the distributions manifestly dependent on $\hat{P}$, the first two, but also the other distributions as well.

$$\begin{aligned} N_{Fit}(\hat{P}) &= N_{E/W} \cdot (1 + m_{coh}(\hat{P} - 61.3)) \cdot \\ &\quad \Big(\mathbf{MC}_{coh}(\hat{P}) + \\ &\quad\quad (N_{ela}\mathbf{MC}_{ela}(\hat{P}) + \\ &\quad\quad\ N_{ine}\mathbf{MC}_{ine}(\hat{P})\ ) \cdot \\ &\quad\quad (1 + m_{scat}(\hat{P} - 61.3)\ )\ \Big) \qquad (6.13) \\ N_{Fit}(X) &= N_{E/W} \cdot \sum_{i}^{j} \Big\{(1 + m_{coh}(P'_i - 61.3)) \cdot \\ &\quad \Big(\mathbf{MC}_{coh}(\hat{P}, X) + \\ &\quad\quad (1 + m_{scat}(\hat{P} - 61.3))\ \cdot \\ &\quad\quad (N_{ela}\mathbf{MC}_{ela}(\hat{P}, X) + \\ &\quad\quad\ N_{ine}\mathbf{MC}_{ine}(\hat{P}, X)\ )\ \Big)\ \Big\} \qquad (6.14) \end{aligned}$$

These parameters are allowed to float in the background fit. The fitter forms

a χ^2 by comparing resulting sideband distributions of $\hat{P}$, ARGUMENT, P_T^2, and RINGNUMBER and the signal region $(\hat{P}, Z)$ distribution with the same distributions in the data. In addition, the P_T^2 slopes for single carbon and inelastic scatters are adjusted by reweighting events in the MC analysis. The resulting χ^2 is minimized with respect to these variables as well.

6.2 Fit Results

6.2.1 Background

Table 6.1 shows the values of the parameters in Equations 6.13 and 6.14 after a fit to the background distributions. Figure 6.1 shows $\hat{P}$ and Z overlays for the signal region. Figures 6.2 and 6.3 show the fitter optimized sideband distributions.

Variable	Value
N_{EAST}	98.43±0.12
N_{WEST}	99.07±0.12
$m_{coh} \times 10^4$ GeV	-2.43±0.23
$C_{ela} \times 10^2$	53.92±0.12
$C_{ine} \times 10^2$	78.30±0.70
$m_{scat} \times 10^2$ GeV	-18.75±0.45
χ^2/ D.o.F.	$867.58/(1178-6)$

Table 6.1: Parameters of Background Fit.

The errors shown in Figure 6.1 are statistical only and represent a fit to the background sideband region defined by:

$$\begin{aligned} P_T^2 &\in [0, 0.2] \left(\frac{\text{GeV}}{c}\right)^2 \\ P_T^2 \text{ electron} &\in [0, 0.2] \left(\frac{\text{GeV}}{c}\right)^2 \\ P_T^2\ \pi &\in [0, 0.2] \left(\frac{\text{GeV}}{c}\right)^2 \end{aligned}$$

$$\begin{aligned} \text{ARGUMENT} &\in [-0.1, 0.04] \left(\frac{\text{GeV}}{c}\right)^2 \\ \text{RINGNUMBER} &\in [0, 400] \text{ cm}^2. \end{aligned} \tag{6.15}$$

These values are quite robust but do show some non-statistical fluctuation when analysis cuts and fit regions are varied. The systematic error due to the uncertainty in these values is based not on their statistical precision but on the wider variation seen in the course of studying the background. In particular, the momentum dependence of the MC background, m_{scat}, varies by as much as 10%/100 GeV.

6.2.2 Asymmetry Fits

Our goal is to extract three measurements from the regenerator K_{e3} asymmetry. The first parameter represents a test of analyticity,

$$\Delta\phi_\rho = \phi_\rho - (-90^\circ(1.0 + \alpha)) \ . \tag{6.16}$$

The second parameter contributes to the precision understanding of indirect **CP** violation, δ_L. The third parameter measures $\Delta S = \Delta Q$ violation, $\Re(x)$.

A large number of fits with various combinations of parameters floating, fixed or constrained have been studied to understand the sensitivity of the fit to deviations in the input parameters. Unless otherwise noted, the fits that follow use the $K_{\pi 2}$ values of the kaon evolution and regeneration parameters, shown in Table 6.2, as fixed constraints. The fiducial range of $\hat{P} \in [30 \text{ GeV}, 180 \text{ GeV}]$ and $Z \in [124 \text{ m}, 154 \text{ m}]$ is considered with 5 GeV bins in momentum and 2 m bins in Z vertex.

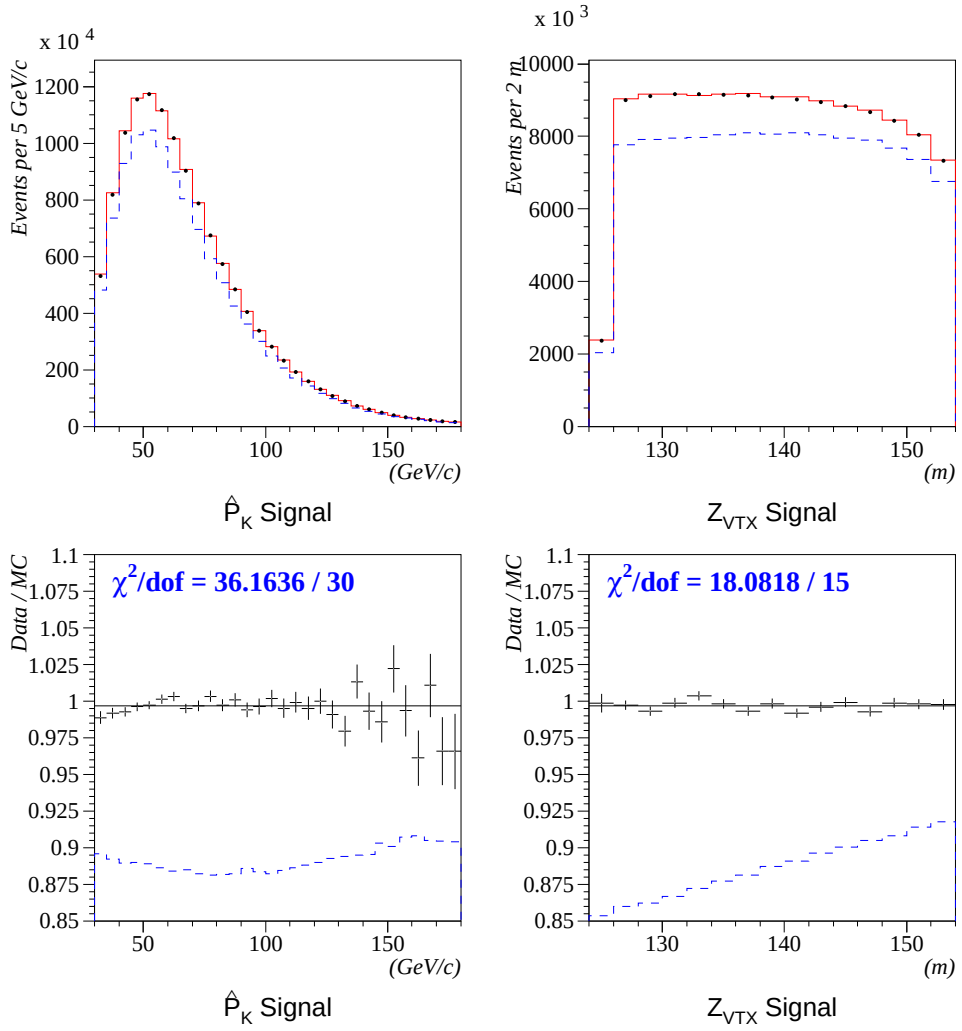

Figure 6.1: Overlay of Data on Monte Carlo for Momentum and Z Vertex Distributions in the Signal Region. The dashed line shows the level of coherent events.

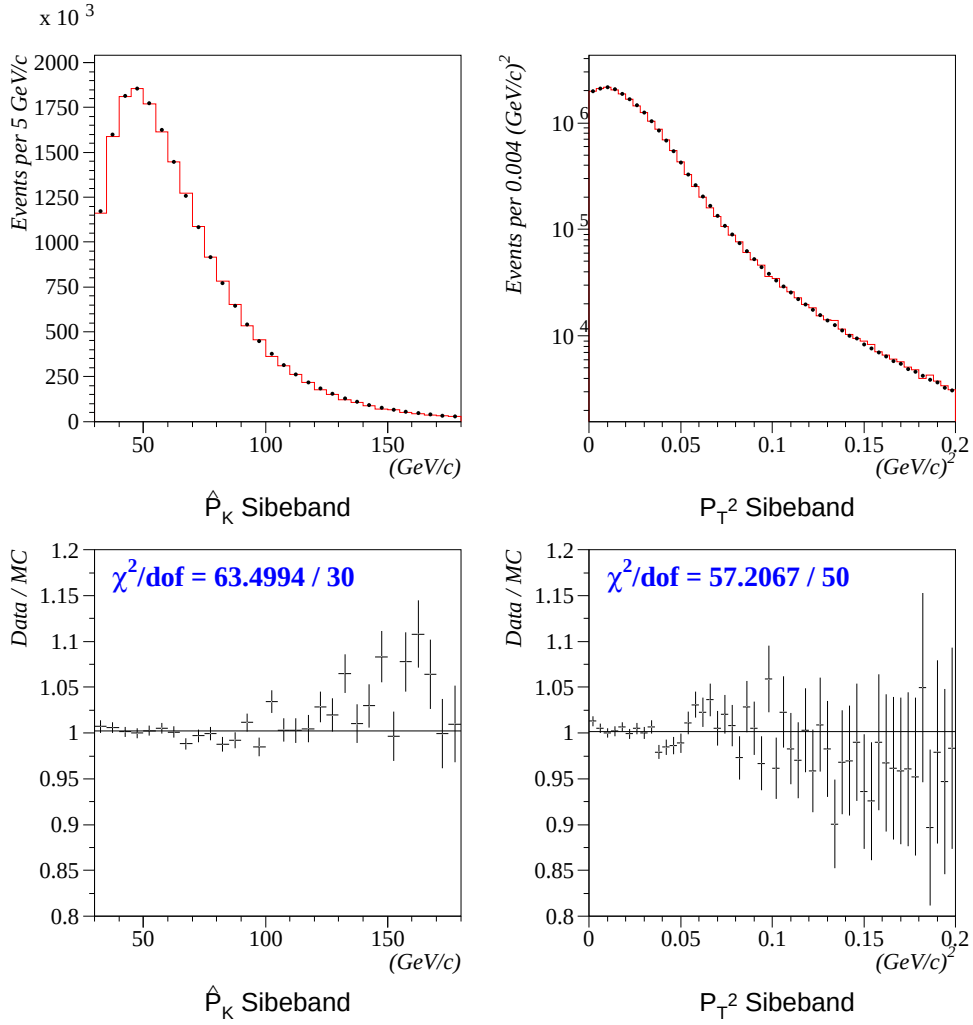

Figure 6.2: Overlay of Data on Monte Carlo for Momentum and P_T^2 Distributions for Sideband Events

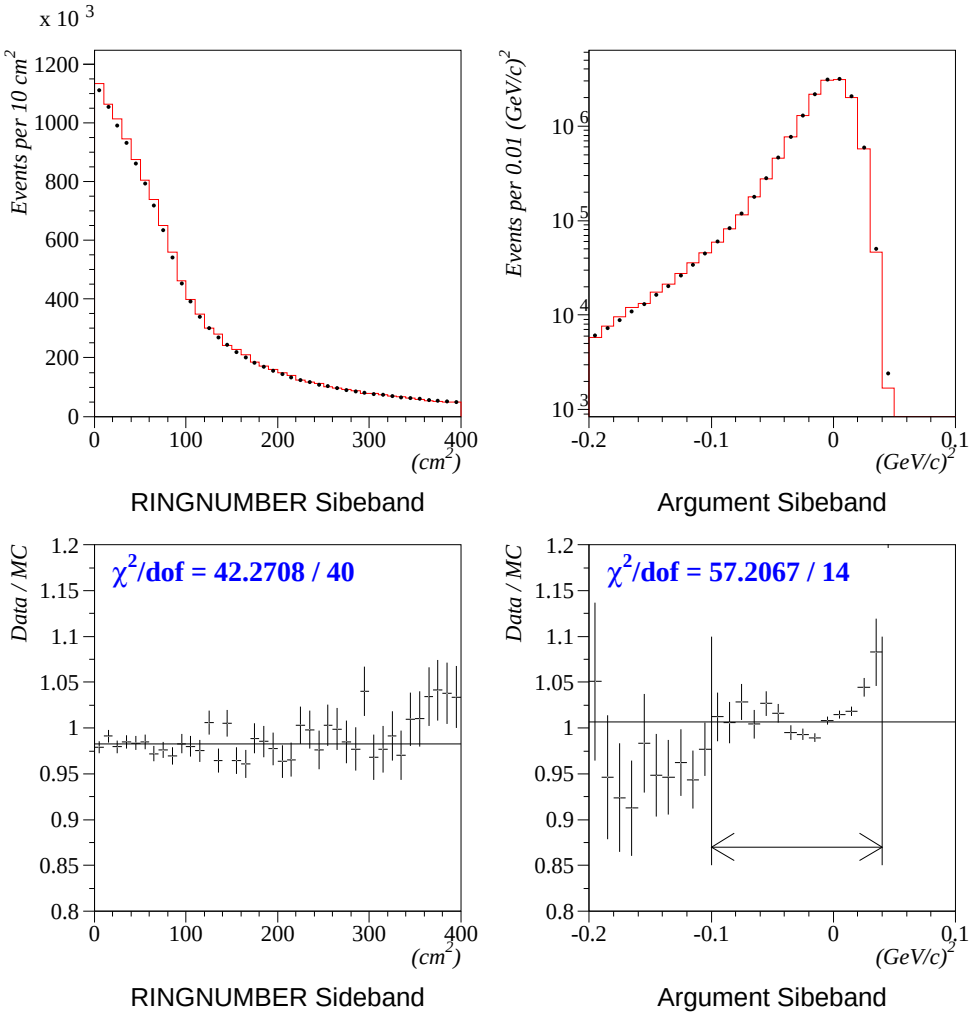

Figure 6.3: Overlay of Data on Monte Carlo for RINGNUMBER and ARGUMENT Distributions for Sideband Events

Parameter from $K_{\pi 2}$ fit	Value
$\Delta m/(10^{10}\hbar\mathrm{s}^{-1})$	0.5282 ± 0.0008
$\Gamma_S/(10^{-10}\mathrm{s}^{-1})$	1.1153 ± 0.0005
$\left\lvert\frac{f-\bar{f}}{k}\right\rvert$@70 GeV /mbarn	1.1994 ± 0.0006
α	-0.5437 $\pm$ 0.0011
χ^2/ D.o.F.	$\frac{348}{331-4}$

Table 6.2: Values of Kaon Evolution and Regeneration Parameters from $K_{\pi 2}$ Fit

Fit	$\Delta\phi_\rho$	Raw $\delta_L \times 10^6$	χ^2/D.o.F.
Baseline	0.0 Fixed	3419 Fixed	$\frac{945.93}{900}$
Simple	$-1.05(83)^\circ$	3419 Fixed	$\frac{944.35}{900-1}$
Nominal	$-0.70(88)^\circ$	3556(93)	$\frac{942.08}{900-2}$

Table 6.3: Fits for $\Delta\phi_\rho$

Testing Analyticity

Table 6.3 shows the best fits for validating analyticity. The first row shows a baseline χ^2 with no free parameters. Analyticity is assumed ($\Delta\phi_\rho = 0$), and δ_L is fixed to the uncorrected (raw) vacuum asymmetry in a similar kinematic range ($(3419 \pm 66) \times 10^{-6}$[26]). The second row shows a simple fit; only $\Delta\phi_\rho$ is floated, resulting in the most statistically powerful measurement. In the third row, our nominal fit, the raw value of δ_L is floated as well. This is preferred, despite its reduced statistical power, since decoupling the result from systematic effects of the asymmetry of the detector's particle ID efficiency is more important than the small loss of statistical power. The uncorrelated error between the simple and nominal fits is 0.32°. A comparison of the asymmetry in the data with the fit prediction for the nominal case can be seen in Figures 6.4 and 6.5.

Measuring δ_L

Although the statistical precision of a δ_L measurement in the regenerator beam is not as powerful as in the vacuum beam, the precision exceeds that of all measurements prior to KTeV and contributes to our understanding of that number.

Fit	$\delta_L \times 10^6$	$\left\lvert\frac{f-f}{k}\right\rvert$@70 GeV	χ^2/ D.o.F.
Nominal	3577 ± 89	1.1994 Fixed	$\frac{942.71}{900-1}$
No BG	3556 ± 111	0.9853 ± 0.0076	$\frac{931.04}{900-2}$

Table 6.4: Fits for δ_L

Assuming analyticity and fixing $\Delta\phi_\rho$ to zero, gives the results shown in the first row of Table 6.4. This is the most statistically powerful way to extract the raw value of δ_L from the regenerator beam K_{e3} data. To turn this into an actual value for δ_L the corrections for detector asymmetries laboriously determined in [26] are applied, taking care to account for small differences between the cuts applied on vacuum and regenerator analyses. The result after the -97×10^{-6} correction is:

$$\delta_L = (3480 \pm 89) \times 10^{-6}. \tag{6.17}$$

A systematic comparison to the vacuum beam result is postponed until the systematics section; however, I preemptively show a fit with the background simulation turned off in the second row of Table 6.4. Note that the background has a huge impact on the amplitude but an insignificant impact on δ_L.

Fit	$\Re(x) \times 10^4$	$\delta_L \times 10^6$	χ^2
Fix δ_L	36 ± 24	3417 Fixed	$\frac{943.6226}{900-1}$
Nominal	12 ± 34	3547 ± 111	$\frac{942.5494}{900-2}$

Table 6.5: Fits for $\Re(x)$

Searching for $\Delta S \neq \Delta Q$

The current best measurement of $\Re(x)$ has an absolute precision of 61×10^{-4} (CPLEAR [20]). With all other parameters fixed, the statistical precision of our fit for $\Re(x)$ is 24×10^{-4}. Table 6.5 shows the fit results. Mildly correlated with δ_L and hugely correlated with $|f_-|$ the systematic uncertainty of this result is governed by the understanding of the scattered background. If no background is included in the fit and the amplitude and $\Re(x)$ are allowed to float, a very large deviation, $\Delta\Re(x) = (450 \pm 24) \times 10^{-4}$, is observed. This sets the scale for the importance of the background. Note that in the same fit, the amplitude disagrees with the $K_{\pi 2}$ measurement by 35σ, while with the correct background treatment the same comparison differs by only 1.3σ. This difference diminishes to 0.3σ when δ_L is simultaneously floated. For this reason we again choose to sacrifice a small amount of statistical power for the more systematically robust fit with δ_L floating.

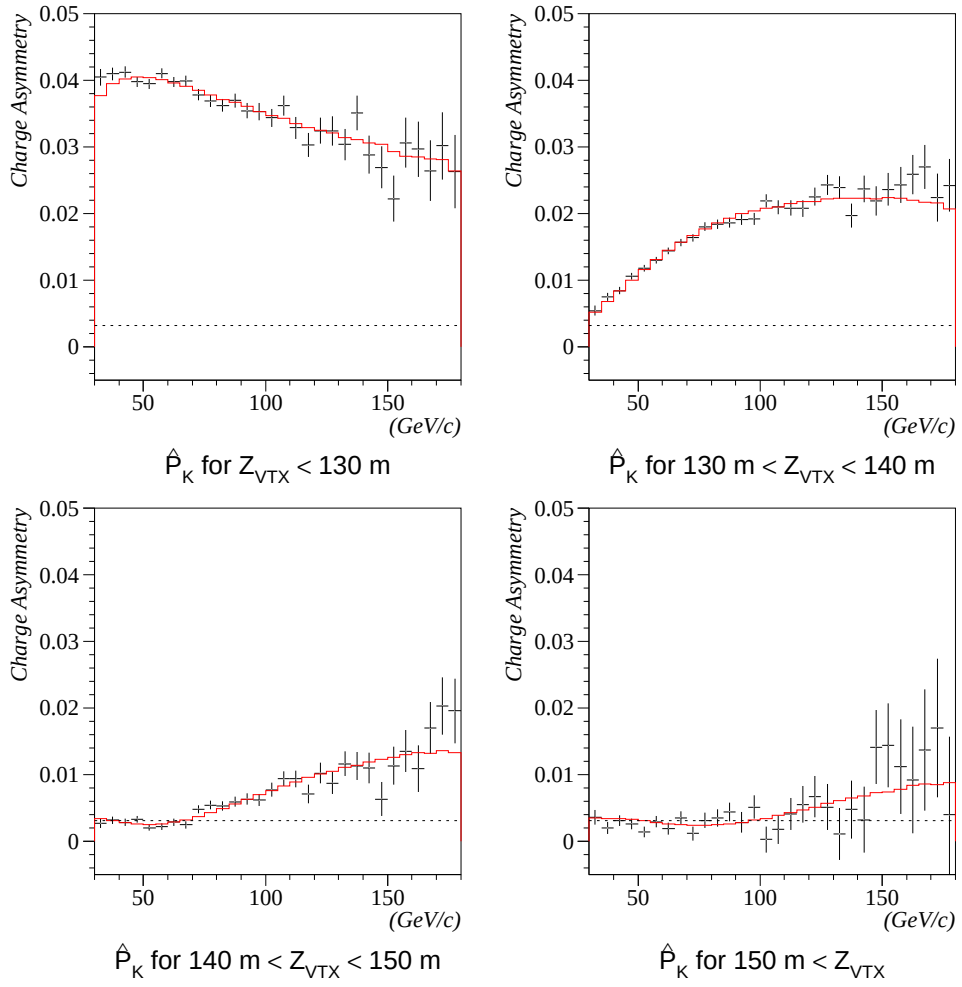

Figure 6.4: The Charge Asymmetry vs. $\hat{P}$ in Several Z Bins. The fitters prediction is overlaid. The dotted line is δ_L.

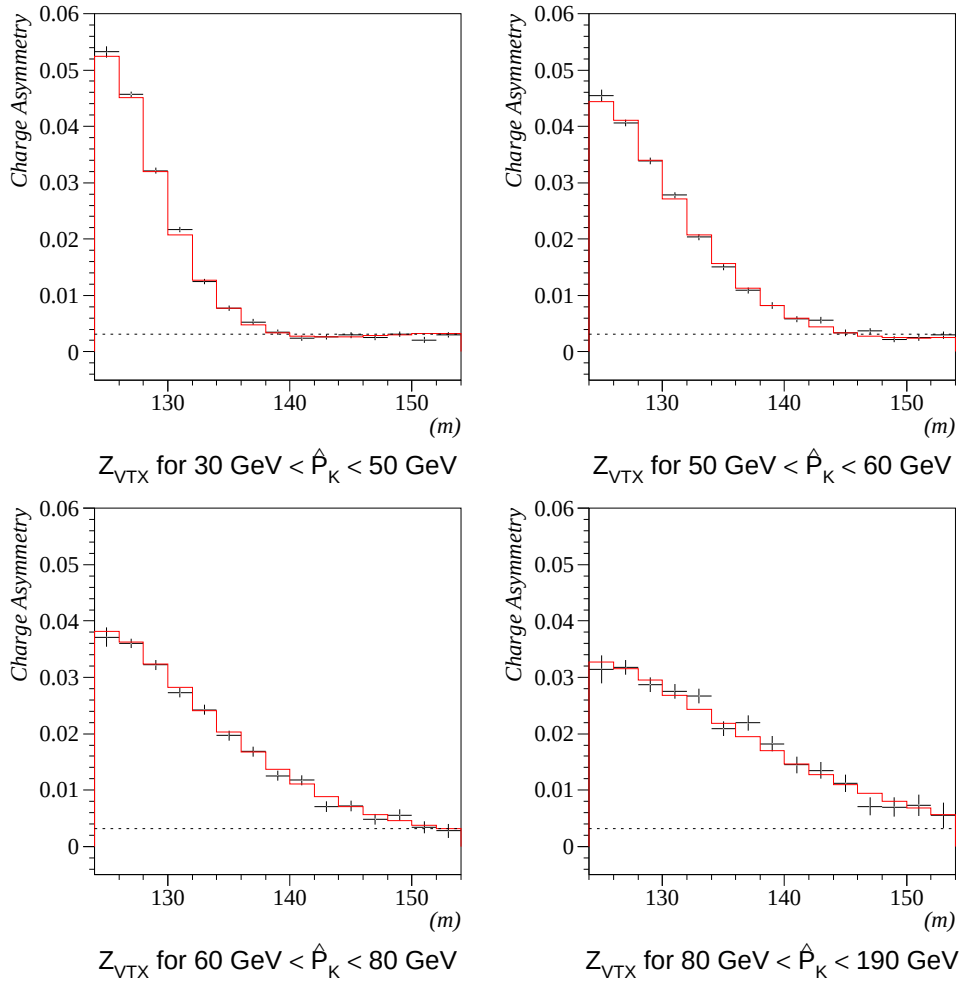

Figure 6.5: The Charge Asymmetry vs. Z in Several $\hat{P}$ Bins. The fitters prediction is overlaid. The dotted line is δ_L.

CHAPTER 7

SYSTEMATIC UNCERTAINTIES

In order to assign a systematic uncertainty to the fit results, each major piece of the analysis chain is evaluated for weakness. Figure 7.1 augments the flow chart introduced in Chapter 1 with the principal effects that this chapter seeks to quantify. Section 7.1 shows the results to be self consistent. Arbitrary partition of the data sample into time units or beam units does not impact the results. Section 7.2 shows that variation of arbitrary parameters in the fitting algorithm have minimal impact on the results. Section 7.3 addresses the impact of the large background on the fit results. Section 7.4 considers the variation of the analysis cuts. Any variation of the fit result due to variation in the cut values indicates a potential vulnerability in the method. Section 7.5 addresses the impact on our fits of the underlying detector asymmetry.

7.1 Consistency Checks

7.1.1 East-West

Although the detector acceptance may change between the east and west beam, the physics does not. Any position-dependent efficiency difference between K^+_{e3} and K^-_{e3} will result in a difference between the fit value in the east and west beams. Figure 7.2 shows the contrast between the illumination of electrons in the two beams. The pion

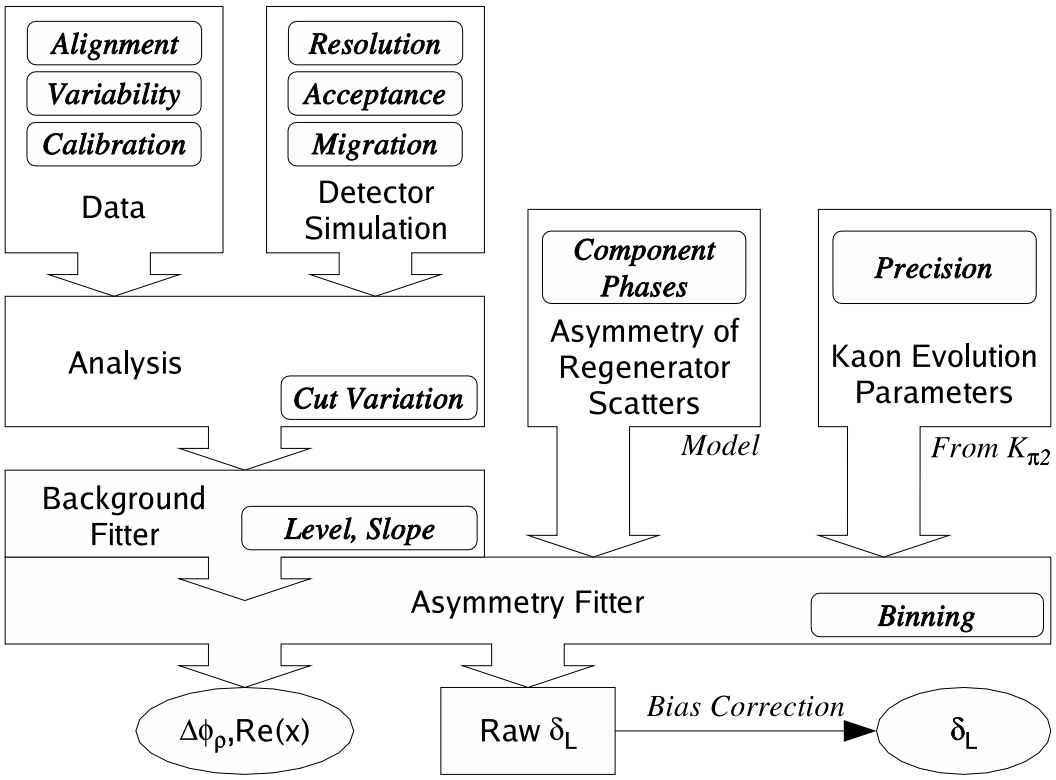

Figure 7.1: Flow Chart of Systematic Effects

illumination contrast is similar. The results of the nominal fits on east and west beams separately, Table 7.1, show no significant east/west difference.

Beam	$\delta\Delta\phi_\rho$	$\delta(\delta_L)$ $\times 10^6$	$\delta\Re(x)$ $\times 10^4$
East	$0.11^\circ \pm 1.26^\circ$	52 ± 47	3493 ± 126
West	$-1.52^\circ \pm 1.23^\circ$	-28 ± 48	3663 ± 126

Table 7.1: Comparison of East and West Beam Fit Results

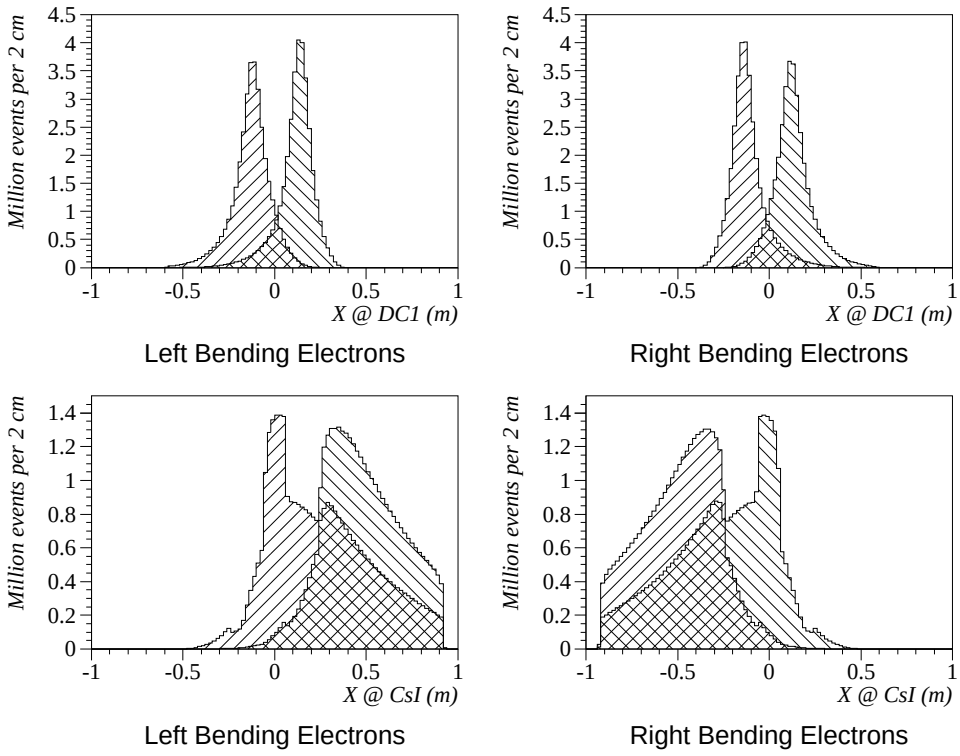

Figure 7.2: Illumination Difference Between the East and West Beams

7.1.2 Time Stability

Any variation as a function of running period would point to a detector instability that is not understood. Figure 7.3 shows the variation of the $\Delta\phi_\rho$ as a function of run period. The χ^2 for these 8 points is 5.6/7 Degrees of Freedom.

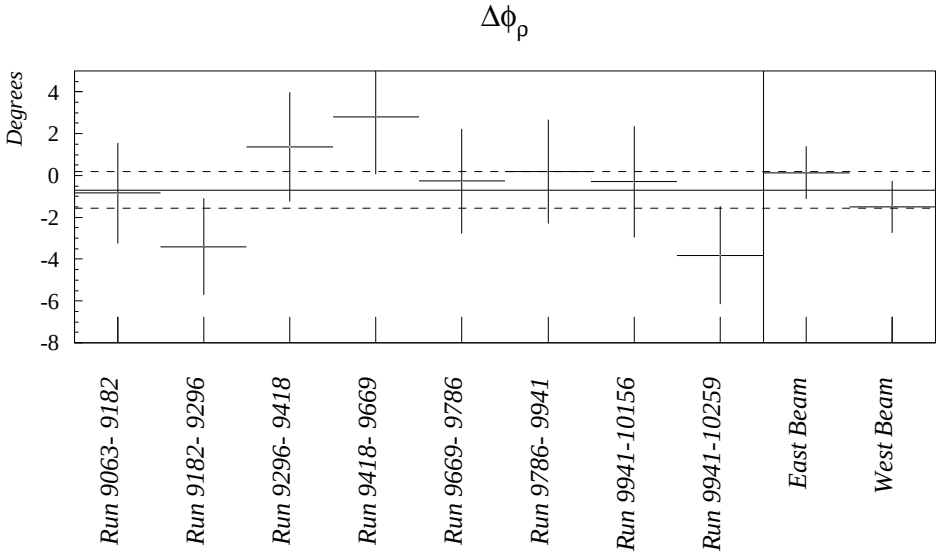

Figure 7.3: $\Delta\phi_\rho$ for several time periods and for each beam independently. For the purposes of this systematic check, δ_L and the background parameters were held fixed to the values found in the nominal fit. $\chi^2 = 7.55/(8-1)$ for the time periods. $\chi^2 = 1.09/(2-1)$ for the two beams. The largest change from the plotted values when the background is floated for each time period is 0.07°.

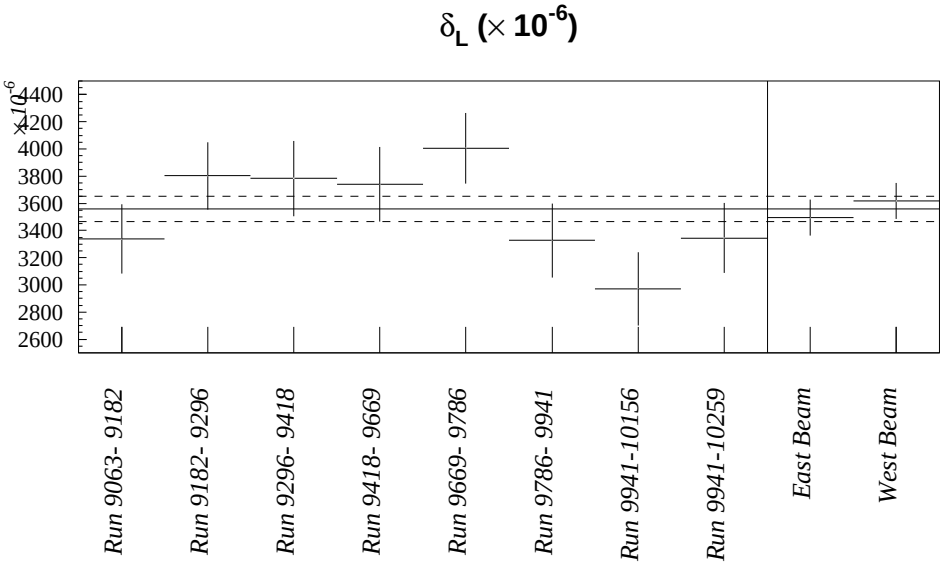

Figure 7.4: δ_L for several time periods and for each beam independently.

7.2 Fitter and Migration Systematics

7.2.1 No $K_{\pi 2}$ Constraint

A powerful test that the entire fitting apparatus is working is to remove the constraint on kaon evolution parameters derived from the $K_{\pi 2}$ data. The resulting fit measures the values of Δm, Γ_S, α and $|f_-/k|_{@70}$. Alternatively, one can fix α and $|f_-/k|_{@70}$ to the $K_{\pi 2}$ values and measure Δm, Γ_S with the K_{e3} asymmetry. Table 7.2 shows the results of these two fits. When all parameters are floated, both Δm and α are 1.9σ low. When the regeneration parameters are fixed to the $K_{\pi 2}$ values, Δm is only 1.4σ low.

Floating:	All	$\Delta m, \Gamma_S, \delta_L$
$\Delta m/(10^{10}\hbar\mathrm{s}^{-1})$	0.5050 ± 0.0121	0.5169 ± 0.0082
$\Gamma_S/(10^{-10}\mathrm{s}^{-1})$	1.094 ± 0.031	1.107 ± 0.011
$\left\|\frac{f-\bar{f}}{k}\right\|_{\mathrm{k=70\ GeV}}$ /mbarn	1.1837 ± 299	$1.1994 \pm$ Fixed
α	-0.5729 ± 197	$-0.54373 \pm$ Fixed
$\delta_L/10^{-6}$	3435 ± 213	3418 ± 145
χ^2 / D.o.F.	$\frac{937.36}{900-5}$	$\frac{940.42}{900-3}$

Table 7.2: Fit Results without the $K_{\pi 2}$ constraints on the kaon evolution and regeneration parameters.

7.2.2 $K_{\pi 2}$ Parameter Uncertainty

Parameter	shift $\times 10^4$	$\delta\Delta\phi_\rho$	$\delta(\delta_L)$ $\times 10^6$	$\delta\Re(x)$ $\times 10^4$
Δm	8	-0.07°	8.2	-1.4
Γ_S	4	-0.002°	2.0	0.9
α	10	0.09°	-3.5	2.3
$\lvert f_-\rvert_{@70\ \mathrm{GeV}}$	6	-0.04°	-4.5	-2.2

Table 7.3: $K_{\pi 2}$ Systematics.

The variation of $K_{\pi 2}$ fit parameters within their error bars induces small changes in the final fit values. Each parameter has been shifted by its uncertainty and the three nominal fits repeated. Table 7.3 summarizes the resulting small shifts in the fit values.

7.2.3 Momentum Binning in the Fitter

The fitter computes the asymmetry at the center of each P bin before using the migration matrix to extract the prediction in $\hat{P}$. The known slope in the momentum spectrum across a given P bin introduces a small bias that is not compensated for by the fitter. In the lowest bins of P and Z the difference between bin center and mean P can be as much as 0.3 GeV. To set an upper limit on the size of this bias, the fit has been repeated with varying granularity in P. Refitting with half the granularity will very nearly double the error due to this effect. Table 7.4 shows the shifts that result when larger P bins are used.

P Bin Size	$\delta\Delta\phi_\rho$	$\delta(\delta_L)$ $\times 10^6$	$\delta\Re(x)$ $\times 10^4$
5 GeV→ 10 GeV	0.064°	0.2	0.41
5 GeV→ 15 GeV	-0.052°	-0.4	1.68
5 GeV→ 30 GeV	0.19°	1.7	1.29

Table 7.4: Shift in Final Parameters When P Bin Size Is Increased

7.2.4 Z Vertex Resolution

One MC effect that does not cancel to first order in this analysis is the simulation of the detector resolution. The resolution in momentum is explicitly included via the migration matrix; the Z vertex resolution *is not* included. Figure 7.5 shows the measured Z resolutions in coarse bins of P (real parent kaon momentum) and Z.

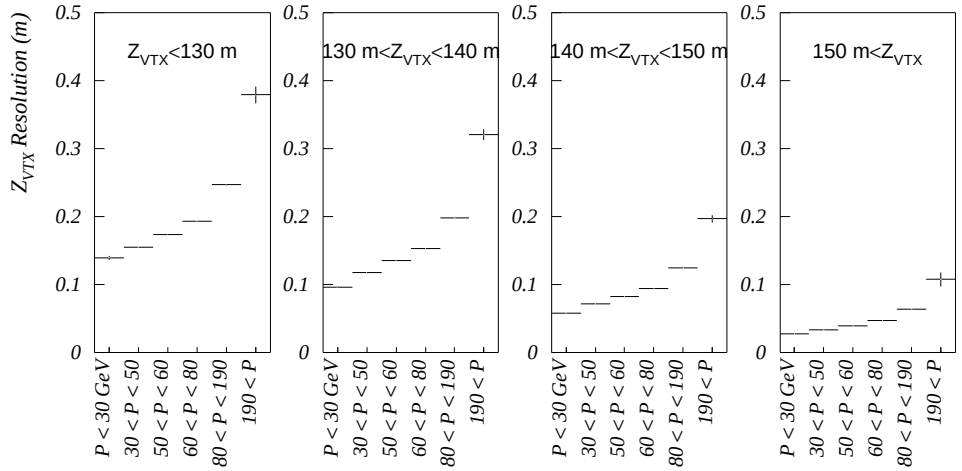

Figure 7.5: Z Resolution in the MC.

Figure 7.6 shows the slight data/MC mismatch in the track momentum resolution. The slope in $1/p^2$, which comes from multiple scattering effects, is well modeled but there is a small offset in the intercept, indicating that the MC resolution on hit positions in the chambers is slightly too large. To set the scale of a possible bias due to Z smearing, a Gaussian approximation of the resolution is convolved with the expression for the rate (Equation 1.23) when doing the Z integral in each fit bin. The width of the Gaussian is a function of $\hat{P}$ and Z drawn from a polynomial fit to the MC resolution, Figure 7.5. The resulting shifts are quite small, as seen in Table 7.5.

	$\delta\Delta\phi_\rho$	$\delta(\delta_L)$ $\times 10^6$	$\delta\Re(x)$ $\times 10^4$
Z resolution in fit	0.04°	-0.8	0.67

Table 7.5: Shift in Final Parameters When Z Resolution Is Approximated in the Fitter

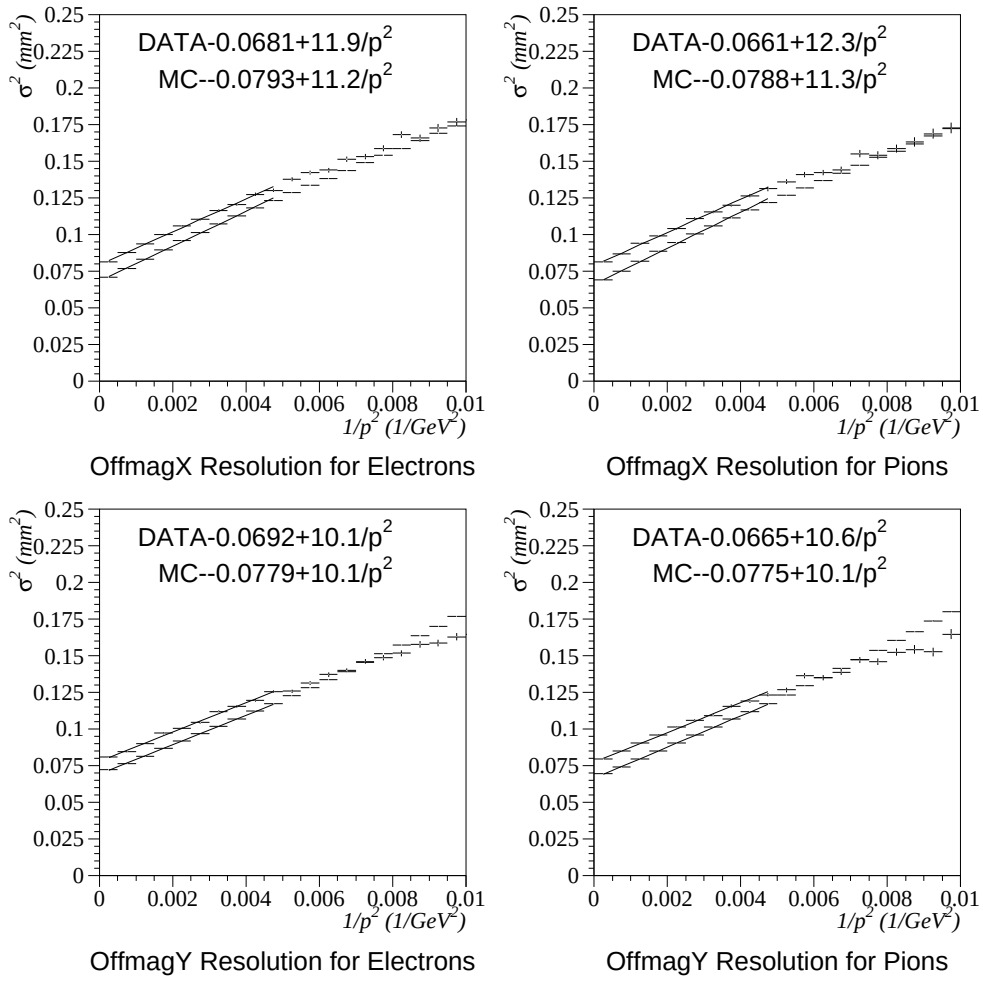

Figure 7.6: Track Resolution in Data and MC.

7.2.5 Shifts in Z Vertex

Small systematic shifts in reconstructed Z position relative to the generated position are seen in the MC. For the Z bin closest to the regenerator, this shift is 0.7 cm on average with a notable slope in $\hat{P}$. Offsetting Z in the fitter by 1.5 cm results in a

0.03° shift in the answer, limiting the size of a possible systematic effect. The effect of such a shift on $\Re(x)$ is $(8.9 \pm 1.4) \times 10^{-4}$ and the effect on δ_L is negligible.

7.2.6 Slope in Data/MC Ratio Versus Kaon Momentum

Any error in the momentum spectrum of the MC will lead to an inaccuracy of the migration matrix and directly affect the measurement. The systematic impact of the small step seen in the $\log(R_P)$ overlay (Figure 5.7) is estimated by artificially shifting the Monte Carlo value of $\log(R_P)$ down by 7×10^{-4}. The fit results are very nearly identical to those caused by shifting m_{coh} by 10^{-4}/GeV. This causes a shift of 0.04° in $\Delta\phi_\rho$. This is a much larger variation in slope than the statistical precision of 2.3×10^{-5} seen in Table 6.1. The impact on δ_L and $\Re(x)$ is negligible.

7.2.7 Sumamry of Fitter and Migration Systematics

Table 7.6 summarizes the results of our various fits. A conservative approach is taken, selecting the worst case momentum binning result. Although these errors are not guaranteed to be perfectly independent, they have been combined in quadrature to produce a final systematic.

Source	Uncertainty		
	$\delta\Delta\phi_\rho$	$\delta(\delta_L)$ $\times 10^6$	$\delta\Re(x)$ $\times 10^4$
$K_{\pi 2}$ Fit	0.12°	10.2	3.6
Fit Binning	0.19°	1.7	1.7
Z Resolution	0.04°	0.8	0.7
Z Shift	0.03°	-	10.0
P Slope	0.04°	-	-
Total	0.23°	10.4	10.4

Table 7.6: Summary of Fitter and Migration Systematics

7.3 Background

Understanding the phase and the $\hat{P}, Z$ shape of scattered background is very important to the systematic understanding of our fit. Ignoring the background entirely results in $\delta\Delta\phi_\rho = 15°$! However, the χ^2 for such a fit is horrendous. The simple step of allowing $|f_-|$ to float results in an excellent χ^2 and $\delta\Delta\phi_\rho = -1.1°$. This is surreptitiously equivalent to floating the level of a background opposite in phase to the signal to dilute the asymmetry.

7.3.1 Cut Variation

To address concerns about the $\hat{P}, Z$ shape of the scattered background we vary key analysis cuts, effectively changing the background fraction, and study the resulting shifts in the final fit parameters. Table 7.7 summarizes the shifts observed in the fits. For $\Delta\phi_\rho$/ fits, the RINGNUMBER illumination that looked troubling in Figure 5.8 shows no sign of causing systematic troubles. The combination of background and resolution tail effects on the ARGUMENT distribution, however, are problematic. The variation with ARGUMENT cut is also the standout shift in the $\Re(x)$ fits. The philosophy applied to Table 7.7 to determine a systematic is to pick the largest excursions and assign a value for which there is a 68% confidence level that the true shift is closer to zero than what we measure. Applying this philosophy, one obtains the summary in Table 7.8.

7.3.2 Simulation

Systematic contributions from the uncertainty in our background parameterization are found by looking at the wide range of fits for the background level, slope and P_T^2 shape as well as the theoretical prediction of the background phase and con-

Parameter	New Cut	$\delta\Delta\phi_\rho$	$\delta\Re(x)$ $\times 10^4$
RINGNUMBER	110→80	-0.10±0.22°	-5±1
	110→100	-0.13±0.07°	0±10
	110→120	0.01±0.06°	-8±9
P_T^2	0.54→0.50	0.00±0.03°	0±1
	0.54→0.58	0.00±0.02°	0±1
	0.54→0.62	0.00±0.02°	0±1
P_{Te}^2	0.54→0.50	0.00±0.04°	0±1
	0.54→0.58	0.00±0.03°	0±1
	0.54→0.62	0.00±0.01°	0±1
$P_{T\pi}^2$	0.54→0.50	-0.02±0.15°	-5±5
	0.54→0.58	0.02±0.01°	1±1
	0.54→0.62	0.02±0.02°	1±7
ARGUMENT$_{min}$	-0.002→0.000	-0.40±0.24°	-22±9
	-0.002→-0.004	-0.04±0.10°	-3±4
	-0.002→-0.008	0.32±0.19°	10±6
ARGUMENT$_{max}$	∞→0.03	-0.07±0.03°	1±2

Table 7.7: Background Cut Systematics

Source	Uncertainty	
New Cut	$\delta\Delta\phi_\rho$	$\delta\Re(x)$ $\times 10^4$
RINGNUMBER	0.13°	5
P_T^2 Pion	0.02°	5
ARGUMENT	0.42°	23
Total	0.44°	24

Table 7.8: Summary of Background Cut Systematics

servatively estimating the uncertainty of each piece. Table 7.9 summarizes these uncertainties and shows the variability of the fit parameters as each parameter is permitted to move to its extreme.

Source		Uncertainty	
Parameter	Shift	$\delta\Delta\phi_\rho$	$\delta\Re(x)$ $\times 10^4$
1C Level	1%	0.08°	8
1C Phase	10°	0.20°	8
1C P Slope	$\frac{10\%}{100\ \text{GeV}}$	0.18°	12
1C P_T^2 Slope	$\frac{0.5}{\text{GeV}^2}$	0.02°	10
Total		0.28°	19

Table 7.9: Background Fit Systematics

7.4 Analysis Cuts

In order to quantify the robustness of the fit, every analysis cut is varied in turn and the resulting fit recomputed. Table 7.10 shows the impact of this process on the nominal analyticity fit and the $\Re(x)$ fit.

Any cut that changes the answer by more than 1.5σ is included in the total systematic. Table 7.11 shows those parameters which exceed this threshold and the systematic uncertainty assigned for each. For the analyticity test, vertex χ^2, electron E/P, pion E/P and $P_{\pi^0 KIN}$ all cross the 1.5σ rubicon, but induce only small shifts in the answer. The variation with minimum electron energy, however, is both large and poorly determined, leading to the single biggest systematic in this analysis. For the $\Re(x)$ measurement the same 4 distributions (vertex χ^2, electron E/P, pion E/P and $P_{\pi^0 KIN}$) contribute a little, but the variation with minimum cell separation dominates the total, and the regenerator veto comes into the picture. Note that for the regenerator veto, the shift resulting from tightening the cut is used instead of the large shift seen when this cut is relaxed. In practice, loosening the regenerator cut this much causes a huge enhancement to the inelastic component of the scattered background (a factor of 3 increase), and the fits to the background

sensitive sidebands look much worse (χ^2 : 873 $\rightarrow$ 1253). The fact that the fit procedure works at all over that dynamic range of background levels is a testament to the stability of this approach.

Parameter	Shift	$\delta\Delta\phi_\rho$	$\delta\Re(x)$ $\times 10^4$
Max Offmag χ^2	500$\rightarrow$1000	$0.01^\circ \pm 0.13^\circ$	0 ± 1
Max Vertex χ^2	100$\rightarrow$500	$0.08^\circ \pm 0.02^\circ$	5 ± 1
Max Regenerator	2$\rightarrow$18 MIPS	$-0.20^\circ \pm 0.23^\circ$	-11 ± 7
Max Regenerator	2$\rightarrow$1.5 MIPS	$-0.24^\circ \pm 0.20^\circ$	-6 ± 3
Max Lead Module	0.7$\rightarrow$0.3 MIPS	$0.09^\circ \pm 0.18^\circ$	1 ± 6
Max Lead Module	0.7$\rightarrow$2.0 MIPS	$-0.04^\circ \pm 0.12^\circ$	-1 ± 4
Min Elec. EOP	0.94$\rightarrow$0.90	$-0.09^\circ \pm 0.06^\circ$	-4 ± 1
Max Elec. EOP	10.00$\rightarrow$1.05	$0.11^\circ \pm 0.05^\circ$	5 ± 1
Max π EOP	0.85$\rightarrow$0.80	$0.11^\circ \pm 0.09^\circ$	1 ± 2
Max π EOP	0.85$\rightarrow$0.90	$-0.06^\circ \pm 0.06^\circ$	-3 ± 2
Min P_π	8$\rightarrow$5 GeV	$-0.00^\circ \pm 0.13^\circ$	2 ± 11
Min P_π	8$\rightarrow$12 GeV	$0.11^\circ \pm 0.25^\circ$	2 ± 5
Min P_e	8$\rightarrow$5 GeV	$0.15^\circ \pm 0.19^\circ$	11 ± 8
Min P_e	8$\rightarrow$10 GeV	$0.45^\circ \pm 0.27^\circ$	-2 ± 10
Min P_e	8$\rightarrow$12 GeV	$0.63^\circ \pm 0.39^\circ$	-4 ± 15
Min ΔX,Y,R	3$\rightarrow$10 cm	$-0.10^\circ \pm 0.29^\circ$	-6 ± 10
Min Cell Sep.	3$\rightarrow$0	$-0.11^\circ \pm 0.29^\circ$	-3 ± 11
Min Cell Sep.	3$\rightarrow$4	$0.11^\circ \pm 0.20^\circ$	13 ± 8
$P_{\pi^0 KIN}$	0$\rightarrow$-0.02	$-0.14^\circ \pm 0.03^\circ$	-4 ± 2

Table 7.10: Analysis Cut Systematics

Source	Uncertainty	
Parameter	$\delta\Delta\phi_\rho$	$\delta\Re(x)$ $\times 10^4$
Vertex χ^2	0.08°	5
Mimimum Cell Separation	-	17
Regenerator Veto	-	7
Electron E/P	0.15°	5
Pion E/P	0.08°	4
Minimum P_e	0.67°	-
$P_{\pi^0 KIN}$	0.14°	5
Total	0.71	21

Table 7.11: Summary of Analysis Cut Systematics

7.5 Non-canceling Detector Asymmetry

KTeV's publication [26] of the vacuum beam K_{e3} asymmetry describes the handful of small effects which defeat the 4-fold way and lead to a systematic bias in the observed raw asymmetry, as well as a methodology for correcting these effects. I leverage as much of this work as possible in order to compute the biases in the regenerator beam.

The conclusion of KTeV studies of vacuum K_{e3} decay is that a correction of -97 ± 46 must be applied to the raw asymmetry in the vacuum beam to extract the true asymmetry. Small differences in the cuts used for the vacuum and regenerator analysis may contribute to a systematic change to that correction for the regenerator beam. The momentum spectra in the two beams are also different, which may cause efficiency asymmetries to contribute differently. The grossest example of such a momentum-dependent effect can be seen in the variation of the charge asymmetry of pion acceptance. Applying the momentum-dependent asymmetry measured in reference [26], I see a -150×10^{-6} shift in the regenerator fit. This is in good agreement with the shift for the vacuum asymmetry of $(-156 \pm 10) \times 10^{-6}$. Variation of the kaon evolution and regeneration parameters and the background also play a role in the systematic. Entirely removing the background but allowing the amplitude to float results in a shift of only 21×10^{-6} and actually improves χ^2 ! Assigning the full 21×10^{-6} of background, the 10×10^{-6} from Δm, 46×10^{-6} from the error estimate in the vacuum beam and 10×10^{-6} for momentum dependencies, results in a 53×10^{-6} systematic error on δ_L.

The fits testing analyticity and measuring $\Re(x)$ are explicitly not sensitive to an overall offset in the asymmetry (δ_L floats) but could be affected by the momentum dependence of these corrections. To estimate the magnitude of such an effect, I

again apply the measured pion loss asymmetry, which is both the largest correction and the correction with the largest slope in the analysis. The resulting shift of the phase is $-0.03°$. The resulting shift in $\Re(x)$ is 4×10^{-4}.

7.6 Summary

The systematic errors from all sources are combined in quadrature and summarzied in Table 7.12.

Source	Uncertainty		
	$\delta\Delta\phi_\rho$	$\delta(\delta_L)$ $\times 10^6$	$\delta\Re(x)$ $\times 10^4$
Fitting and Migration	0.23°	10	10
Background Cuts	0.44°		24
Background Fit	0.28°	21	19
Analysis Cuts	0.71°		21
Detector Asymmetry	0.03°	10	4
Asymmetry Correction		46	
Total	0.91°	53	39

Table 7.12: Final Systematics

CHAPTER 8

CONCLUSION

By analyzing K_{e3} decays downstream of the KTeV regenerator recorded in 1997, we obtain three important results. First, we constrain any non-analytic behavior of kaon-carbon scattering amplitude by precisely extracting both the regeneration phase and amplitude from the observed time evolution of the K_{e3} charge asymmetry. Second, we see no evidence of $\Delta S = \Delta Q$ violation, and set the best known bounds on its potential extent as parameterized by $\Re(x)$. Third, we obtain a precise measure of δ_L, the indirect **CP** violation seen in the charge asymmetry of K_L decay.

These measurements were made possible by the great success of the KTeV collaboration. Careful design of the overall experiment, great attention to detail for each critical system, and a lot of sweat integrating the parts into a working whole, guaranteed that a vastly complex detector was ready to turn protons arriving on target into viable and plentiful data. Many full days and nights of vigilance ensured that the living experiment continued to work. The drift chambers' gas was periodically replenished so the experiment could breath, the buzz of the audible spill monitor pulsed like a heartbeat, 20 seconds on, 40 seconds off, though day shifts, evening shifts and owl shifts. From the control room, numerous plots reported on the health of the patient, often requiring quick attention. Doctors were paged, rapid diagnoses made, and many minor surgeries evolved from cause for alarm to routine procedure. Once recorded, the data became the focus of the collaboration, and the

details involved in calibrating, simulating, and understanding the complex systems, the moving parts, and their idiosyncrasies, required just as large an effort. Terabytes of data were sorted and parsed. Hundreds of thousands of lines of code were written and tested. Underneath all the effort to tame a large dataset, to understand a complex detector, was the underlying physics of a deceptively simple process where one parent kaon decays to three children: pion, electron, neutrino. In sufficient numbers, this decay provides insight about how the world interacts with itself.

8.1 Analyticity

The observed momentum dependence of the magnitude of the amplitude is clearly seen in the $K_{\pi 2}$ decays. Analyticity, itself based on the twin pillars of **CPT** conservation and weak causality, relates this magnitude to the phase of the scattering amplitude. A standard resonance exchange model for the amplitude accurately describes the observations of the magnitude of the regeneration amplitude in the $K_{\pi 2}$ system and predicts the phase.

We have precisely measured the phase of kaon-Carbon scattering amplitude in the 30-160 GeV momentum range using the charge asymmetry of the K_{e3} decay. Subject to numerous systematic cross checks, the difference in the measured and predicted phases is:

$$\phi_\rho - \phi_{analyticity} \quad = \quad -0.70^\circ \pm 0.88^\circ \text{ (stat)} \pm 0.91^\circ \text{ (syst)} \; . \tag{8.1}$$

A typical example of analyticity, the optical theorem, is introduced to aspiring physicists as it relates to the scattering of $\sim$eV photons. This is now precisely verified in the context of tens of GeV kaons. Figure 8.1 shows the comparison

with the previous measurement of Carithers [19] along with the theoretical phase evolution.

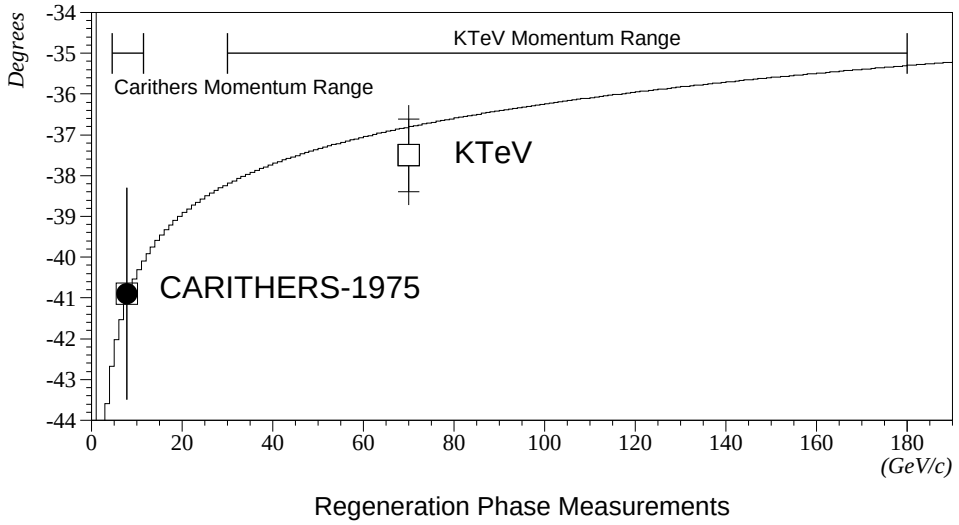

Figure 8.1: Carbon Regeneration Phase vs. Kaon Momentum. Momentum range of each dataset is shown. Tick marks on the KTeV point show the statistical component of the error. The curve is the prediction for the phase based on a fit of the $K_{\pi 2}$ amplitude data to a nuclear screening model.

A specific critique [14] of the ϕ_{+-} result focused on the resonance exchange model used to predict the impact on the phase from magnitude variations outside of the observed momentum range of the KTeV apparatus. The existence of exotic resonances could induce a shift in phase by as much as 3° without having an observable impact on the magnitude. The theoretical response [15] showed that the sensitivity of the magnitude measurement severely limits this possibility. This measurement provides direct evidence that no such large shifts are taking place. Implications on the type of exotic scattering intermediaries outside of our momentum range that are ruled out by this measurement depend greatly on the characteristics of the exotic. Rather

than try to map that space, we simply submit this observation as a constraint for consideration.

8.2 $\Delta S = \Delta Q$

Fundamental to our understanding of semi-leptonic kaon decay is the notion that the sign of the lepton charge effectively tags the strangeness of the parent kaon. An $S = 1$, neutral kaon decays to a state with $S = 0$ and e^-. An $S = -1$, neutral kaon decays to a state with $S = 0$ and e^+. The change in strangeness is the same as the change in lepton change. $\Delta S = \Delta Q$. Valid Standard Model diagrams that violate this rubric are possible, but they are suppressed by the additional role that the weak interaction must play. Predictions of the amplitude of such diagrams are beyond the precision available to current experiments. However, this dataset provides an opportunity to limit the magnitude of any exotic interactions that might produce a $\Delta S \neq \Delta Q$ final state. The complex parameter x characterizes this possibility. Our dataset is sensitive to the real part of this parameter. We measure:

$$\Re(x) \quad = \quad (12 \pm 33\ (\text{stat}) \pm 39\ (\text{syst})) \times 10^{-4}\ . \tag{8.2}$$

This is consistent with zero and slightly more precise than other measurements available. No anomalies that might threaten the Standard Model prediction for $\Delta S \neq \Delta Q$ behavior are seen. Figure 8.2 shows how our result compares to past measurements. The new world average, assuming uncorrelated errors, is found to be:

$$\Re(x) \quad = \quad (2.4 \pm 38) \times 10^{-4}\ . \tag{8.3}$$

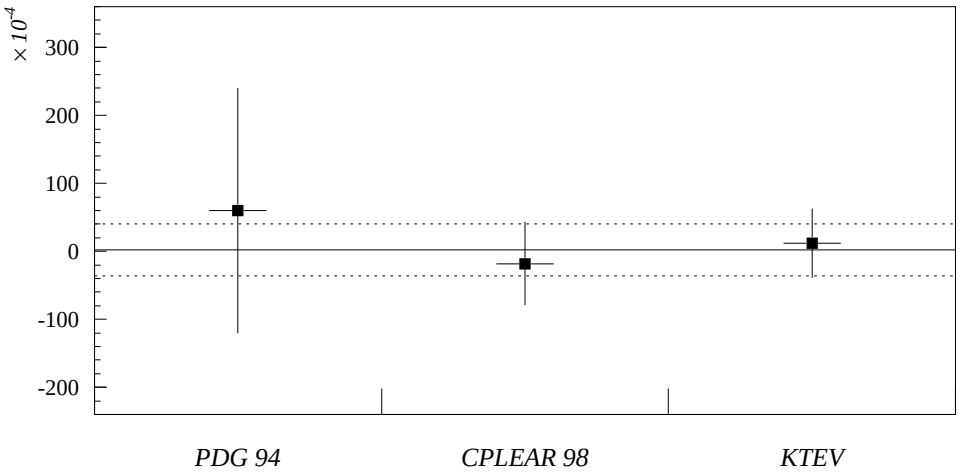

Figure 8.2: History of $\Re(x)$ Measurements. The line represents the new world average with dotted 1σ band. The global fit gives a χ^2 of 0.25 for 2 degrees of freedom. [27, 28]

8.3 K_L Asymmetry

The parameter δ_L is the charge asymmetry of the long lived kaon. **CPT** conserving theory indicates that this should be twice the real part of the **CP** violating amplitude, ϵ. KTeV's measurements of vacuum beam K_{e3} decays provide the most precise measurement of this parameter. The regenerator beam has sufficient statistics to make the second most precise measurement and to contribute contribute significantly to the world average. The final measurement, which results from the fit and a careful accounting of the small systematic biases in the detector acceptance, is:

$$\delta_L \;=\; (3480 \pm 89\ (\text{stat}) \pm 53\ (\text{syst})) \times 10^{-6} \tag{8.4}$$

Figure 8.3 shows how this compares to other measurements. The part of the systematic error uncorrelated with the vacuum beam is 21×10^{-6} resulting in a difference between the two beams (raw asymmetries) of

$$(3419 \pm 66 - 3577 \pm (90 \oplus 21)) \times 10^{-6} \;=\; (-158 \pm 113) \times 10^{-6} = -1.4\sigma \quad (8.5)$$

The resulting KTeV average is

$$\delta_L \;=\; (3472 \pm 54(\text{raw}) - 97 \pm 46) \times 10^{-6}\,, \quad (8.6)$$

and the new world average is

$$\delta_L \;=\; (3366 \pm 63) \times 10^{-6}\,. \quad (8.7)$$

8.4 Summary

The mechanics of the study of the kaon regeneration amplitude are messy. Massive statistics are needed to push the limits of precision. A capable detector is needed to limit background events and provide a well understood acceptance. A relatively large amount of theory is required to model the incoherent backgrounds and to interpret the results. At their core, the results described by this thesis are straightforward: physics as we know it stands intact despite assault on three fronts. Our precise fits for both the regeneration phase and the K_L asymmetry confirmed with new authority the underlying physics. Our null experiment in search of a surprising effect in kaon decay obtained a null result. Semi-leptonic kaon decays are a window

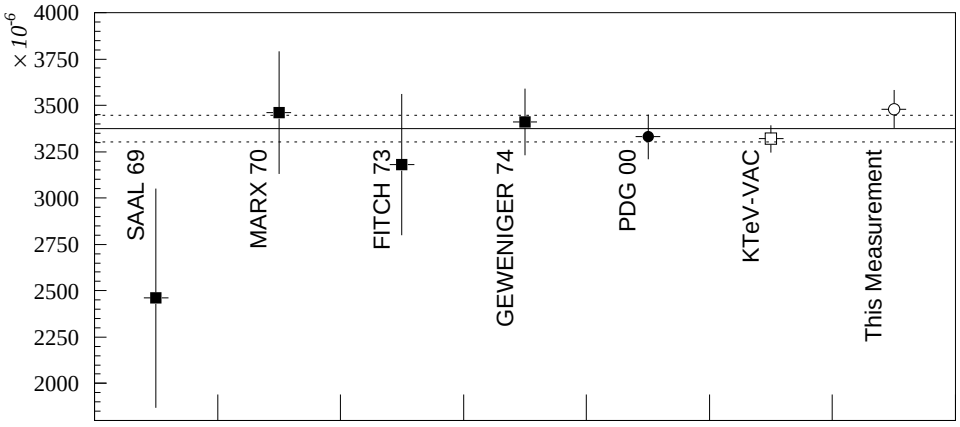

Figure 8.3: History of δ_L Measurements. The line represents the new world average δ_L with dotted 1σ band. The global fit, treating the combined KTeV as a single measurement gives a χ^2 of 2.75 for 4 degrees of freedom. [29, 30, 31, 32, 33, 8]

into the revealing realm of the kaon system, but based on the investigations described in this thesis, this niche of the Standard Model is safe.

REFERENCES

[1] R. Oehme T.D. Lee and C.N. Yang, *Phys. Rev.* **106**, 340 (1957).

[2] C.S. Wu et al., *Phys. Rev.* **105**, 1413 (1957).

[3] J.I. Friedman and V.L. Telegdi, *Phys. Rev.* **105**, 1681 (1957).

[4] L.M. Lederman R.L. Garwin and M. Weinrich, *Phys. Rev.* **105**, 1415 (1957).

[5] J. H. Christenson, J. W. Cronin, V. L. Fitch, and R. Turlay, *Phys. Rev. Lett.* **13**, 138 (1964).

[6] L. Wolfenstein, *Phys. Rev.* **13**, 563 (1964).

[7] J. A. Graham, Ph.D. thesis (The University of Chicago, December, 2001).

[8] Particle Data Group, D.E. Groom et al., *Eur. Phys. J. C* **15**, 1 (2000).

[9] R. A. Briere, Ph.D. thesis (The University of Chicago, June, 1995).

[10] J. Hilgevoord. *Dispersion Relations and Causal Description.* North-Holland Publishing Company, 1960.

[11] E. C. Titchmarch. *Introduction to the Thoery of Fourier Integrals.* Oxford University Press, 1937.

[12] J. G. Taylor, *Annals of Physics* **5**, 391 (1958).

[13] M. Block and R. Cohn, *Rev. Mod. Phys.* **57**, 563 (1985).

[14] K. Kleinknecht and S. Luitz, *Phys. Lett.* **B336**, 581 (1994).

[15] R. A. Briere and B. Winstein, *Phys. Rev. Lett.* **75**, 402-405 (1995).

[16] G.L. Kane J. Bronzan and U.P. Sukhatme, *Phys. Lett.* **B49**, 272 (1974).

[17] U.P. Sukhatme et. al., *Phys. Rev.* **D11**, 3431 (1975).

[18] J. Fischer and P. Kolar, *Phys. Rev.* **D17**, 2168 (1978).

[19] W. C. Carithers et al., *Phys. Rev. Lett.* **34**, 1240 (1975).

[20] A. Angelopoulos et al., *Phys. Lett.* **B444**, 38-42 (1998).

[21] V. Prasad, Ph.D. thesis (The University of Chicago, June, 2002).

[22] A. Alavi-Harati et al., *Phys. Rev. Lett.* **88**, 181601 (2002).

[23] C. Bown and E. Cheu, *Nucl. Instr. and Meth. A* **369**, 248 (1996).

[24] A. Alavi-Harati et al., *Phys. Rev. Lett.* **89**, 072001 (2002).

[25] A.J. Malensek, *Fermilab Report FN-341 (errata).*

[26] H. Nguyen. Long Writeup for the Measurement of δ_L in 1997 KTeV Data. KTeV Internal Document, 2001.

[27] Particle Data Group, L. Montanet et al., *Phys. Rev. D* **50**, 1173 (1994).

[28] A. Angelopoulos et al., *Phys. Lett. B* **444**, 52-60 (1998).

[29] H.J. Saal, Ph.D. thesis (Columbia University, June, 1969).

[30] J. Marx et. al., *Phys. Lett.* **B32**, 219 (1970).

[31] V.L. Fitch et. al., *Phys. Rev. Lett.* **31**, 1524 (1973).

[32] C. Geweniger et. al., *Phys. Lett.* **B48**, 438 (1974).

[33] V. Luth, Ph.D. thesis (CERN Int., June, 1974).